Frontal prism Site U1412[1]

R.N. Harris, A. Sakaguchi, K. Petronotis, A.T. Baxter, R. Berg, A. Burkett, D. Charpentier, J. Choi, P. Diz Ferreiro, M. Hamahashi, Y. Hashimoto, K. Heydolph, L. Jovane, M. Kastner, W. Kurz, S.O. Kutterolf, Y. Li, A. Malinverno, K.M. Martin, C. Millan, D.B. Nascimento, S. Saito, M.I. Sandoval Gutierrez, E.J. Screaton, C.E. Smith-Duque, E.A. Solomon, S.M. Straub, W. Tanikawa, M.E. Torres, H. Uchimura, P. Vannucchi, Y. Yamamoto, Q. Yan, and X. Zhao[2]

Chapter contents

[1] Harris, R.N., Sakaguchi, A., Petronotis, K., Baxter, A.T., Berg, R., Burkett, A., Charpentier, D., Choi, J., Diz Ferreiro, P., Hamahashi, M., Hashimoto, Y., Heydolph, K., Jovane, L., Kastner, M., Kurz, W., Kutterolf, S.O., Li, Y., Malinverno, A., Martin, K.M., Millan, C., Nascimento, D.B., Saito, S., Sandoval Gutierrez, M.I., Screaton, E.J., Smith-Duque, C.E., Solomon, E.A., Straub, S.M., Tanikawa, W., Torres, M.E., Uchimura, H., Vannucchi, P., Yamamoto, Y., Yan, Q., and Zhao, X., 2013. Frontal prism Site U1412. *In* Harris, R.N., Sakaguchi, A., Petronotis, K., and the Expedition 344 Scientists, *Proc IODP,* 344: College Station, TX (Integrated Ocean Drilling Program). doi:10.2204/iodp.proc.344.105.2013
[2] **Expedition 344 Scientists' addresses.**

Background and objectives

Integrated Ocean Drilling Program (IODP) Site U1412 (proposed Site CRIS-9A) targeted the frontal sedimentary prism, the main subduction thrust, the underthrust sedimentary section, and the upper oceanic crust. This site is along seismic Line BGR99-7 at common midpoint 4550 (Figs. **F1**, **F2**). The scientific objectives were to

1. Characterize the frontal sedimentary prism by documenting its lithology and age;
2. Sample the décollement at a shallow depth to define the deformation style, stress, fault friction, and behavior that influences coseismic displacement and plays an important in tsunami earthquakes;
3. Characterize any diagenetic processes, microstructures, and potential sealing/healing processes;
4. Characterize the physical properties of the subducting incoming and frontal prism sediments that are thought to mix with eroded upper plate material; and
5. Determine the chemistry of pore water within the wedge, décollement, and underthrust sections and characterize fluid pathways.

Wireline logging this site was a high priority to quantify the changes between underthrust material and input material.

This site was chosen because the frontal prism, subduction thrust, incoming sediment, and upper oceanic crust are well imaged with seismic reflection data (Fig. **F1**). The décollement is imaged as a high-amplitude negative-polarity reflection that indicates an inversion in seismic impedance. High heat flow measured in this area is interpreted as fluid flow in the upper oceanic crust, and estimating the style of flow is important.

Site U1412 consists of a 780 m thick section of upper plate sediments and 200 m of underthrust sediments (Fig. **F1**). The bottom-simulating reflector (BSR) is at ~200 meters below seafloor (mbsf). Sediment above the BSR is relatively transparent with few coherent reflectors. Below the BSR, a series of landward-dipping reflectors are interpreted as faults. The décollement is at 780 mbsf and is defined by a high-amplitude negative-polarity reflection. Near the toe of the margin, the décollement appears to cut sharply upward at ~1 km landward of the deformation front. Below the décollement, the incoming sediment shows little internal coherence of reflectors. The top of the oceanic crust is well defined by a large-amplitude

doi:10.2204/iodp.proc.344.105.2013

reflector. A series of steps in the basement reflector may represent blocks of oceanic crust offset by plate-bending normal faults.

Operations

First transit to Site U1412

After a 7.0 nmi transit from Site U1380, the vessel stabilized over Site U1412 (proposed Site CRIS-9A) at 0200 h on 14 November 2012. The position reference used for dynamic positioning (DP) was a combination of GPS signals and an acoustic beacon, which was deployed at 0217 h on 14 November.

Hole U1412A

Upon arrival at Site U1412, an advanced piston corer (APC)/extended core barrel (XCB) bottom-hole assembly (BHA) was assembled and lowered to 1876 m water depth. After three unsuccessful attempts at recovering the mudline, Hole U1412A (8°29.3294′N, 84°7.6686′W) was spudded at 1520 h on 14 November 2012 at a water depth of 1921 m. Nonmagnetic core barrels and the FlexIT orientation tool were used with Cores 344-U1412A-1H through 15H. Advanced piston corer temperature (APCT-3) tool formation temperature measurements were taken with Cores 3H and 5H–8H. All cores after Core 3H were partial stroke cores, and APC refusal was reached at 108.2 mbsf with Core 15H. After APC refusal was reached, the XCB coring system was deployed and coring continued through Core 25X to a final depth of 200.3 mbsf. At that time, the hole had become too unstable to continue coring. The hole was plugged with 49 bbl of heavy mud and abandoned. The drill string was pulled from the hole, clearing the seafloor at 1410 h on 16 November and ending Hole U1412A.

Fifteen APC cores and ten XCB cores were recovered from Hole U1412A (Table T1). The APC cored interval was 108.2 m with 108.8 m recovered. The XCB cored interval was 92.1 m with 61.3 m recovered. Overall recovery for Hole U1412A was 85%.

Hole U1412B

After clearing the seafloor, we attempted to recover the last XCB core barrel that had been deployed. The first attempt resulted in the aft coring line parting above the core barrel. Two wireline runs were made before eventually bringing the core barrel and sinker bars back to the surface. The vessel was offset 350 m south-southwest in the hope that the formation would be more suitable for a deeper hole. Hole U1412B (8°29.1599′N, 84°7.7512′W) was spudded at 2350 h on 16 November 2012 at 1965 m water depth. Recovery of the mudline core was slightly problematic, as remnants of wireline from the previous wireline failure obstructed the overshot. After successfully clearing the debris, an XCB core barrel with a center bit was dropped and Hole U1412B was drilled from 6.7 to 155.8 mbsf. The center bit was replaced with an XCB core barrel, and coring began at 1700 h on 17 November. Cores 344-U1412B-3X through 20X were recovered to 304.3 mbsf. Coring over the last 75 m was punctuated by erratic and high torque. The drill string first became stuck at 233.4 mbsf. After working the pipe free with 14,000 lb of overpull and 700 A of torque, the hole was cleaned and coring resumed. Coring continued until 2245 h on 19 November, when the drill string became firmly stuck for the second time. This time the string was freed from the formation with 90,000 lb of overpull and 800 A of torque. When we were unable to wash back down to 304.3 mbsf, the decision was made to terminate coring and prepare the hole for logging operations.

With the bit at 289.4 mbsf, a 50 bbl high-viscosity mud sweep was pumped to clean the hole. The drill string was then pulled to 231.3 mbsf. Four mud sweeps (total = 160 bbl) were pumped to try to keep the hole open. The wiper trip continued to 85.6 mbsf. Over the next 5.75 h, we attempted to trip and wash back to bottom, eventually reaching a total depth of 289.4 mbsf. Another 50 bbl high-viscosity mud sweep was pumped, a go-devil was dropped to open the lockable float valve, and the hole was displaced with 130 bbl of heavy logging mud. We then raised the drill pipe to 91.0 mbsf, and the logging tools were rigged up. The first logging run with the triple combination (triple combo) string started at 1040 h on 20 November. However, the tools were unable to exit the BHA and the drill string became stuck. The tools were pulled from the hole and were laid out at 1600 h. The drill string was so firmly stuck that we were unable to lower the elevators the 1 m required to land them on the elevator stool, so the vessel had to be offset by 50 m to lower the elevators. Once the elevators had landed on the elevator stool, the top drive was picked up. With the top drive installed, the mud pumps were turned on and circulation was reestablished. The drill pipe was slowly pulled from the hole, and the vessel moved back over the hole. The remainder of the drill string was pulled to the surface, and the bit cleared the rotary table at 2245 h on 20 November, ending Hole U1412B.

One APC core was taken over a 6.7 m interval with 6.74 m recovered (101%) (Table T1). Eighteen XCB cores were taken over a 148.5 m interval with 21.52 m recovered (15%). Total recovery in Hole U1412B was 28.26 m (18%). Total time spent on Hole U1412B was 104.5 h.

Hole U1412C

After the drill string cleared the rig floor, the vessel was offset 20 m north-northeast. The rotary core barrel (RCB) coring BHA was picked up and run to just above the seafloor. Seafloor depth for Hole U1412C was set at 1965.0 m from the offset depth at the previous hole. Hole U1412C (8°29.1700′N, 84°7.7467′W) was spudded at 0730 h on 22 November 2012 and was drilled with a center bit to 300 mbsf in 20 h. The hole was then cleaned with a 40 bbl high-viscosity mud sweep. Coring continued with Cores 344-U1412C-2R through 10R to a final depth of 387.0 mbsf. Excessive torque (>800 A) was present while cutting the final core, and in order to pull the final core, the bit had to be pulled back to 326 mbsf. However, high torque was still present at 326 mbsf, and the drill string had to be pulled back all the way to 239 mbsf. We then attempted to wash back to bottom to resume coring. After several hours of working to clean the hole, we reached 307 mbsf. High and erratic torque was still present. Because of the lack of progress and difficult drilling conditions, the decision was made to abandon Hole U1412C. The drill string was tripped to the surface, and the bit cleared the rotary table at 2115 h. The acoustic beacon was recovered at 1815 h, and the rig floor was secured for transit at 2200 h on 23 November, ending Hole U1412C.

Nine RCB cores were taken over an 87.0 m interval with 36.6 m recovered (42%) (Table **T1**). Total time spent on Hole U1412C was 71.25 h. The vessel proceeded to Site U1413 before returning.

Second transit to Site U1412

After a 15.0 nmi transit from Site U1413, the vessel stabilized over Site U1412 at 0330 h on 1 December 2012. The initial position was the official location of Hole U1412B, and the vessel was then offset 50 m south-southwest in the hope that the décollement could be reached at a shallower depth. The position reference used for DP was a combination of GPS signals and an acoustic beacon, which was deployed at 0418 h on 1 December.

Hole U1412D

An RCB BHA with a used 9⅞ inch bit was made up and lowered to just above the seafloor. Hole U1412D (8°29.1402′N, 84°7.7793′W) was spudded at 0850 h on 1 December 2012 at 1973 m water depth. Drilling without recovery continued with a center bit for 19.75 h to 350.4 mbsf. The hole was cleaned with a 40 bbl high-viscosity mud sweep, and the center bit was recovered with the wireline. Coring continued with nonmagnetic RCB core barrels for Cores 344-U1412D-2R and 3R to a final depth of 369.2 mbsf. Excessive torque (>500 A) was present while cutting the final core. After adding another single joint of drill pipe and dropping the next core barrel, we were unable to advance the hole. Constant high torque (1000 A) kept stalling the top drive, and we had to offset the vessel 60 m from the hole location in order to free the stuck drill string. All efforts to condition the hole and continue coring failed, and the decision was made to abandon the hole. The seafloor was cleared at 1630 h, and the beacon was recovered at 1735 h on 2 December. After recovering the beacon, the vessel began a slow move using the DP system to Site U1414. During the transit to the next site, the remainder of the drill string was recovered. The bit cleared the rotary table at 2105 h on 2 December, ending Hole U1412D and Site U1412.

Two RCB cores were taken over an 18.8 m interval with 12.3 m recovered (65%) (Table **T1**). Total time spent on Hole U1412D was 41.5 h. Total time spent on Site U1412 was 277.5 h, or 11.56 days.

Lithostratigraphy and petrology

Site U1412 was drilled to investigate the lithostratigraphy and structural geology of the slope-toe sequence and the uppermost portions of the basement, as interpreted in multichannel seismic reflection data. The primary goal of this site was to penetrate the décollement and investigate the fluid flow regime within the sediment and the oceanic crust. Four holes were cored at Site U1412, from 0 to 108.20 mbsf with the APC (Cores 344-U1412A-1H through 15H), from 108.20 to 304.34 mbsf with the XCB (Cores 344-U1412A-16X through 25X and 344-U1412B-3X through 20X), from 300.00 to 387.00 mbsf with the RCB (Cores 344-U1412C-1R through 10R), and finally, further downslope, from 350.40 to 363.98 mbsf with the RCB (Cores 344-U1412D-2R and 3R). Overall core recovery at this site was moderate (average = 59%) but became poor (<20%) toward the bottom of Holes U1412B–U1412D. Three units were distinguished in the sedimentary rocks (Fig. **F3;** Table **T2**). Unit I is predominantly dark greenish to greenish gray clay (50%) with small variations in grain size to silt (24%) and silty clay (26%) and contains eight tephra layers. This unit is terrigenous-influenced sediment. Unit I shows strong indications for gas expansion and gas hydrate disassociation. Unit II is a light to dark grayish brown calcareous nannofossil ooze with varying amounts of diatoms and sponge spicules. Primary sedimentary structures were not observed because of very strong drilling disturbances. Unit III is a sequence of grayish green clayey siltstone with minor interlayered sandstone and contains five dark grayish tephra layers. Its dominant matrix composition is terrigenous (clay) and contains nannofossils and

radiolarian and diatom fragments. The sediment in Hole U1412D is slightly more clayey, is highly bioturbated, and shows a decrease in biogenic components.

Description of units

The 387 m long combined sedimentary sequence of Hole U1412A (Cores 344-U1412A-1H through 25X), Hole U1412B (Cores 344-U1412B-1H through 20X), Hole U1412C (Cores 344-U1412C-1R through 10R), and Hole U1412D (Cores 344-U1412D-2R through 3R) is assigned to three lithostratigraphic units (Fig. F3; Table T2).

Unit I (Holes U1412A and U1412B)

Intervals: Sections 344-U1412A-1H-1, 0 cm, to 25X-CC, 53 cm, and 344-U1412B-1H-1, 0 cm, to 8X-1, 44 cm
Thickness: 204.74 m
Depth: 0.00–204.74 mbsf
Age: Holocene to early Pleistocene
Lithology: calcareous clay with minor silt and silty clay

Unit I is massive dark greenish gray clay intercalated with silty clay horizons that become more calcareous rich toward the bottom of Hole U1412A (Fig. F4). Unit I contains eight tephra layers and a glauconite-rich layer.

The clay sediment is slightly bioturbated and moderately well cemented by calcite. Silty clay horizons are dispersed throughout the length of the unit, with only a few silty-sandy horizons confined to two sections in the middle of Hole U1412A (Cores 344-U1412A-13H and 14H). Abundant sponge spicule–filled pods ranging in size from a few millimeters to ~1 cm are disseminated throughout the sediment, but their occurrence decreases toward the bottom of Hole U1412A, becoming rare in Hole U1412B.

The tephra layers in Unit I range in thickness from 2 to 7 cm and are characterized by a dark or light greenish gray color, normal grading, sharp to gradational upper contacts, and sharp lower contacts (Fig. F5). Ash pods, a few millimeters thick, are disseminated throughout both holes. The glauconite-rich layer is ~10 cm thick and has contacts that are sharp to gradational (Fig. F6). Common centimeter-sized pods of glauconite also occur in the uppermost 10 m of both holes.

The main matrix components of Unit I are terrigenous and dominated by clay. Smear slides indicate that the most common accessory grains in the silty clay include feldspar and lithic (sedimentary and magmatic) fragments. Trace components include amphibole, calcite, biotite, quartz, chlorite, glass shards, pyroxene, and opaque minerals. Biogenic components include nannofossils, diatoms, and radiolarian and foraminifer fragments. The nannofossil component becomes dominant with depth.

Unit I is moderately to highly disturbed by gas hydrate in Hole U1412A and fractured by drilling in Hole U1412B.

Unit II (Holes U1412B and U1412C)

Intervals: Sections 344-U1412B-8X-1, 44 cm, to 20X-CC, 4 cm, and 344-U1412C-1R-1, 0 cm, to 5R-CC, 10 cm
Thickness: 126.27 m
Depth: 204.74–331.01 mbsf
Age: early to middle Miocene
Lithology: Calcareous ooze with nannofossils and biogenic silica

Unit II is light to dark grayish brown silt-sized calcareous ooze with abundant biogenic silica (i.e., diatoms and sponge spicules) (Fig. F7). The massive upper part of the calcareous ooze becomes more lithified downhole and grades from very conspicuous white and laminated, 50 cm thick diatomaceous ooze into grayish brown nannofossil ooze (Fig. F8). Because of the high degree of drilling disturbance, no observations could be made regarding bioturbation. Good recovery and less disturbance in the lowermost portion of the unit allow for the identification of lamination and bedding structures, as well as reworked material.

The main matrix components of Unit II are calcareous (nannofossils and foraminifers) and silicic (sponge spicules, diatoms, and radiolarians) biogenic components. Additionally, microscopic observations of smear slides indicate that the most common accessory grains in the ooze include feldspar, glass, and lithic (sedimentary and magmatic) fragments. Trace components include amphibole, calcite, chlorite, and opaque minerals.

The uppermost 30 m of recovered sediment has a chaotic mousse-like structure due to the extensive drilling disturbance. Downhole, progressively coarse sand and pebble- to cobble-sized drill cuttings appear, often intermixed with fall-in material from the upper part of the hole.

Unit III (Holes U1412C and U1412D)

Interval: Sections 344-U1412C-5R-CC, 10 cm, to 10R-CC, 19 cm, and 344-U1412D-2R-1, 0 cm, to 3R-CC, 15 cm.
Thickness: Hole U1412C = 55.99 m; Hole U1412D = 13.58 m
Depths: Hole U1412C = 331.01–387.00 mbsf; Hole U1412D = 350.40–363.98 mbsf
Age: late Pliocene to early Pleistocene
Lithology: clayey siltstone with sandstone

Unit III is clayey siltstone with minor interlayered sandstone (Fig. F9) and contains five dark grayish tephra layers (two in Hole U1412C and three in Hole U1412D) that are as thick as 10 cm (Fig. F10). Sediment is dark grayish green clay with silt in Hole U1412D.

Within core sections that experienced the least drilling disturbance, bioturbation appears to be quite abundant, with common burrows.

The slightly calcareous clayey siltstone layers are well sorted and mostly massive. Rare laminations appear in both the siltstone and sandstone, with the latter occasionally showing reworked sedimentary lithic lenses (Fig. F9). The abundance of sand horizons increases gradually toward the base of the hole and becomes most abundant in Core 344-U1412C-8R. The sandstone beds do not show clear contacts with the underlying siltstones. Organic material (e.g., sapropel) in the sediment is generally sporadic but appears to increase in abundance toward the bottom of the hole.

Siltstone and sandstone smear slides indicate that the dominant matrix composition is clay with abundant feldspar and sedimentary rock fragments, rare to common opaque minerals, calcite, quartz, hornblende, and glauconite, along with rare biotite, pyroxene, and volcanic glass. Biogenic components identified in smear slides include common nannofossils and fragments of foraminifers, radiolarians, and diatoms. Biogenic components are much diminished in Hole U1412D.

X-ray diffraction analyses

Preliminary X-ray diffraction (XRD) analyses of sediment from Holes U1214A–U1214C suggest that there is little variation in composition within the site (Fig. F11).

Unit I

The major mineral components of Unit I are phyllosilicates, including chlorite and smectite, quartz, plagioclase, and calcite. Zeolites (laumontite and heulandite), analcime, hornblende, and pyrite are also present in all samples. Small variations in the proportion of calcite and hornblende are observed. Biotite was only observed in three samples.

Unit II

The major mineral component of Unit II is calcite. Other identified minerals include pyrite and dolomite (Fig. F11). Dolomite is present in various proportions until it becomes nearly absent from Section 344-U1412B-8X-CC to the bottom of Unit II.

Based on the background XRD patterns, we can conclude that Unit II samples contain a large amount of amorphous material.

Unit III

Two Unit III samples show that the major mineral components are phyllosilicates, including chlorite and smectite, quartz, calcite, and plagioclase (Fig. F11). Zeolites and hornblende are present in small amounts. The presence of amorphous material in Unit III could not be established.

Depositional environment

The lithology of Site U1412 represents typical lower slope sediments that are dominated by terrigenous sediment. In the lower part of the hole (204 mbsf) the lithology (Unit II) changes abruptly to Miocene calcareous ooze similar to that found at Sites U1381 and U1414, before changing to Pleistocene hemipelagic sediment again. This alternating sequence probably reflects accretion of large slivers from the incoming frontal prism.

Paleontology and biostratigraphy

We examined the microfossil content of core catcher samples from Holes U1412A–U1412C. Calcareous nannofossils and radiolarians provided biostratigraphic age estimates, and benthic foraminifers were used to characterize paleoenvironmental changes at Site U1412.

Calcareous nannofossils

Calcareous nannofossil abundance and preservation varied considerably at Site U1412 (Table T3). In Hole U1412A, nannofossils ranged from abundant to rare, with preservation from good to poor. Samples 344-U1412A-1H-CC and 2H-CC are assigned to Zone NN21, based on the presence of *Emiliania huxleyi*. For Samples 344-U1412A-3H-CC through 19X-CC, the age is less well constrained and is assigned to Zones NN19–NN21 (1.89 Ma to present). The first appearance of *Pseudoemiliania lacunosa*, which defines the top of Zone NN19, occurs in Sample 344-U1412A-20X-CC. Sample 344-U1412A-25X-CC contains the first appearance of the genus *Discoaster* spp., which constrains the base of Hole U1412A to Zones NN19–NN18 (1.89–2.39 Ma).

Nannofossil assemblages from the top of Hole U1412B overlap with those from the base of Hole U1412A. Samples 344-U1412B-3X-CC and 4X-CC are indicative of Zones NN19–NN21. Sample 344-U1412B-5X-CC, containing *P. lacunosa*, places Samples 5X-CC through 7X-CC in Zone NN19. The presence of *E.*

huxleyi in Samples 344-U1412B-6X-CC and 7X-CC might suggest contamination, potentially due to the difficult drilling conditions. A major change in assemblage occurs between Samples 344-U1412B-7X-CC and 8X-CC, coinciding with a change in lithology from green claystone to nannofossil ooze (see **"Lithostratigraphy and petrology"**). Samples 344-U1412B-8X-CC through 19X-CC contain a middle Miocene (Zone NN5) assemblage, including *Sphenolithus moriformis*, *Sphenolithus heteromorphus*, *Coccolithus pelagicus*, *Discoaster* spp., *Cyclicargolithus floridanus*, and *Reticulofenestra pseudoumbilicus*. This middle Miocene assemblage is also found in Samples 344-U1412C-2R-CC through 5R-CC. A change from Miocene to Pleistocene assemblages occurs at the top of Core 344-U1412C-6R and is coincident with a change in lithology from nannofossil ooze to green claystone.

Radiolarians

The siliceous fraction is dominated by radiolarians and diatoms, with a minor proportion of sponge spicules. Radiolarians at this site are generally common and well preserved, with the exception of Samples 344-U1412C-5R-CC through 7R-CC.

Radiolarian assemblages from Sample 344-U1412A-1H-CC through 344-U1412B-8X-CC (Unit I) are representative of the Pleistocene–Holocene. However, detailed biostratigraphic zonations could not be assigned to this interval because of the lack of diagnostically important species. The presence of *Pterocorys minythorax* and *Amphirhopalum ypsilon* suggests a depositional sequence <1.8 Ma (above Zone RN14; Sanfilippo and Nigrini, 1998). Species such as *Acrosphaera trepanata*, *Sphaeropyle langii*, *Dictyophimus crisiae*, *Botryostrobus auritus*, and *Didymocyrtis tetrathalamus* are characteristic of this assemblage.

Assemblages in Samples 344-U1412B-8X-CC through 344-U1412C-4R-CC (Unit II) are indicative of the early middle Miocene (Zones RN5–RN4). Cores 344-U1412B-8X through 18X are assigned to Zone RN5 (14.98–12.02 Ma; Kamikuri et al., 2009). Samples 344-U1412B-19X-CC through 344-U1412C-4R-CC are constrained to Zone RN4 (14.98–17.03 Ma; Kamikuri et al., 2009). Marker species for Zones RN4–RN5 include *Didymocyrtis mammifera*, *Didymocyrtis laticonus*, *Cyrtocapsella cornuta*, *Cyrtocapsella tetrapera*, *Liriospyris parkerae*, *Tholospyris kantiana*, *Periphaena decora*, *Centrobotrys thermophila*, and *Giraffospyris* sp. (Table **T4**). Because of poor preservation and low abundances, Samples 344-U1412C-5R-CC through 10R-CC (Unit III) were not assigned to a biostratigraphic zone.

Benthic foraminifers

Benthic foraminifers were studied in 41 core catcher samples: 21 from Hole U1412A, 15 from Hole U1412B, and 5 from Hole U1412C (Table **T5**). Three additional samples from working-half sections were taken at intervals 344-U1412A-19X-6W, 21–24 cm, and 344-U1412B-1H-1W, 0–2 cm, and 8X-1W, 54–56 cm. Benthic foraminifer abundances range from common to present and preservation from good to moderate in the upper and middle sections of Unit I (Samples 344-U1412A-1H-CC through 18X-CC). Abundance decreases significantly in the middle and lower sections of Unit I (Samples 344-U1412A-19X-CC through 344-U1412B-7X-CC). Foraminifers are abundant to common at the top of Unit II (Samples 344-U1412B-8X-1W, 54–56 cm, and 9X-CC). Preservation and abundance decrease downhole within Unit II, with foraminifers becoming rare and strongly recrystallized, especially in the uppermost section of Hole U1412C (Samples 344-U1412C-2R-CC through 6R-CC). Samples contained within Unit III (Samples 344-U1412C-7R-CC and 9R-CC), contain similar species to the ones in Unit I. Throughout Unit III, benthic foraminifers are rare or present.

Benthic foraminifer assemblages indicate two distinct paleoenvironments at Site U1412 that correspond closely with the lithostratigraphic units and biostratigraphic zones. The upper interval (Samples 344-U1412A-1H-CC through 344-U1412B-7X-CC) is characterized by *Cibicidoides pachyderma*, *Uvigerina* spp. (*Uvigerina peregrina* and *Uvigerina auberiana*), "Globobuliminids" (including the genera *Globobulimina*, *Praeglobobulimina*, and *Chilostomella*), *Stainforthia complanata*, *Valvulineria glabra*, *Melonis affinis*, and *Cassidulina carinata* (Fig. **F12;** Table **T5**). These species show substantial abundance variations downhole that are likely related to changes in the quantity and quality of the organic flux or variations in sediment oxygen concentrations (Fontainer et al., 2002).

The lower interval (Sections 344-U1412B-8X-1W through 344-U1412C-6R-CC) roughly coincides with Unit II. Benthic foraminifer assemblages are substantially different from Unit I and include *Globocassidulina subglobosa*, *Hansenisca altiformis*, and two species completely absent from Unit I, *Planulina renzi* and *Cibicidoides pachyderma* var. *bathyalis*. The last occurrence of *P. renzi* occurs in the middle Miocene, coinciding with the first appearance of *Fontbotia wuellerstorfi* (van Morkhoven et al., 1986). Although these two species, present in Unit II (Table **T5**), are not widely used biostratigraphic markers, they help to further constrain Unit II to the Miocene. Benthic foraminifer assemblages in Unit II are characteristic of mesotrophic to oligotrophic conditions and contain a relatively high proportion of epibenthic foraminifers (e.g., *Planulina* and *Cibicidoides*), suggesting low sedimentation rates and/or high bottom currents.

Unit III benthic foraminifers differ considerably from those in Unit II but are similar to those in Unit I.

However, given the low abundance of individuals, a comparison with Unit I was not possible (Table T5).

Structural geology

Site U1412 is located on the prism-toe of the Costa Rica margin ~2.5 km from the frontal thrust. The primary goal at Site U1412 was to describe and document the style, geometry, and kinematics of the prism units, décollement zone, and underthrusted sediments. Hole stability issues limited recovery. In particular, Holes U1412B and U1412D yielded few structural data. Structural observations were discontinuous. We divided the structural data into two intervals corresponding to Holes U1412A and U1412B and Holes U1412C and U1412D.

Holes U1412A and U1412B (0–200.3 mbsf)

Bedding dip varies from subhorizontal to intermediate dip angles as large as 35° (Fig. F13). After orienting the dip directions and dip angles into geographic coordinates, the mean bedding attitude is west-southwest, with some surfaces dipping northwest. The bedding orientation is not depth dependent. The bedding trends (NNE–SSW and southwest–northeast) are subparallel to the trench and the proximal flank of the Cocos Ridge, respectively. The combination of the trench and the subducting Cocos Ridge probably results in the two preferential orientations of the bedding planes.

Hole U1412A cores are characterized by the presence of normal faults. These structures form distinct shear planes with little displacement but well-preserved striations (Fig. F14). After orienting the dip directions, dip angles, and striations into geographic coordinates, the faults appear to form two conjugate sets with northwest–southeast and NNE–SSW trends (Fig. F15A). This data set reveals a subvertical orientation of the maximum principal stress axis, σ_1, and a subhorizontal, ENE–WSW orientation of the minimum principal stress axis σ_3 (Fig. F15B), indicating a stress regime characteristic of normal faulting. We interpret these faults to be compaction-related features. The interval where these conjugate normal faults occur ranges from 28 to ~143 mbsf within lithostratigraphic Unit I. As the stratigraphic age within this interval is Pleistocene, the deduced formation age of the normal faults is younger than Pleistocene.

Holes U1412C and U1412D (300–387 mbsf)

Cores from Hole U1412C are both highly deformed and characterized by drilling disturbance. Hole U1412D was located 50 m trenchward of Hole U1412C, making direct correlation of the structures with Holes U1412A and U1412B difficult. Paleomagnetic orientation of the structural data is particularly difficult and cannot be provided at this time. Bedding planes measured in Hole U1412C show dip angles between 45° and 65° (Fig. F13). This hole is characterized by the presence of two fault zones with prominent brecciation. These fault zones are localized between 330 and 342 mbsf and 358 and 365 mbsf. The upper fault zone is located at the boundary where sedimentary age reverses from Miocene to Pleistocene (see **"Paleontology and biostratigraphy"**). The age reversal may be due to large accumulated displacement on the fault and suggests high activity and multiple faulting episodes. Adjacent to and within these fault zones, well-developed foliation with varying dip angles is observed (Fig. F13). Foliation is not clearly developed in Hole U1412D cores, suggesting less intense deformation. Interestingly, some normal faults similar to those present in Hole U1412A (Fig. F16) are observed in Hole U1412D and are interpreted to be compaction-related features.

Hole U1412C is additionally characterized by distinct fault planes mainly developed as reverse faults with moderately steep to steep dip angles (Fig. F13). Normal faults were also observed.

Geochemistry

Inorganic geochemistry

We collected 29 APC whole-round samples (12–25 cm long), 9 XCB whole-round samples (20–25 cm), and 10 RCB whole-round samples (11–37 cm) on the catwalk at a frequency of 1–3 samples per core through Core 344-U1412A-15H and 1–2 samples per core in the XCB and RCB cored intervals of Holes U1412B–U1412D. Most XCB cores were too disturbed for adequate pore fluid sampling. All samples were thoroughly cleaned for drill water contamination. The cleaned samples were placed in Ti squeezers and squeezed at gauge forces of <30,000 lb. The inner diameter of the Ti squeezers is 9 cm; thus, the maximum squeezing pressure was 3043 psi (~21 MPa). The pore fluid was collected in syringes and passed through a 0.2 µm filter prior to analysis. The volume of pore fluid recovered varied with lithology and coring technique, from 23 to 56 mL from the APC cores, from 0.8 to 50 mL from the XCB cores, and from 3.5 to 35 mL from the RCB cores. The chemical composition of the samples below the sulfate–methane transition zone (SMTZ) at 14.7 mbsf was corrected for drill fluid contamination where the sulfate data indicated contamination <5%. Specific aliquots were used for shipboard analyses, and the remaining fluid was sampled for shore-based analyses (see **"Geochemistry"** in the "Methods" chapter [Harris et al., 2013]).

The uppermost three cores were processed under a nitrogen atmosphere and used for detailed studies of biogeochemical processes in the SMTZ. In addition to the 10 cm interstitial water samples, a 2 cm slice from the cleaned sediment was collected for shore-based microbiological analyses. These microbiological samples were collected through Core 344-U1412A-15H. The cleaned samples were vacuum-sealed and stored at –80°C.

To collect enough methane concentration data above the methane saturation depth, we sampled sediment immediately below the SMTZ at high resolution. We used real-time sulfate concentration analyses to accurately delineate the SMTZ at 14.7 mbsf. These real-time measurements allowed us to select the core sections immediately below the SMTZ (Sections 344-U1412A-2H-7 and 3H-1), which were sampled on the catwalk at 20 cm intervals. Three headspace samples were collected from each interval for shore-based concentration and isotope analyses of the dissolved gases. Additionally, we collected one whole round just above the SMTZ depth and one below for shipboard interstitial water analyses.

In Section 344-U1412C-7R-2 we collected one whole-round sample for He isotope analysis.

The APC cores recovered from Hole U1412A do not show significant drilling contamination. In contrast, samples from Holes U1412B and U1412C were highly disturbed by drilling. Because the samples from these cores were recovered below the SMTZ, no sulfate should be present in these samples. We used the sulfate concentrations reported in Table **T6** as a tracer for drilling contamination with surface seawater and corrected the pore fluid concentrations in the samples from Holes U1412B and U1412C, as described in **"Geochemistry"** in the "Methods" chapter (Harris et al., 2013).

Raw data for major and minor element concentrations are listed in Tables **T6** and **T7.** In Tables **T8** and **T9** we list the sulfate-corrected concentration data. Sulfate-corrected data for Holes U1412A–U1412C are illustrated in Figures **F17, F18, F19,** and **F20.**

Because of drilling problems and no core recovery suitable for pore fluid analyses, all figures show a gap in data points between ~200 and ~320 mbsf.

Salinity, chloride, and alkalis (sodium and potassium)

Downhole profiles of salinity, chloride, sodium, and potassium at Site U1412 are shown in Figure **F17.** Salinity values slightly decrease with depth from the seawater value at the seafloor, 35, to ~30 at the base of the hole. Chloride concentrations, however, do not vary significantly with depth. A few discrete excursions to lower values between 60 and 85 mbsf are consistent with observations of moussy sediments in the cores and of a BSR and may be indicative of gas hydrate dissociation during core recovery.

Sodium concentrations remain relatively constant in the APC cores recovered from Hole U1412A. They show a marked decrease toward the sediment of lithostratigraphic Unit II to a low value of 331 mM at 163 mbsf, which is also apparent in the low concentrations measured in the three samples collected at the bottom of this unit at ~187, 196, and 329 mbsf in Hole U1412C. The decrease may be driven by volcanic tephra alteration to zeolites. Sodium concentrations increase toward the bottom of the hole but still remain lower than seawater in the deepest sample, which has a concentration of 369 mM.

There is no significant change in the concentration of potassium in the sampled depth interval. In the uppermost ~100 m, potassium concentrations are slightly higher than the seawater value of 10.5 mM by 1–2 mM, most likely because of clay ion exchange reactions. The reason for scatter in the data points in the XCB core samples is unclear. Potassium concentrations in Hole U1412C (325–370 mbsf) are 1 mM lower than seawater value, which may be caused by volcanic tephra alteration to clays.

Alkalinity, sulfate, ammonium, phosphate, calcium, and magnesium

Pore fluid profiles of sulfate, alkalinity, ammonium, and phosphate in the uppermost 100 to 200 m at this site reflect characteristic organic matter remineralization (Figs. **F18, F19**). Sulfate concentrations decrease almost linearly from the seafloor to the SMTZ at 14.7 mbsf. Alkalinity increases from the seawater value at the seafloor to a maximum of 44 mM at 56 mbsf and gradually decreases with depth to ~4 mM in the deepest sediments cored at Site U1412. Alkalinity is involved in carbonate diagenesis in the uppermost ~150 m, as suggested by the Ca profile. Phosphate reaches its maximum concentration of 121 µM at 23 mbsf, at a shallower depth than alkalinity, and its concentrations decrease sharply with depth, possibly because of minor apatite precipitation. Ammonium peaks at a greater depth than alkalinity and reaches a maximum value of ~9.3 mM at 111 mbsf. Ammonium concentrations show an increasing trend with depth below ~300 mbsf. However, there are not enough data points to properly interpret this trend.

Ca and Mg concentrations decrease from seawater values at the seafloor to minima of ~3.9 and ~40 mM, respectively, at the SMTZ at 14.7 mbsf, reflecting precipitation of authigenic carbonates. There, however, the concentrations of both Ca and

Mg, but in particular Ca, increase at the depth of the highest alkalinity values, and more marked increases are noted in the samples below 170 mbsf, indicating the presence of diagenetic sources for both cations. In lithostratigraphic Unit III, Ca concentrations reach a maximum value of ~13 mM, slightly higher than the seawater value, suggesting a source of Ca at greater depth. In contrast, Mg concentrations decrease with depth to a minimum of ~22 mM, accounting for only half of the seawater values. The inverse concentration-depth profiles of Ca and Mg also suggest interaction with a high-temperature reaction zone at depth.

Strontium, lithium, manganese, boron, silica, and barium

Downhole distributions of Sr, Li, Mn, B, Si, and Ba are shown in Figure **F20.** Sr concentrations remain near the seawater value of 87 µM throughout Hole U1412A, with only a small incursion to low concentrations and a minimum value of 68 µM at 8.8 mbsf. The overall lower concentrations in the uppermost 20 m are coincident with the observed decrease in calcium and suggest Sr uptake during carbonate precipitation. Sr in samples from Hole U1412B increases with depth, continuing toward the bottom of lithostratigraphic Unit III. The gap in data between ~200 and 320 mbsf precludes good interpretation of the diagenetic reactions responsible for the increase in Sr concentrations.

Li concentrations decrease in the uppermost 20 m from a seawater value of 25 to 5.9 µM at ~23 mbsf. Such a decrease in Li concentrations in the upper sediments offshore Nicoya was analyzed in the context of lithium isotope data by Chan and Kastner (2000), who interpret their results as a balance between ash alteration at low temperatures and ion exchange from clays; indeed, a rather thick ash layer is present at this depth (see **"Lithostratigraphy and petrology"**). In general, Li concentrations increase with depth from the minimum at 23 mbsf to ~100 µM at the bottom of the cored section. These elevated values suggest interaction with a high-temperature reaction zone at depth, consistent with the calcium data.

B values steadily decrease in lithostratigraphic Unit I from seawater value to ~100 µM at ~170 mbsf, perhaps driven by volcanic tephra alteration and/or siliceous ooze diagenesis in lithostratigraphic Unit II. However, because of a lack of data this interpretation cannot be verified.

Even the shallowest samples collected in Hole U1412A show an increase in dissolved Si to ~600 µM, a value that remains relatively constant throughout lithostratigraphic Unit I. Si concentrations are variable in Hole U1412C, ranging from 173 to 986 µM.

Dissolved Ba shows a marked increase in concentration below the SMTZ (Fig. **F18**), associated with dissolution of marine barite in environments depleted in sulfate (e.g., Torres et al., 1996). Ba concentrations remain relatively constant below ~40 mbsf and increase with depth in Holes U1412B and U1412C, suggesting a deeper source for this element.

Organic geochemistry

At Site U1412, we collected 64 samples for headspace gas, and 20 voids were also sampled for shore-based gas analyses. The data from these samples are listed in Tables **T10** and **T11** and plotted in Figures **F21** and **F22.** In the headspace gas samples, methane concentrations range from 4 to 31,400 ppmv, ethane concentrations are <12 ppmv, propane concentrations do not exceed 3 ppmv, and C_{4+} was not detected at all. In the void gas samples, methane concentrations range from 770,000 to 850,000 ppmv, ethane ranges between 14 and 85 ppmv, propane concentrations are <11 ppmv, and C_{4+} was not detected at any depth.

In general, methane concentrations increase rapidly below 14.1 mbsf, consistent with the depth of the SMTZ at this site (Fig. **F18**). The gas composition of the headspace and void gas indicates that gas originates from a biogenic source. However, the decrease with depth in the C_1/C_{2+} ratios of headspace and void gas to ~400 indicates a mixture of biogenic gas and thermogenic hydrocarbons that likely migrated from depth.

The organic and inorganic carbon (IC) profiles are illustrated in Figure **F23** and listed in Table **T12.** In lithostratigraphic Unit I, total carbon fluctuates between ~1.2 and 2.9 wt%; IC ranges from ~0.1 to <1.2 wt%, which corresponds to $CaCO_3$ concentrations ranging from 0.9 to 9.6 wt%; and total organic carbon (TOC) concentrations decrease from 1.8 to 0.8 wt%. There is a marked change to higher values in lithostratigraphic Unit II, with IC ranging from ~3 to 8.5 wt%, which corresponds to $CaCO_3$ concentrations ranging from 25 to 68 wt% and TOC concentrations decreasing from 1.8 to 3 wt%. In lithostratigraphic Unit III, IC ranges from ~0.4 to 0.9 wt%, which corresponds to $CaCO_3$ concentrations ranging from 3.4 to 7.7 wt%, and TOC concentrations are relatively constant at ~1 wt%.

Total nitrogen concentrations do not exceed 0.18 wt%. The calculated C/N ratio in Hole U1412A ranges between 5.4 and 15.6, suggesting that the sediment might be degraded marine organic matter. However, to fully characterize the organic carbon source we require information on the carbon isotopic ratios and other organic matter tracers.

Physical properties

At Site U1412, physical properties measurements were made to help characterize lithostratigraphic units. After sediment cores reached thermal equilibrium with ambient temperature at ~20°C, gamma ray attenuation (GRA) density, magnetic susceptibility, and *P*-wave velocity were measured using the Whole-Round Multisensor Logger (WRMSL). After WRMSL scanning, the whole-round sections were logged for natural gamma radiation (NGR) and thermal conductivity was measured using the full-space method on unconsolidated sediments. Following core splitting, color reflectance and magnetic susceptibility were measured on the archive-half cores. Moisture and density (MAD) were measured on discrete samples collected from the working halves of the split sediment cores, generally once per section. *P*-wave velocity and strength were measured on the working halves of split cores, depending on recovered length and condition. For consolidated sediments in Hole U1412C, thermal conductivity was measured on the split core using the half-space method.

Density and porosity

Bulk density values at Site U1412 were determined from both GRA measurements on whole-round cores and mass/volume measurements on discrete samples from the working halves of split cores (see **"Physical properties"** in the "Methods" chapter [Harris et al., 2013]). Both types of measurements yield similar trends, but the GRA values show greater scatter. GRA values scatter higher and lower than the MAD density values in APC cores and are generally less than or equal to MAD density values for XCB and RCB cores. Gas expansion voids in Hole U1412A and variable core diameter and drilling disturbance in the XCB and RCB cores contribute to the scatter in GRA density values (Fig. **F24**). Bulk density values increase and porosity values decrease in the uppermost 30 m. Both properties remain stable to the base of Unit I, with average bulk density and porosity values of 1.69 g/cm^3 and 60%, respectively. In Unit I, the average grain density is 2.69 g/cm^3. Both the GRA and the discrete samples indicate some scattered high bulk density values in Units II and III. Just above the Unit II/III boundary, three discrete samples yielded high bulk densities and abnormally low grain densities. Limited data do not allow us to assess whether these values are real or due to measurement errors.

Bulk density and porosity values in Unit III show considerable variability but suggest slightly more compaction (higher bulk density and lower porosity) than that at the base of Unit I. Unit III samples from Hole U1412D show porosity trends similar to those from Hole U1412C but at a slightly (~15 m) shallower depth.

Magnetic susceptibility

Volumetric magnetic susceptibilities were measured using the WRMSL, and point measurements were made on the SHMSL for all core sections longer than ~20 cm at Site U1412 (Fig. **F25**). Magnetic susceptibility values measured by these two methods are in good agreement. In Unit I, the background magnetic susceptibility is between 20 and 30 IU. Magnetic susceptibility excursions reach ~200 IU and are sometimes, but not always, associated with tephra layers. The few recovered intervals in Unit II yielded low magnetic susceptibility values (<15 IU). Magnetic susceptibility in Unit III is variable, ranging from near 0 to ~75 IU with one excursion to >160 IU.

Natural gamma radiation

NGR counting periods were 10 min, and measurement spacing was fixed at 20 cm for all holes and sections. NGR results are reported in counts per second (cps) (Fig. **F26**). NGR values in Unit I generally range between 15 and 25 cps. Lower NGR values (around 10 cps) are observed within Unit II. NGR values in Unit III are higher and have greater variability than those within Units I and II. The highest counts, around 46 cps, were observed within Unit III at 362 mbsf.

P-wave velocity

P-wave velocity at Site U1412 was measured on the working halves of cores using the *P*-wave caliper (Fig. **F27**). Because of gas expansion, poor recovery, and drilling disturbance, *P*-wave velocity data could only be collected from limited intervals. In the uppermost 25 mbsf of Unit I, *P*-wave velocities vary between 1520 and 1600 m/s. From ~330 mbsf, just above the boundary between Units II and III, to the bottom of Unit III, *P*-wave velocity shows scattered values around 1500 ± 200 m/s.

Thermal conductivity

Thermal conductivity measurements were conducted on sediment whole-round cores using the needle-probe method and on lithified split cores using the half-space method (see **"Physical properties"** in the "Methods" chapter [Harris et al., 2013]). Thermal conductivity values within Unit I range from 0.7 to 1.2 W/(m·K), with most values between 0.9 and 1 W/(m·K). Thermal conductivity values decrease slightly with depth, possibly because of gas disturbance of the core (Fig. **F28A**). This trend contradicts

the commonly observed inverse correlation with porosity, which is nearly constant within Unit I (Fig. F24). However, thermal conductivities are higher in Unit III compared to Unit I, following the inverse relationship with porosity. Thermal conductivity values within Unit III are higher than those within Unit I, and they rapidly increase with depth from 1 to 1.20 W/(m·K).

Downhole temperature and heat flow

Four downhole temperature measurements were attempted using the APCT-3 between 20 and 60 mbsf in Hole U1412A. All measurements were made in a calm sea state. A least-squares linear fit to the temperature data yields a gradient of 114°C/km and a bottom water temperature of 2.25°C (Fig. F28B). The use of a linear fit implies constant thermal conductivity and basal heat flow. Extrapolation of temperature to the base of the hole was not conducted because of the lack of reliable thermal conductivity values within Unit II.

Sediment strength

Compressive sediment strength was measured by the Geotester STCL-5 pocket penetrometer in Units I and II and by a third-party needle penetrometer in Units II and III (see **"Physical properties"** in the "Methods" chapter [Harris et al., 2013]). Shear strength in Unit I was measured by the automated vane shear apparatus. In the uppermost 30 m, compressive strength linearly increases with depth from ~2 to 390 kPa and shear strength increases from 20 to ~180 kPa (Fig. F29). From ~30 to ~180 mbsf, compressive strength values become variable, ranging between ~100 and ~470 kPa, and strength does not increase with depth. Values in Unit III are very scattered. The highest strength of 1980 kPa was observed at ~330 mbsf, where the lowest porosity (~30%) was observed (Fig. F24). Some of the scatter in compressive strength below 30 mbsf may reflect variable disturbance from gas expansion in Unit I and from the small surface area tested by the needle penetrometer.

Electrical conductivity and formation factor

Formation factor was obtained from electrical conductivity measurements in the *y*- and *z*-axes of the split core from the shallow portion of Hole U1412A (0 to ~107.91 mbsf) and in the *z*-axis in Hole U1412B (0.1~6.25 mbsf) (Fig. F30). The *y* and *z* measurements in Hole U1412A are similar throughout the hole, indicating little anisotropy of electrical conductivity within the sediments. Formation factor increases from 1.5 to 3.2 between 0 and 14 mbsf and becomes stable between 14 and ~65 mbsf, ranging between 2.5 and 4.0. Between ~65 and 107.91 mbsf, formation factor decreases with depth. Core disturbance due to gas expansion likely causes some of the observed scatter.

Color spectrophotometry

Reflectance L* values range between 30 and 40 and are similar in Units I and III, whereas reflectance a* and reflectance b* values show a slight shift at 20 mbsf and excursions just below the Unit II/III boundary (Fig. F31).

Paleomagnetism

Four holes were drilled at Site U1412. Cores 344-U1412A-1H through 15H were cored with the APC using nonmagnetic core barrels and oriented with the FlexIT orientation tool. Cores 344-U1412A-16X through 25X were cored with the XCB system. Core 344-U1412B-1H was also cored with the APC, and Cores 344-U1412B-3X through 20X were cored with the XCB. Core 344-U1412B-21 was a drilled interval. Cores 344-U1412C-2R through 7R and 344-U1412D-1R through 3R were cored with the RCB. We measured the remanent magnetization of archive section halves from Cores 344-U1412A-1H through 23X, Core 344-U1412B-1H through Section 11X-1, Sections 344-U1412C-5R-2 through 9R-3, and Sections 344-U1412D-2R-1 through 3R-5. In order to isolate the characteristic remanent magnetization (ChRM), these archive section halves were demagnetized in an alternating field (AF) up to 40 mT and measured with the pass-through superconducting rock magnetometer (SRM) at 2.5 cm intervals. The remaining core sections were not measured because of the poor conditions of the recovered material. In order to verify the section data, we demagnetized 61 discrete samples using progressive AF and thermal demagnetization techniques and measured them in the SRM.

Natural remanent magnetization of cores

Downhole variations of paleomagnetic data obtained at Site U1412 are shown in Figures F32, F33, F34, and F35. The natural remanent magnetization (NRM) intensity for the carbonaceous silty clay to clayey silt of Unit I (204.74–338.50 mbsf; see **"Lithostratigraphy and petrology"**) is on the order of 10^{-2} A/m (Figs. F32, F33). The clayey siltstone of Unit III (338.50–387.00 mbsf) has somewhat lower NRM intensity (on the order of 10^{-3} A/m; Fig. F34). The calcareous ooze with nannofossils and diatoms of Unit II (204.74–338.50 mbsf) has the lowest NRM intensity (on the order of 10^{-4} A/m; Fig. F34). Sediments recovered from Hole U1412D have a mean

NRM intensity of 2.5×10^{-3} A/m (Fig. F35). There are more significant variations in NRM intensity in lithostratigraphic Unit I than in Units II and III. We observed a strong correlation between the variations in magnetic susceptibility and the variations in NRM intensity (see "Physical properties").

A few troughs of lower NRM values appear around ~12 and ~146 mbsf in Unit I (Fig. F32); these troughs can be linked directly to the presence of watery sediments in these intervals and are likely due to drilling disturbances. NRM measurements of discrete samples taken from the nonwatery sediments above and below these intervals (block crosses in Fig. F32) show intensity values that are similar to the section data, confirming that the watery sediments indeed caused the lower NRM troughs in the pass-through records.

Magnetic noise in the SRM and *y*-axis flux jumps

During initial drilling operations at Site U1412, we observed a large increase in the frequency and number of magnetic flux jumps in the *y*-axis superconducting quantum interference device (SQUID). These jumps produced large magnetic noise anomalies and adversely affected the measurements of some sections (see the uniform inclination values at the top of Fig. F33). Discussions with IODP staff helped us find the solution for this anomaly. This magnetic noise is mainly due to the so-called "antenna" effect described originally by Gary Acton and others in the "Assessment of Readiness of the Refurbished D/V *JOIDES Resolution*" (scientific.oceandrilling.org/xmlui/handle/10914/20521/) and most recently by the Expedition 342 scientists (see "Paleomagnetism" in Norris et al., in press). These reports led us to discover that there was a tiny interval (~0.2 cm) between the aluminum foil wrapped on the cable attached to the in-line degausser and the magnetic shielding assembly. The aluminum foil was used to prevent an ambient electromagnetic field (EMF) from interfering with the SRM, but the tiny gap allowed the EMF to be transmitted inside the SRM. Core sections (especially full 1.5 m length sections) acted like an antenna or wire that conducts the EMF along its length to the SQUID sensors, in a process termed radio-frequency magnetic induction. We rewrapped the power cable attached to the in-line degausser with new aluminum foil and taped the foil to the shielding assembly to make sure the foil was electrically grounded. The magnetic noise decreased immediately, and no major flux jumps were noticed after this grounding. Nevertheless, small flux jumps still exist and are believed to be caused by random disturbances from wiring in the laboratory and fluctuations in ship's power during heavy operations on the rig floor. At present, we cannot prevent this kind of magnetic noise except by repeating the measurement where the small flux jumps occurred. In most cases, the repeated measurements were improved and free of the flux jumps.

Paleomagnetic demagnetization results

As with cores recovered from other Expedition 344 sites, remagnetization imparted by the coring process is common. NRM inclinations are strongly biased toward the vertical (mostly toward +90°) in a majority of cores. Upon AF demagnetization to 40 mT, a significant decrease in intensity (about an order of magnitude; Fig. F32) and a shift of inclination toward shallower values were observed. The inclinations from APC cores (at depths shallower than ~108 mbsf) come close to the expected time-averaged geomagnetic field inclination at this site (approximately ±18°), whereas the inclinations from XCB cores remain much steeper (~50°–60°). It is clear that the maximum level of AF demagnetization (40 mT) we applied was not enough to remove the overprints entirely. An example of good-quality AF demagnetization results is shown in Figure F36.

We demagnetized 61 discrete samples (43 from Hole U1412A, 9 from Hole U1412B, 7 from Hole U1412C, and 2 from Hole U1412D), using stepwise AF and thermal demagnetization (Figs. F32, F33, F34, F35). After removal of the drilling-induced component, the ChRMs of both normal and reversed polarities were observed for most of the samples (Fig. F34). A pair of sister samples was treated by AF and thermal demagnetization. The AF demagnetized sample displayed high resistance to AF demagnetization to 120 mT, and the thermally demagnetized sample showed unblocking temperature between 650° and 675°C, indicating that the main magnetic carrier (probably hematite) in this sample has a high Curie temperature and high coercivity. ChRM inclinations of discrete samples obtained from principal component analysis (PCA; Kirschvink, 1980) for the four holes are plotted in Figures F32, F33, F34, and F35.

Implications for magnetostratigraphy

We used ChRM inclinations and declinations from both discrete and pass-through measurements to define magnetic polarity sequences (Fig. F37). We recognize seven magnetozones in Hole U1412A. These magnetozones are defined as intervals with multiple consecutive samples with polarities that are distinctly different from neighboring intervals. The upper part of Hole U1412A is characterized by two reversed zones (R1 and R2) and three normal polarity zones (N1, N2, and N3). The lower part of the hole is characterized by one long normal interval (N4) and

one reversed interval (R3). Shipboard micropaleontological studies indicate that the base of Hole U1412A (Core 344-U1412A-17X) is close to the Zone NN19/NN18 boundary (~1.9 Ma), the middle part of the hole (Core 6H) is younger than 1.3 Ma, and the uppermost two cores (Cores 1H and 2H) may be within Zone NN21 (younger than 0.29 Ma) (see **"Paleontology and biostratigraphy"**). Using these age points as a guide to correlate the observed magnetozones with those in the Gradstein et al. (2012) geomagnetic polarity timescale, we interpreted N1 as the upper part of the Brunhes Chron and N2 and N3 as the Jaramillo and Cobb Mountain Subchrons, respectively. Consequently, the long normally magnetized Zone N4 is likely the Olduvai Subchron (1.788–1.945 Ma) with its upper boundary placed at ~92 mbsf (Fig. **F37**). If true, this would suggest extremely high sediment accumulation rates for Hole U1412A, similar to those in Hole U1379C. Shore-based radiometric dating on tephra layers within Unit I (i.e., ~25 and 95 mbsf; Fig. **F32**) will provide an independent check on the age assignments based on magnetostratigraphic and biostratigraphic results.

Paleomagnetic measurements of nine discrete samples from Hole U1412B display a change from normal to reversed polarity at ~167 mbsf (Fig. **F33**). Changes in inclination sign are also observed for the seven samples studied from Hole U1412C (Fig. **F34**). Two discrete samples from Hole U1412D were measured for shipboard structural analyses (Fig. **F35**). Because of the small number of samples, we have no magnetostratigraphic interpretations at this time. Shore-based integrated work with micropaleontological data and paleomagnetic studies of discrete samples from each hole are required to estimate the timing and origin of the magnetization recorded by the sediments at Site U1412.

References

Chan, L.-H., and Kastner, M., 2000. Lithium isotopic compositions of pore fluids and sediments in the Costa Rica subduction zone: implications for fluid processes and sediment contribution to the arc volcanoes. *Earth Planet. Sci. Lett.,* 183(1–2):275–290. **doi:10.1016/S0012-821X(00)00275-2**

Fontanier, C., Jorissen, F.J., Licari, L., Alexandre, A., Anschutz, P., and Carbonel, P., 2002. Live benthic foraminiferal faunas from the Bay of Biscay: faunal density, composition, and microhabitats. *Deep-Sea Res., Part I,* 49(4):751–785. **doi:10.1016/S0967-0637(01)00078-4**

Gradstein, F.M., Ogg, J.G., Schmitz, M.D., and Ogg, G.M. (Eds)., 2012. *The Geological Time Scale 2012:* Amsterdam (Elsevier).

Harris, R.N., Sakaguchi, A., Petronotis, K., Baxter, A.T., Berg, R., Burkett, A., Charpentier, D., Choi, J., Diz Ferreiro, P., Hamahashi, M., Hashimoto, Y., Heydolph, K., Jovane, L., Kastner, M., Kurz, W., Kutterolf, S.O., Li, Y., Malinverno, A., Martin, K.M., Millan, C., Nascimento, D.B., Saito, S., Sandoval Gutierrez, M.I., Screaton, E.J., Smith-Duque, C.E., Solomon, E.A., Straub, S.M., Tanikawa, W., Torres, M.E., Uchimura, H., Vannucchi, P., Yamamoto, Y., Yan, Q., and Zhao, X., 2013. Methods. *In* Harris, R.N., Sakaguchi, A., Petronotis, K., and the Expedition 344 Scientists, *Proc. IODP,* 344: College Station, TX (Integrated Ocean Drilling Program). **doi:10.2204/iodp.proc.344.102.2013**

Kamikuri, S., Motoyama, I., Nishi, H., and Iwai, M., 2009. Neogene radiolarian biostratigraphy and faunal evolution rates in the eastern equatorial Pacific ODP Sites 845 and 1241. *Acta Palaeontol. Pol.,* 54(4):713–742. **doi:10.4202/app.2008.0076**

Kirschvink, J.L., 1980. The least-squares line and plane and the analysis of palaeomagnetic data. *Geophys. J. R. Astron. Soc.,* 62(3):699–718. **doi:10.1111/j.1365-246X.1980.tb02601.x**

Norris, R.D., Wilson, P.A., Blum, P., Fehr, A., Agnini, C., Bornemann, A., Boulila, S., Bown, P.R., Cournede, C., Friedrich, O., Ghosh, A.K., Hollis, C.J., Hull, P.M., Jo, K., Junium, C.K., Kaneko, M., Liebrand, D., Lippert, P.C., Liu, Z., Matsui, H., Moriya, K., Nishi, H., Opdyke, B.N., Penman, D., Romans, B., Scher, H.D., Sexton, P., Takagi, H., Turner, S.K., Whiteside, J.H., Yamaguchi, T., and Yamamoto, Y., in press. Site U1405. *In* Norris, R.D., Wilson, P.A., Blum, P., and the Expedition 342 Scientists, *Proc. IODP,* 342: College Station, TX (Integrated Ocean Drilling Program). **doi:10.2204/iodp.proc.342.106.2014**

Sanfilippo, A., and Nigrini, C., 1998. Code numbers for Cenozoic low latitude radiolarian biostratigraphic zones and GPTS conversion tables. *Mar. Micropaleontol.,* 33(1–2):109–117, 121–156. **doi:10.1016/S0377-8398(97)00030-3**

Torres, M.E., Bohrmann, G., and Suess, E., 1996. Authigenic barites and fluxes of barium associated with fluid seeps in the Peru subduction zone. *Earth Planet. Sci. Lett.,* 144(3–4):469–481. **doi:10.1016/S0012-821X(96)00163-X**

van Morkhoven, F.P.C.M., Berggren, W.A., Edwards, A.S., and Oertli, H.J., 1986. Cenozoic cosmopolitan deep-water benthic foraminifera. *Bull. Cent. Rech. Explor.—Prod. Elf-Aquitaine,* 11.

Zijderveld, J.D.A., 1967. AC demagnetization of rocks: analysis of results. *In* Collinson, D.W., Creer, K.M., and Runcorn, S.K. (Eds.), *Methods in Palaeomagnetism:* Amsterdam (Elsevier), 254–286.

Publication: 11 December 2013
MS 344-105

Figure F1. Detail of poststack time-migrated seismic Line BGR99-7 centered at Site U1412. Prestack depth migration from C.R. Ranero (unpubl. data). BSR = bottom-simulating reflector.

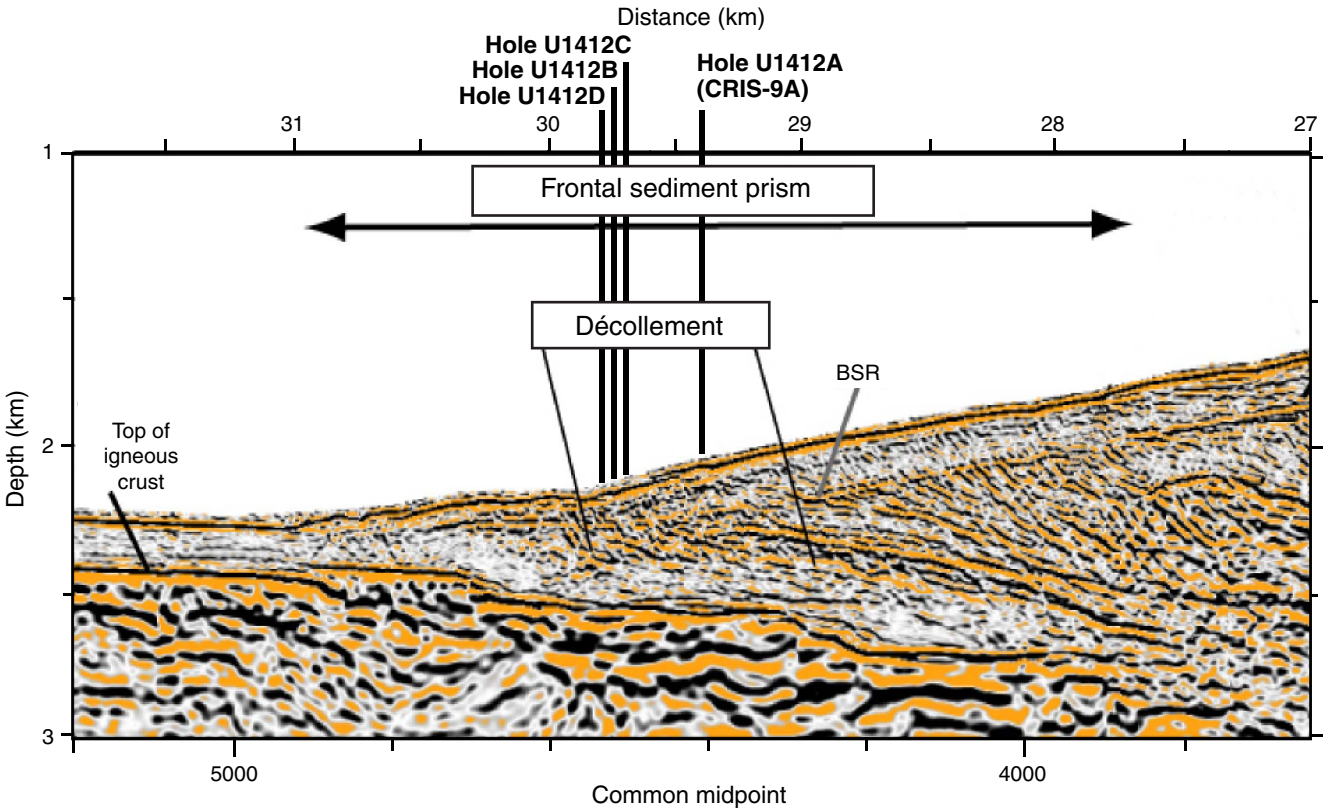

Figure F2. Location of Expedition 344 drill sites. Red diamonds denote Expedition 344 sites (U1380, U1381, and U1412–U1414), and yellow diamonds denote Expedition 334 sites not occupied during Expedition 344 (U1378, U1379). Red lines = 3-D seismic survey, black lines = seismic reflection lines. Numbers along the short and long axes of the 3-D survey represent inlines and crosslines, respectively.

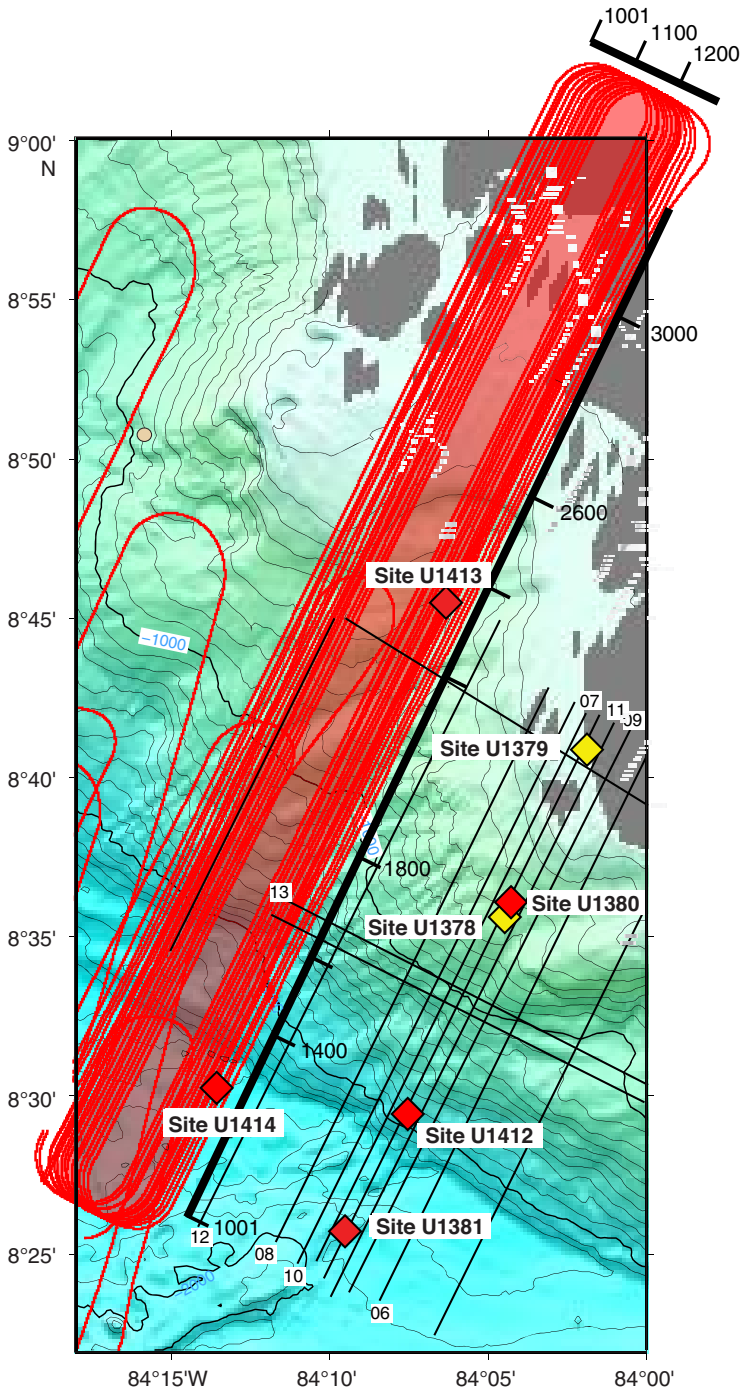

Figure F3. Lithostratigraphic summary of Site U1412.

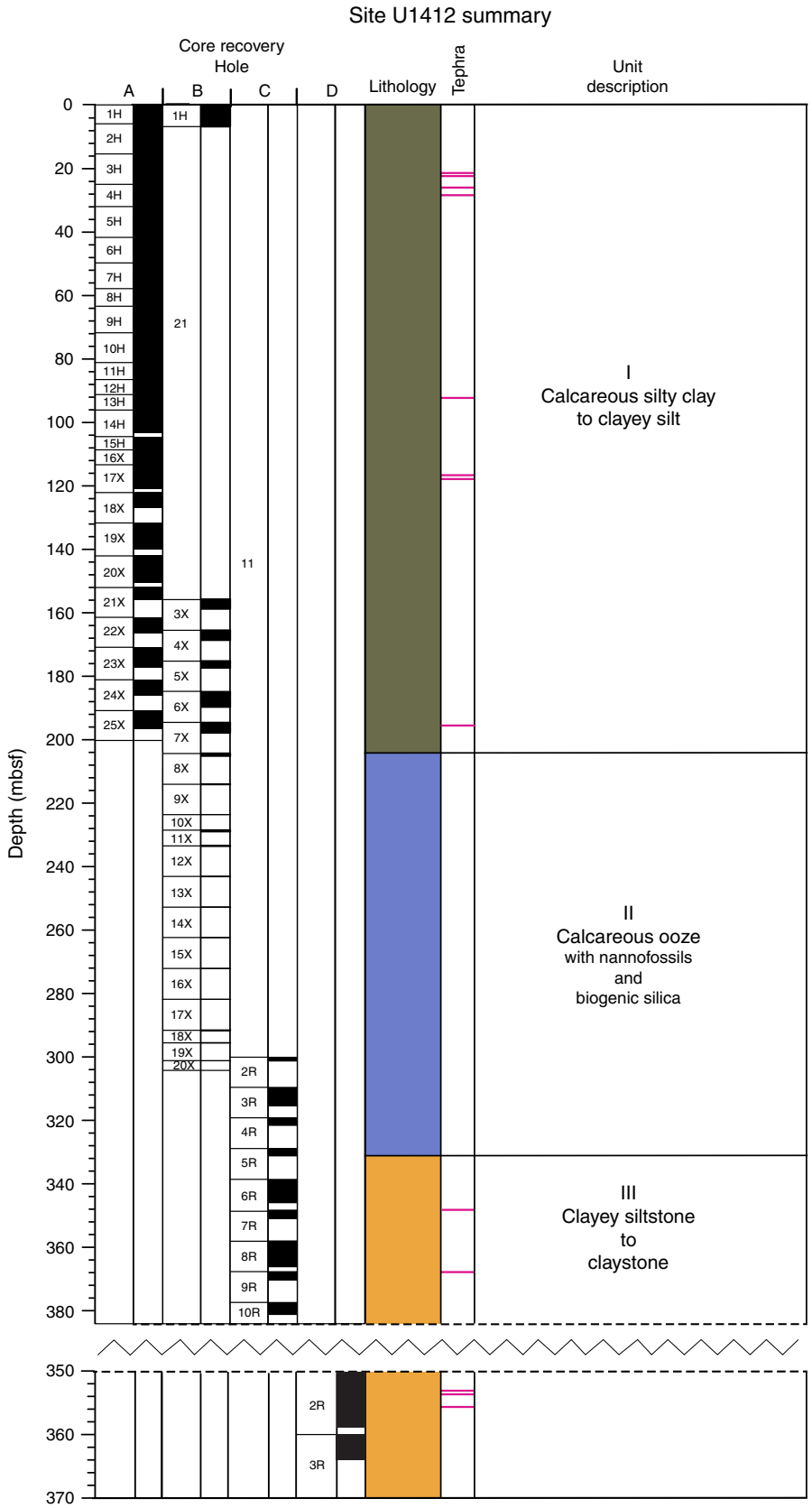

Figure F4. Digital image of dark greenish gray clay lithology representative of Unit I (interval 344-U1412A-2H-6A, 32–44 cm). Note the small (millimeter size) pods filled with sponge spicules widely disseminated throughout the unit.

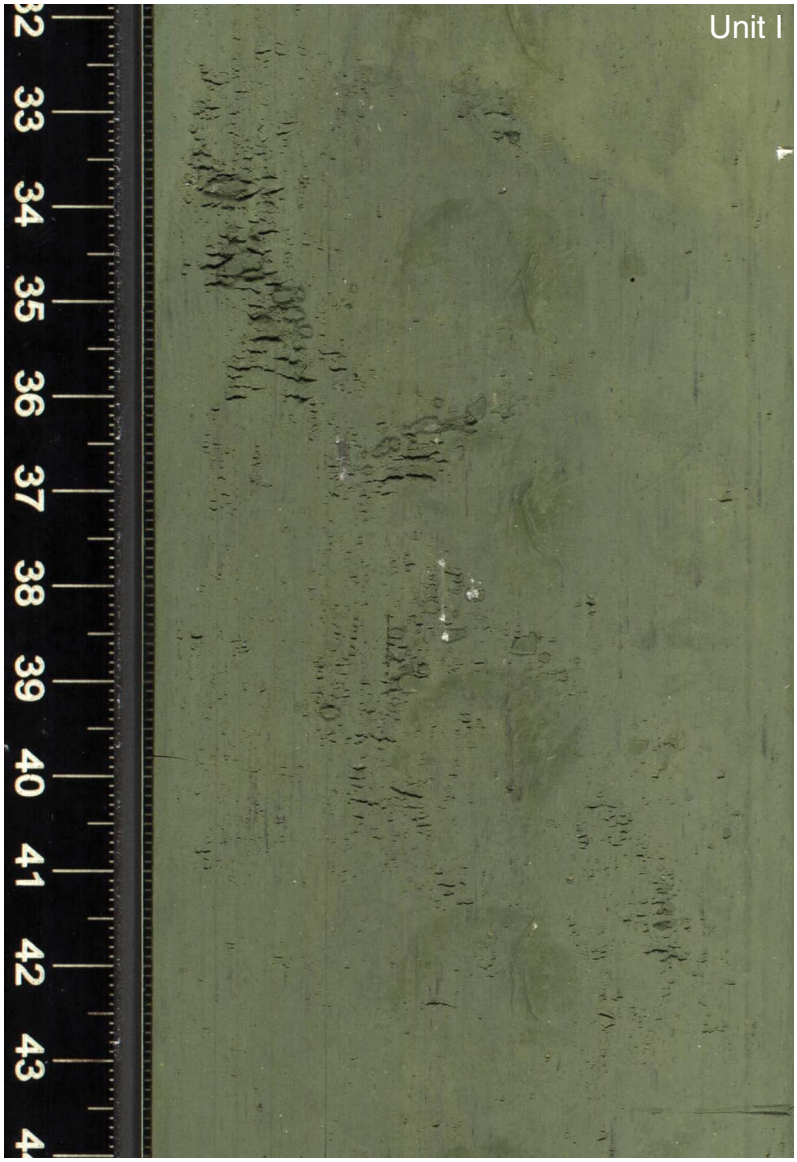

Figure F5. Digital image of one of the dark greenish gray tephra layers intercalated throughout the Unit I sediment (interval 344-U1412A-17X-3A, 40–61 cm). Note the sharp to gradational upper contact and the sharp lower contact, characteristic of the tephras in this unit.

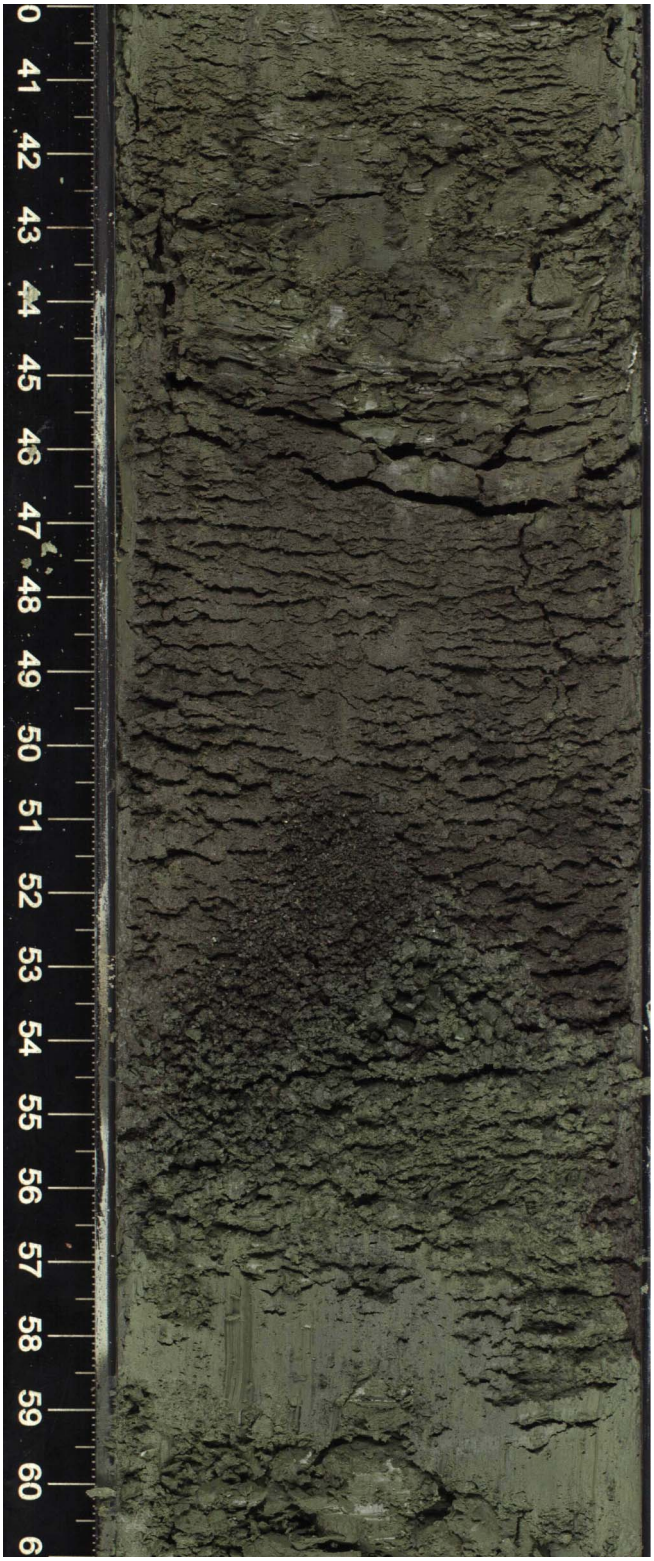

Figure F6. Digital image of glauconite-rich layer (interval 344-U1412A-2H-1A, 70–89 cm).

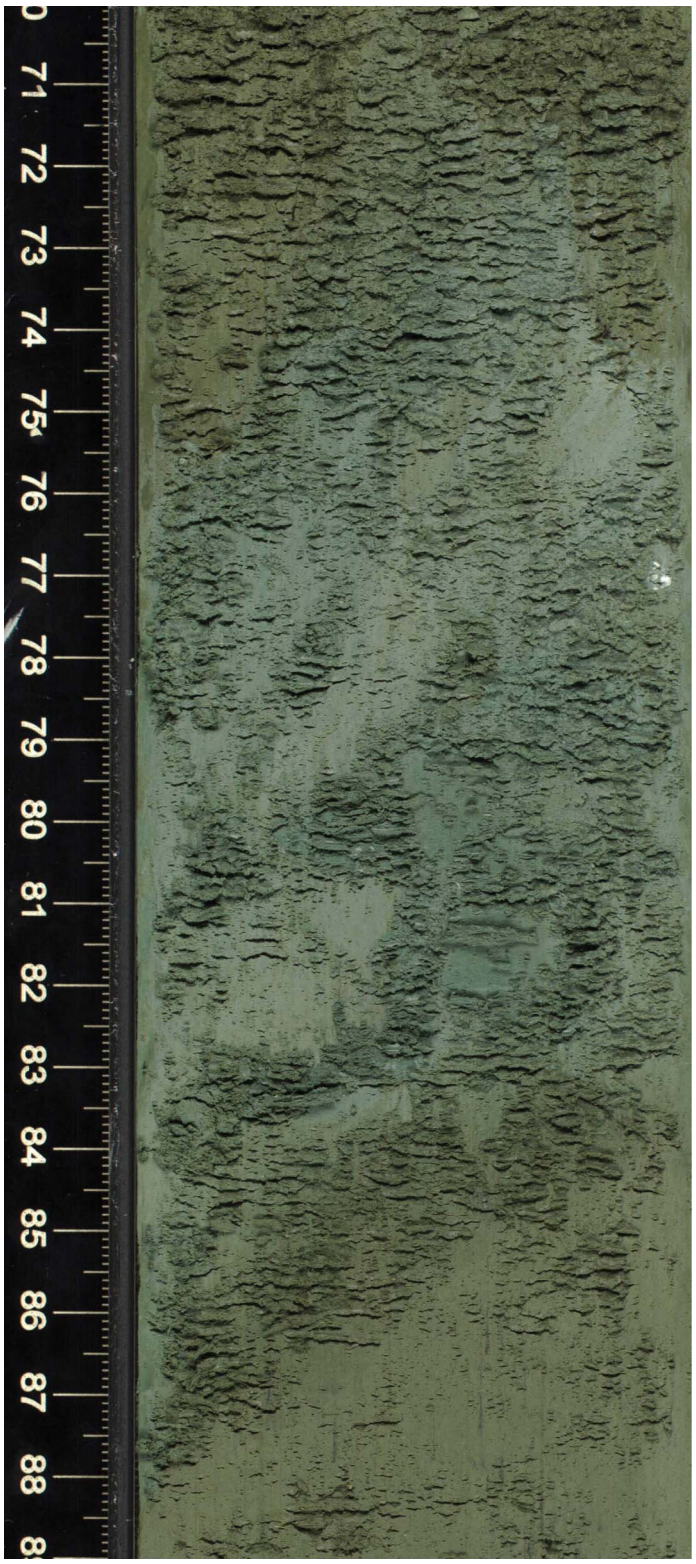

Figure F7. Digital image of the boundary between Unit I and Unit II with a thin glauconite layer marking the transition (interval 344-U1412B-8X-1A, 36–75 cm).

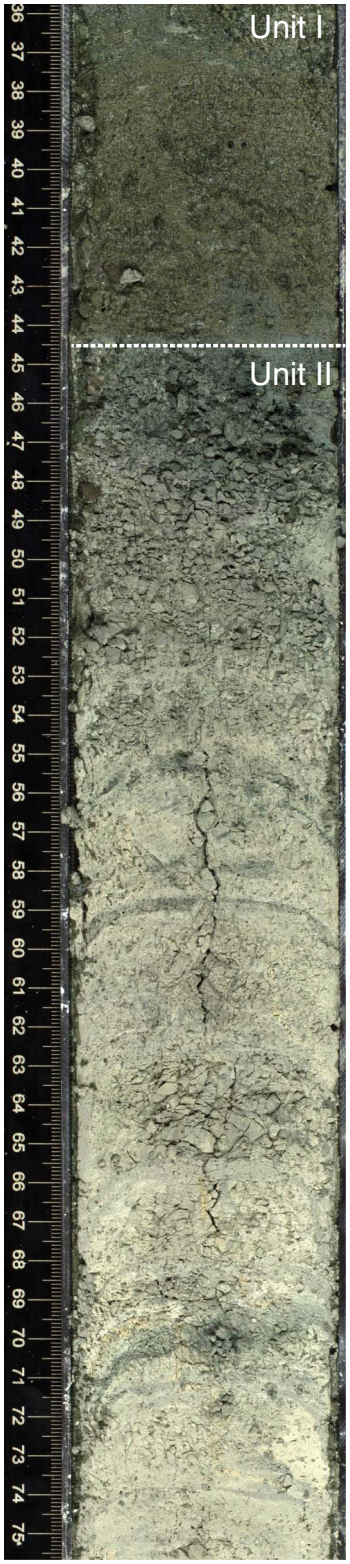

Figure F8. Digital image of light grayish brown diatomaceous ooze from the top of Unit II, which gives way to the darker grayish brown nannofossil ooze that dominates the unit (interval 344-U1412B-8X-CCA, 0–32 cm).

Figure F9. Digital image of well-consolidated calcareous clayey siltstone that characterizes Unit III (interval 344-U1412C-5R-3A, 49–69 cm). Note the dark brown reworked sedimentary lithic fragments.

Figure F10. Digital image of sharp, irregular contact between greenish clayey siltstone (top) and a well-consolidated dark gray tephra layer (bottom) in the highly bioturbated Unit III (interval 344-U1412C-9R-2A, 0–17 cm).

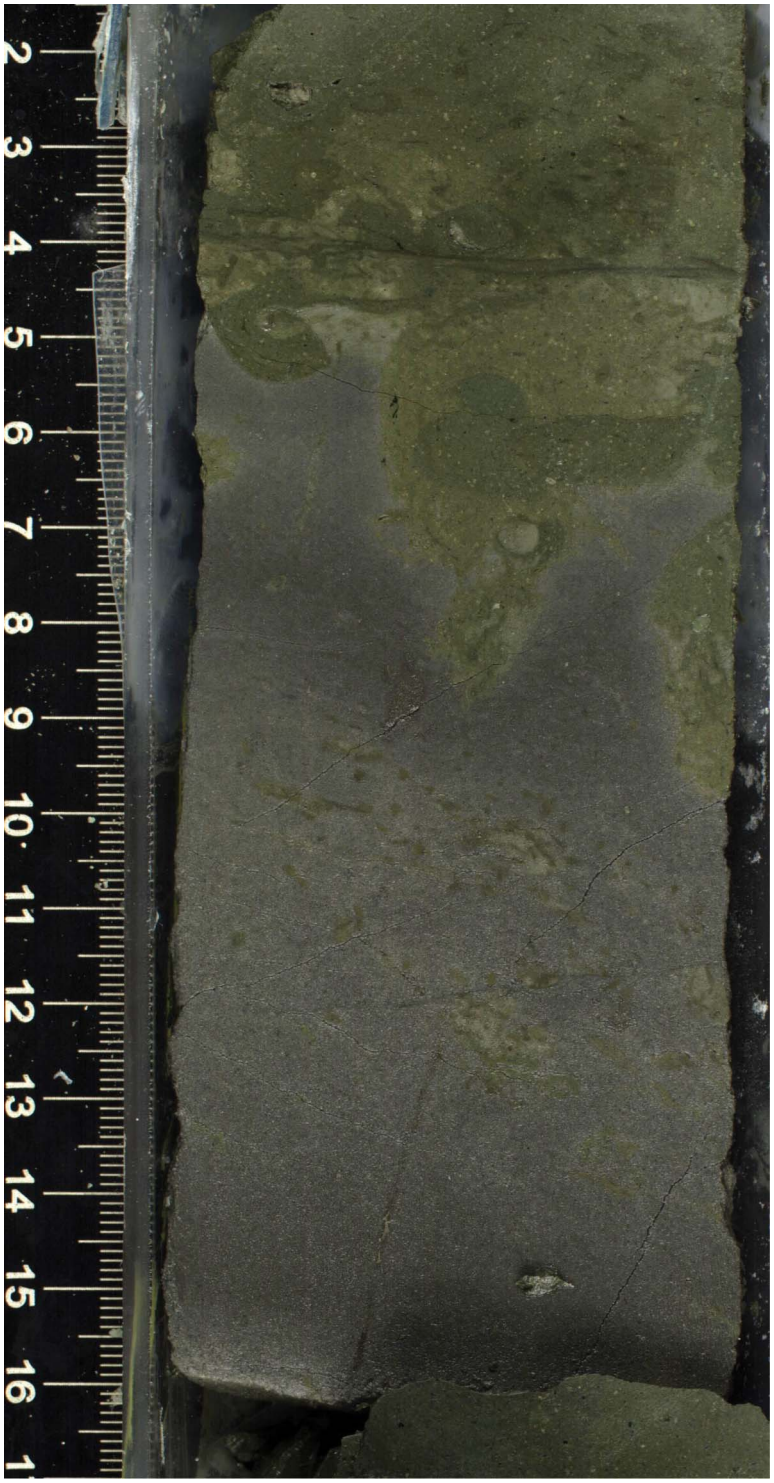

Figure F11. Typical XRD patterns obtained for bulk rock samples, Site U1412. A = analcime, C = calcite, Chl = chlorite (clinochlore), D = dolomite, H = heulandite, Ha = halite, Ho = hornblende, L = laumontite, P = plagioclase, Py = pyrite, Q = quartz, S = smectite.

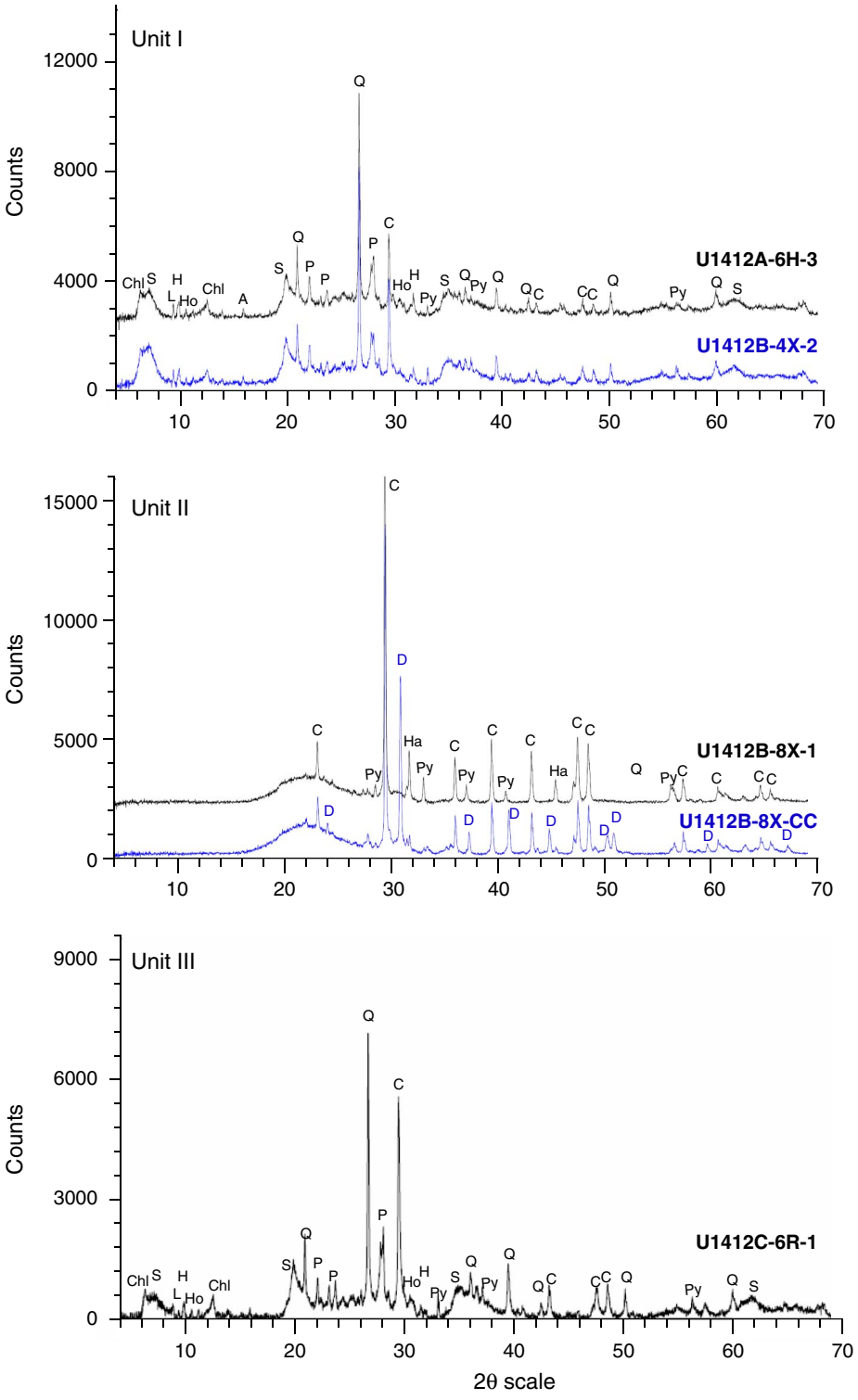

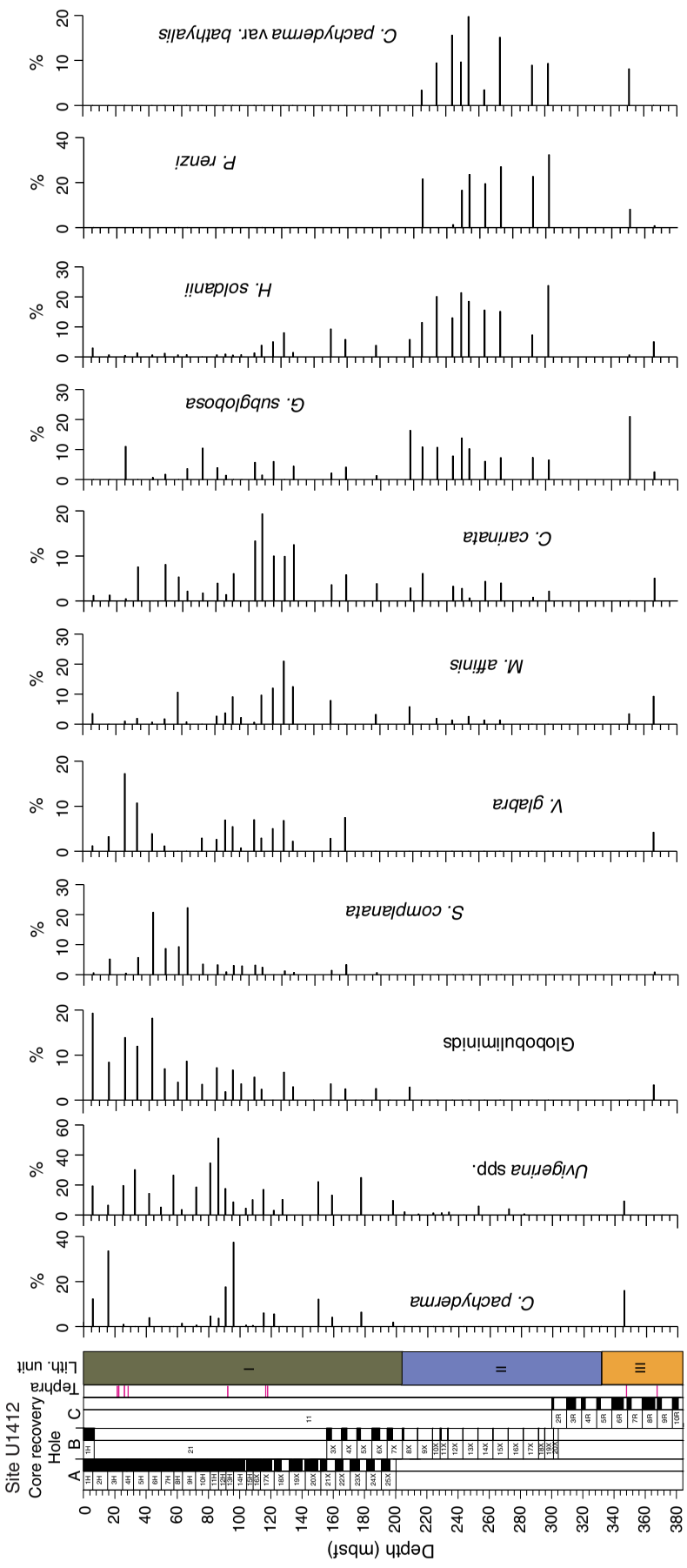

Figure F12. Relative abundance of the most characteristic benthic foraminifer assemblages at Site U1412. Samples containing <100 individuals per sample were not used for relative abundance calculations. *Uvigerina* spp. includes *Uvigerina peregrina* and *Uvigerina auberiana*, and the Globobuliminids group includes *Globobulimina* spp., *Globobulimina affinis*, *Globobulimina auriculata*, *Chilostomella oolina*, *Praeglobobulimina spinescens*, and *Praeglobobulimina ovata*.

Figure F13. Plot of bedding dip angles, dip angles of faults, and other fractures as a function of depth, Site U1412. Purple bands across the figure indicate breccia/fracture zones.

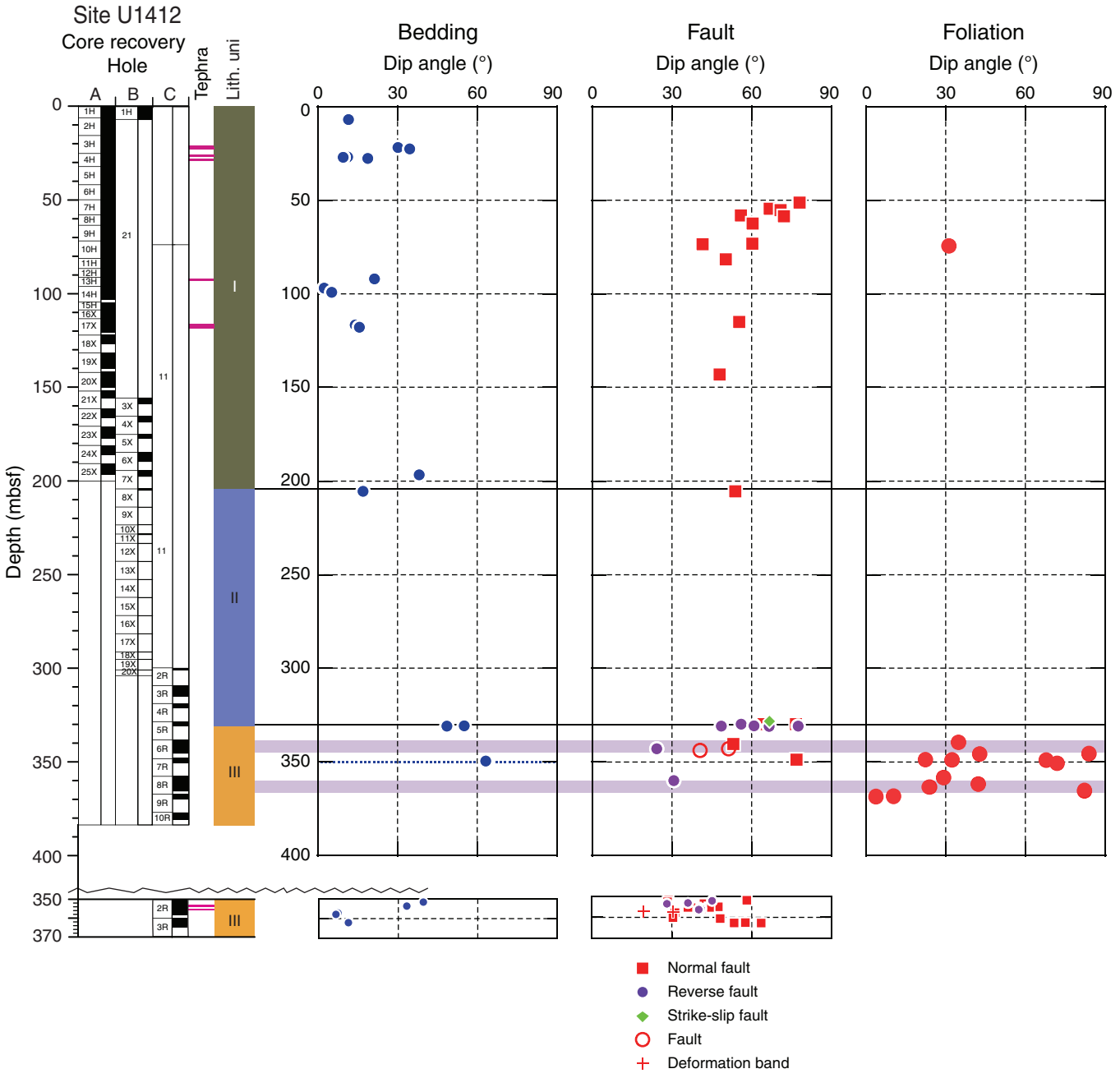

Figure F14. Stereographic diagram showing the orientation of bedding planes, Hole U1412A.

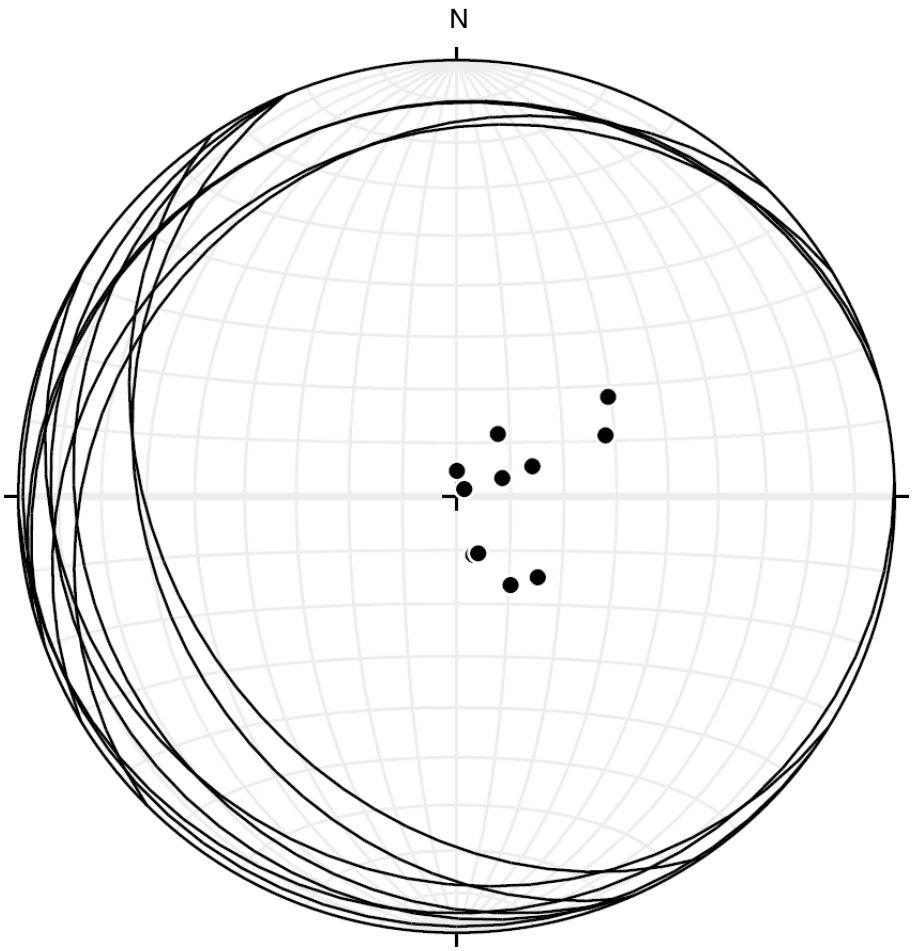

Figure F15. Stereographic diagrams showing (**A**) normal fault planes and lineations and (**B**) fault kinematics analysis, along with related orientation of principal stress axes, Hole U1412A.

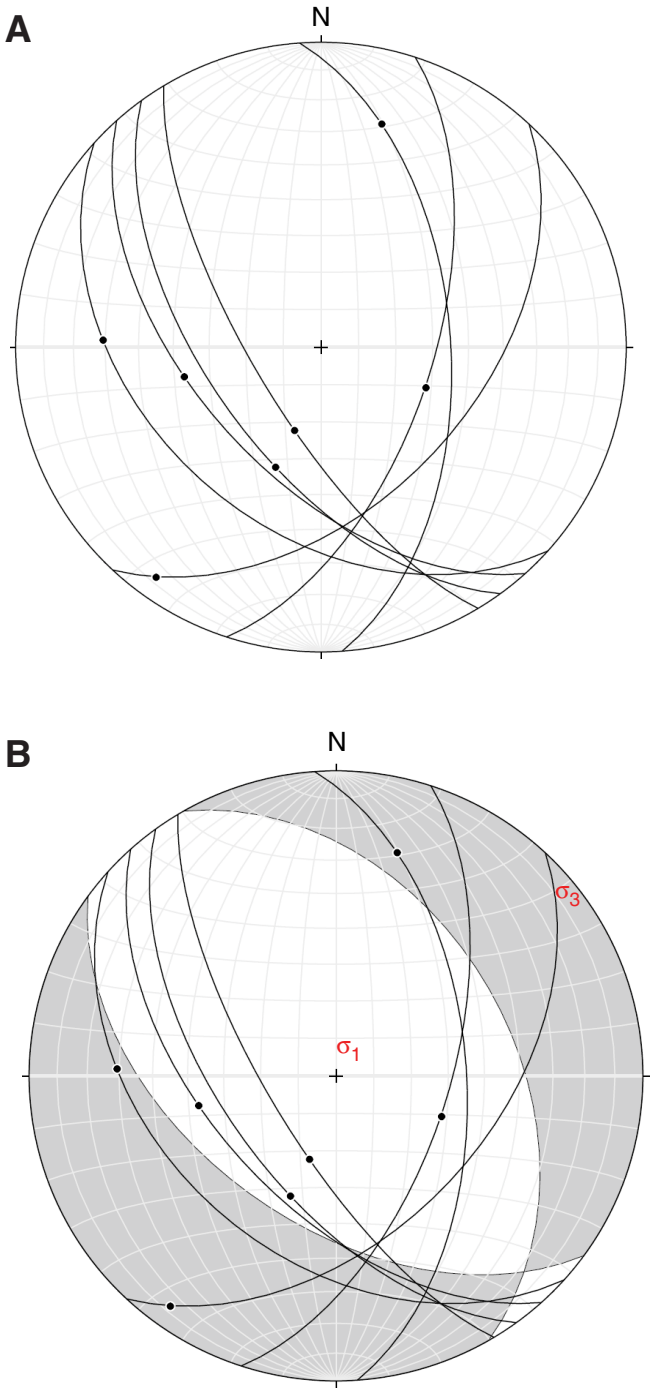

Figure F16. Photograph of a normal fault (interval 344-U1412A-7H-5A, 24–47 cm). The fault plane is marked by a dark color alteration.

Figure F17. Profiles for salinity, chloride, potassium, and sodium, Site U1412. Dashed lines = lithostratigraphic unit boundaries. Blue arrows = bottom seawater values. BSR = bottom-simulating reflector.

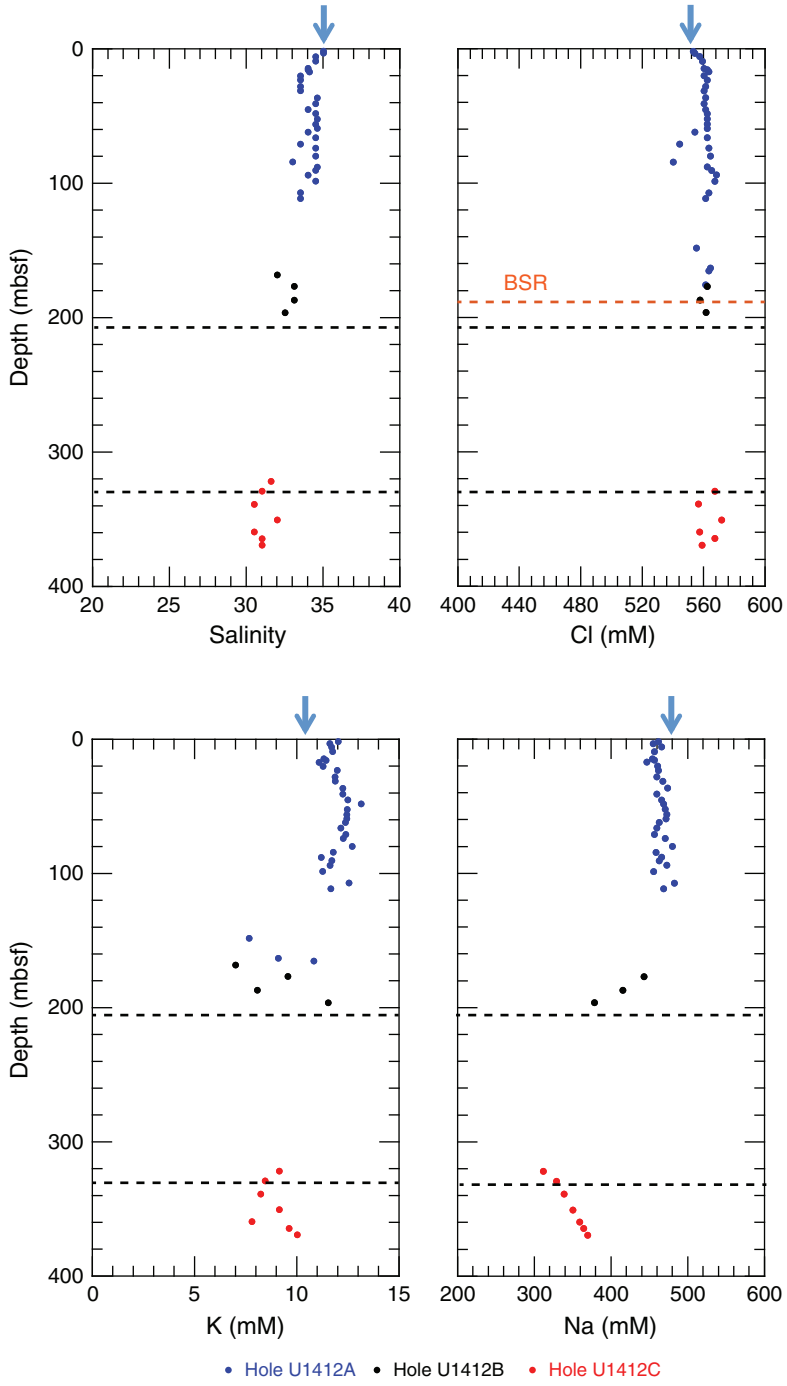

Figure F18. Profiles for sulfate, methane, and barium in the uppermost 30 m of Hole U1412A. The sulfate–methane transition zone (SMTZ) is the horizon where sulfate is consumed and methane begins to increase with depth. Barium also shows a marked increase below the SMTZ as barite dissolves in pore waters devoid of sulfate.

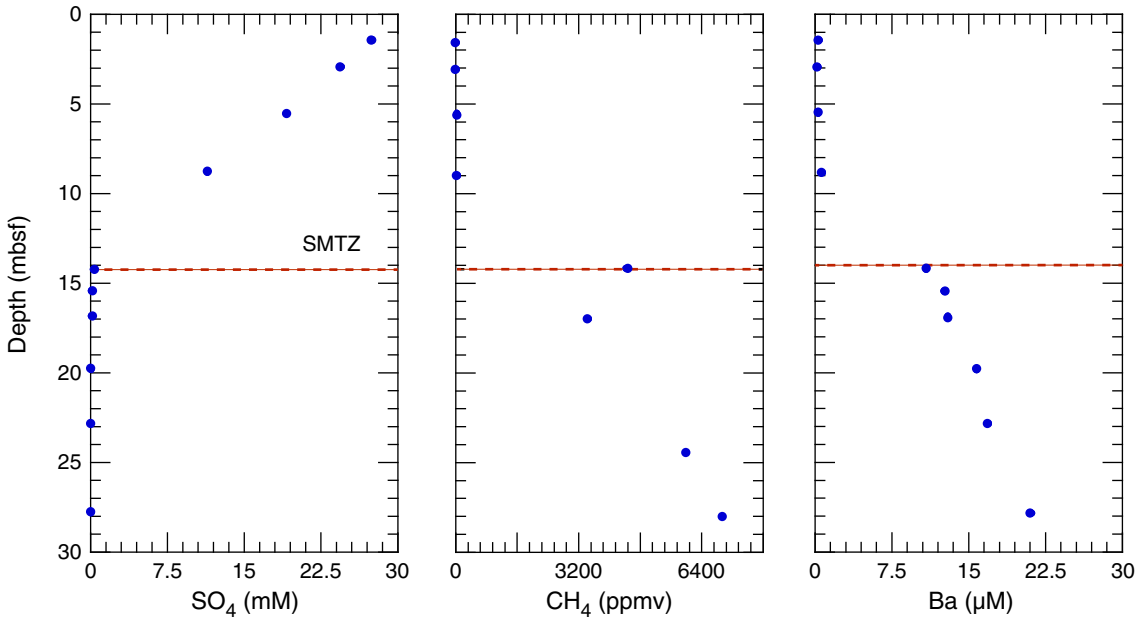

Figure F19. Profiles for alkalinity, calcium, magnesium, sulfate, ammonium, and phosphate, Site U1412. Dashed lines = lithostratigraphic unit boundaries. Blue arrows = bottom seawater values.

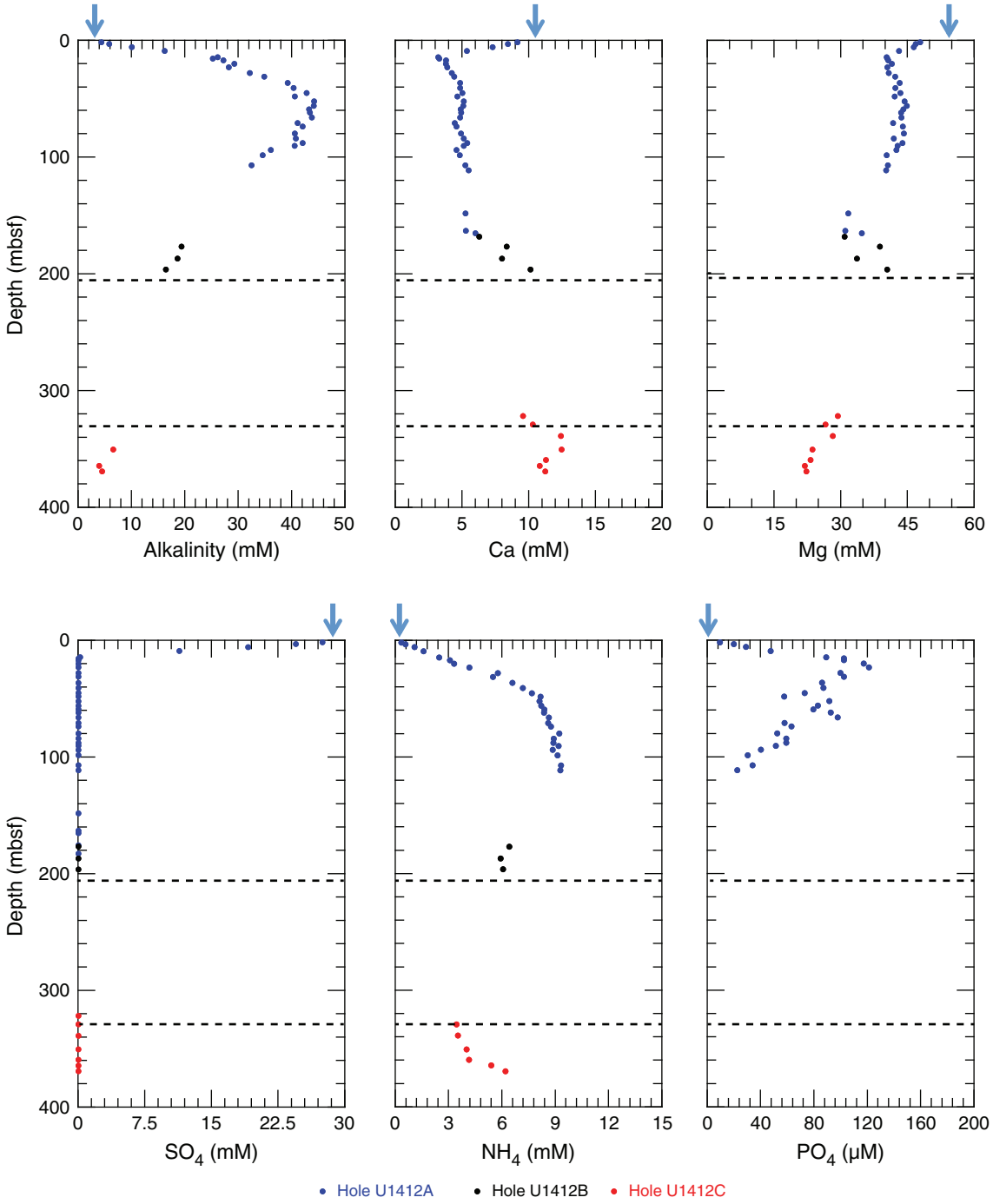

Figure F20. Profiles for strontium, lithium, manganese, boron, silica, and barium, Site U1412. Dashed lines = lithostratigraphic unit boundaries. Blue arrows = bottom seawater values.

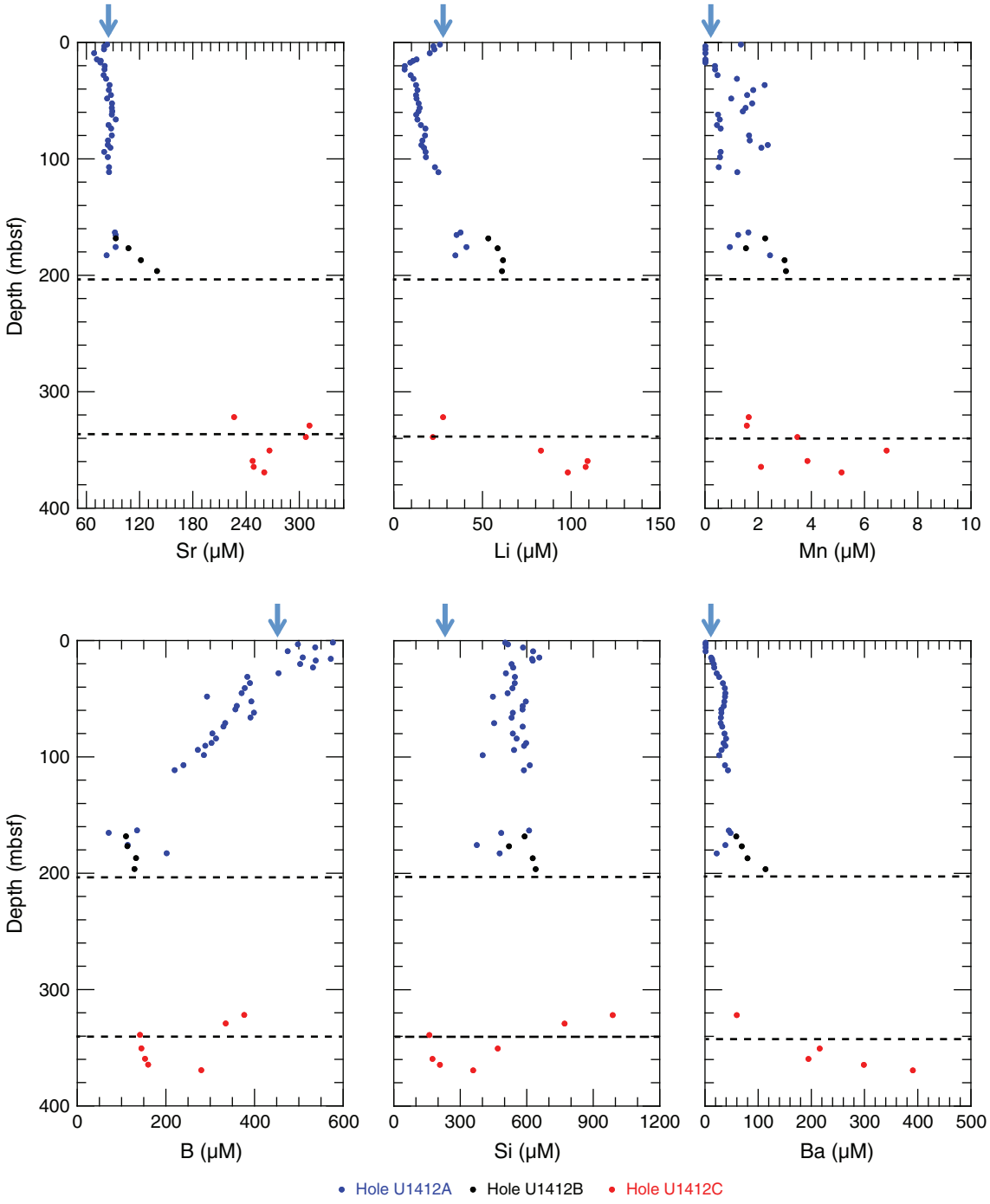

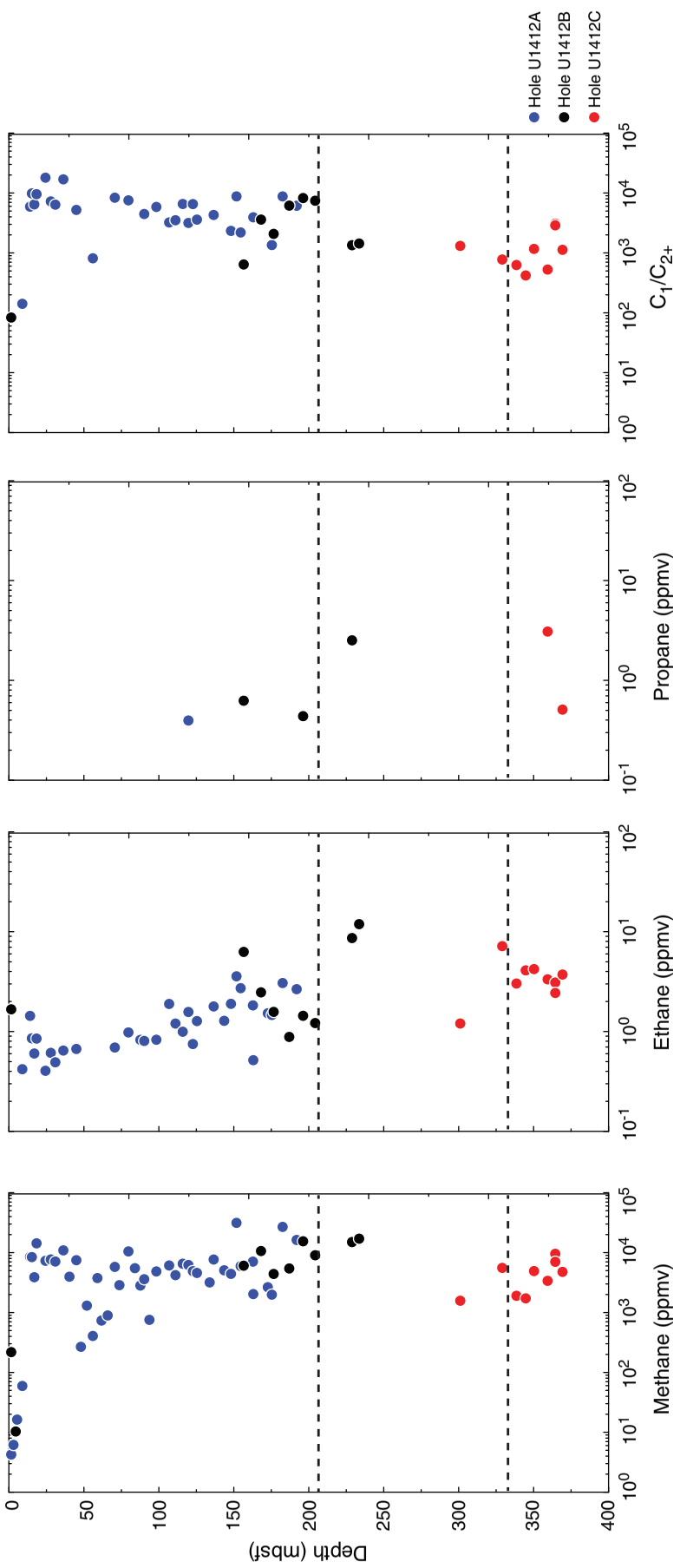

Figure F21. Profiles of hydrocarbons and C_1/C_{2+} ratios in headspace gas samples, Site U1412. Dashed lines = lithostratigraphic unit boundaries.

Figure F22. Profiles of hydrocarbons, CO_2 and C_1/C_{2+} ratios in void gas samples, Holes U1412A and U1412B. Dashed lines = lithostratigraphic unit boundary.

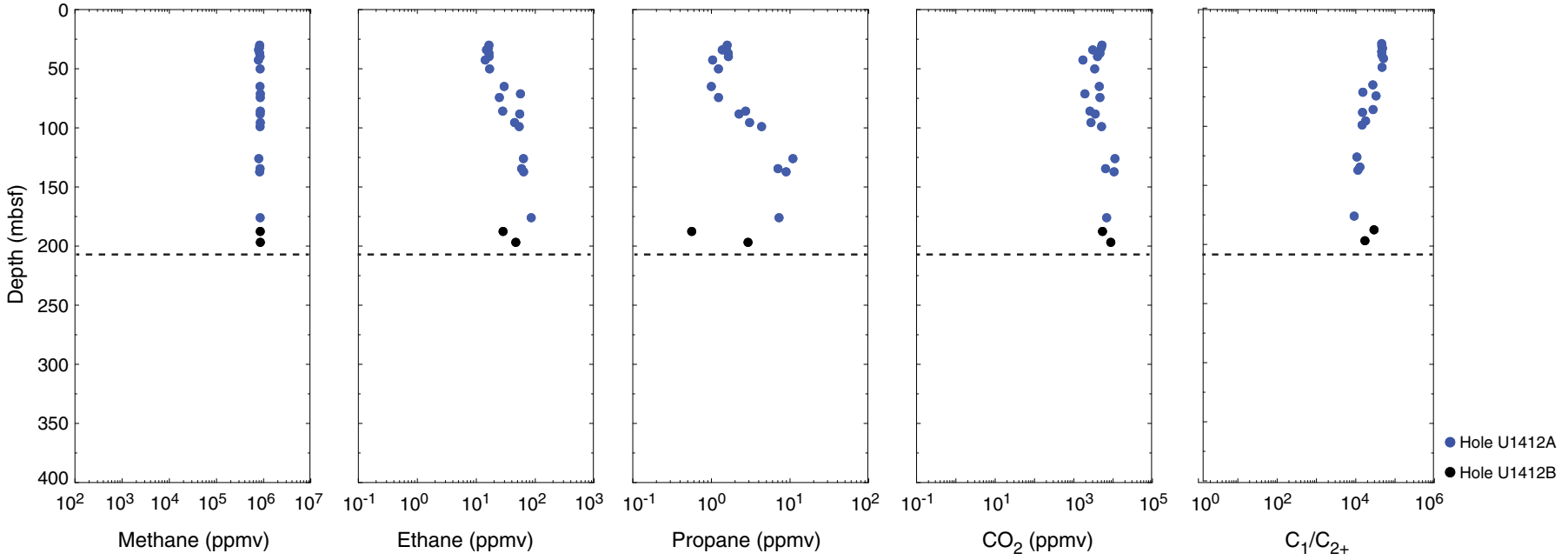

Figure F23. Downhole profiles of total carbon, inorganic carbon, total organic carbon, $CaCO_3$, total nitrogen, and C/N ratio, Site U1412. Dashed lines = lithostratigraphic unit boundaries.

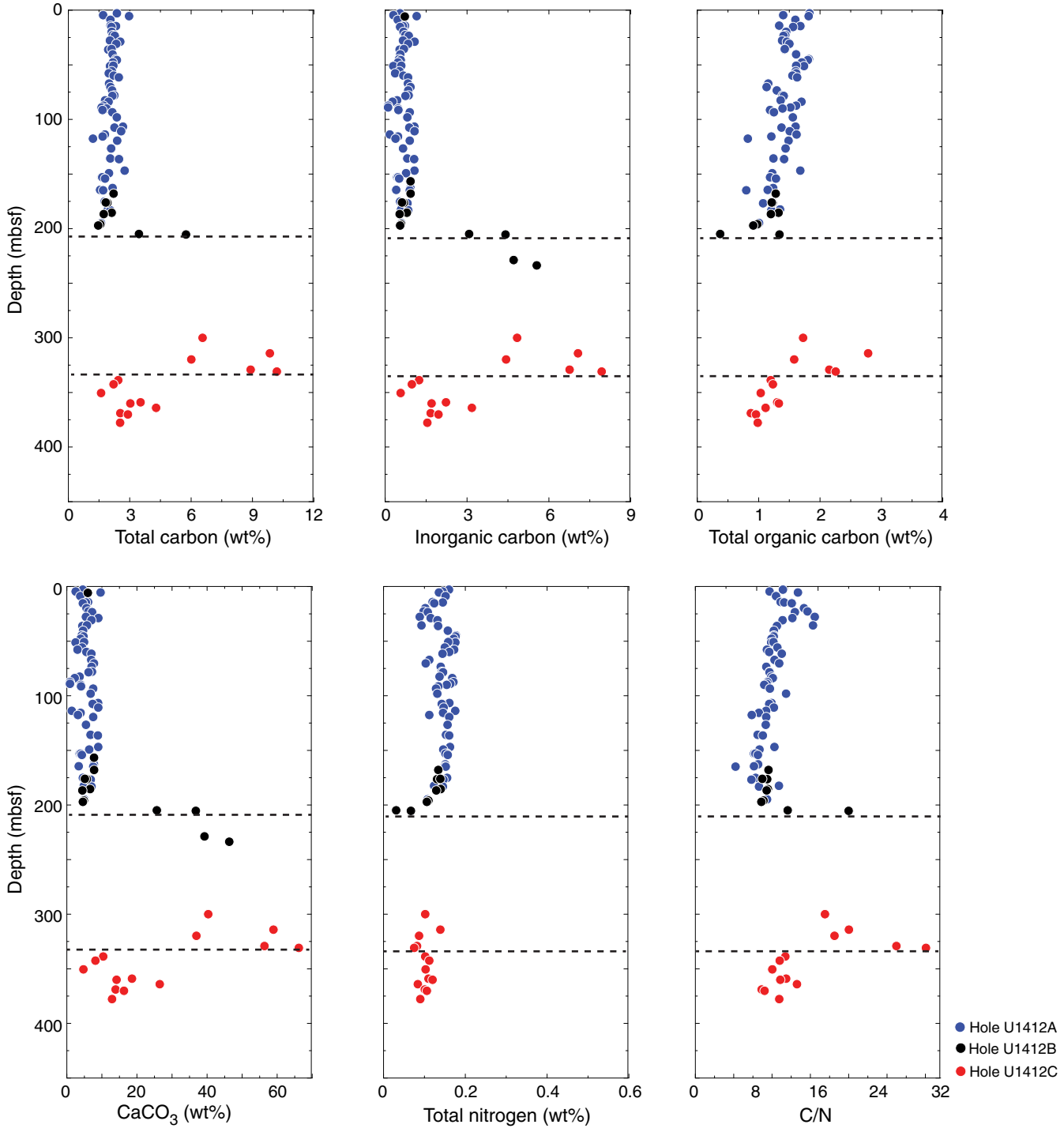

Figure F24. Gamma ray attenuation (GRA) density from the WRMSL and discrete sample porosity and wet bulk density measured using moisture and density (MAD) mass/volume Method C, Site U1412. Horizontal lines = lithostratigraphic unit boundaries.

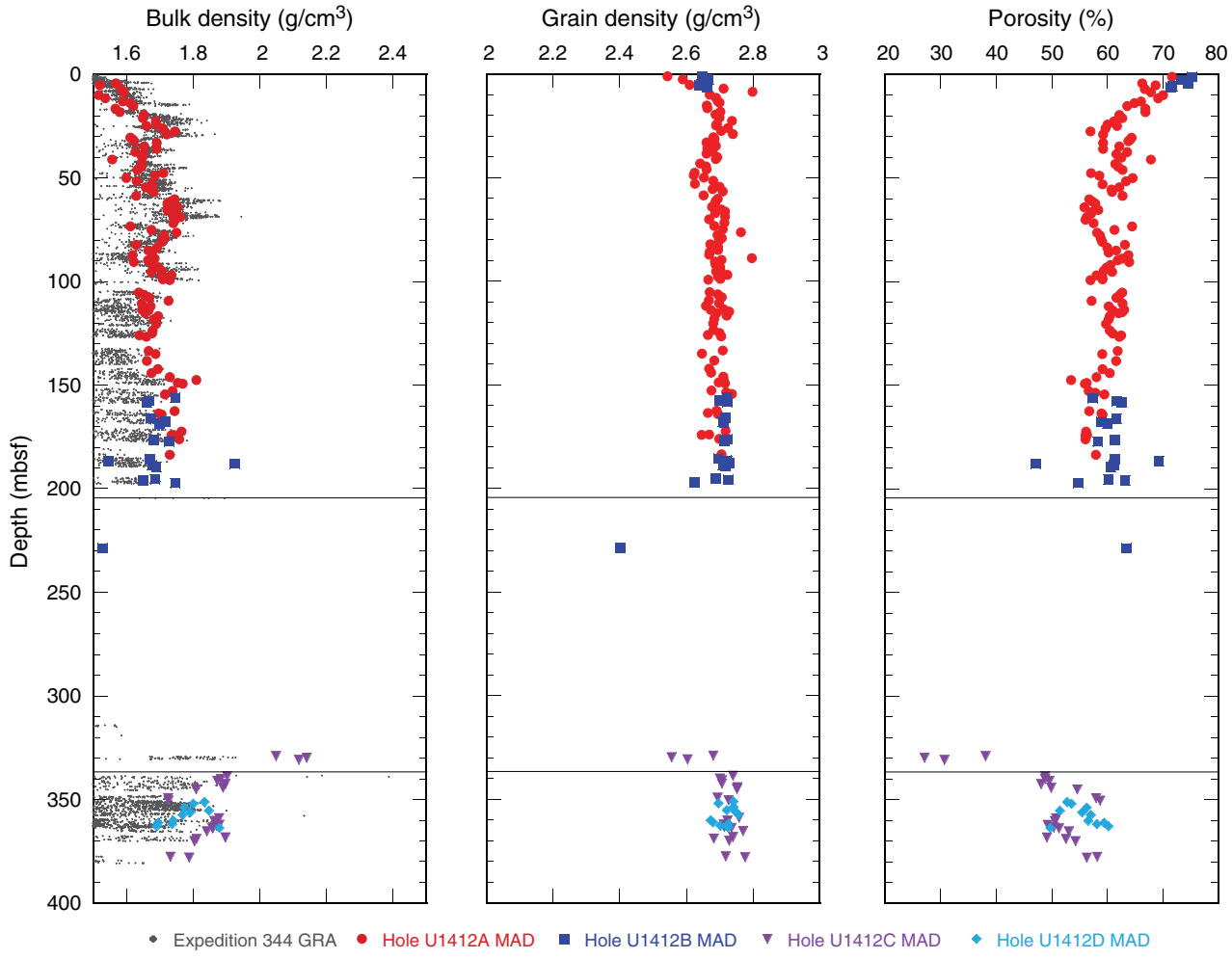

Figure F25. Magnetic susceptibility profiles, Site U1412. WRMSL = Whole-Round Multisensor Logger, SHMSL = Section Half Multisensor Logger. Horizontal lines = lithostratigraphic unit boundaries.

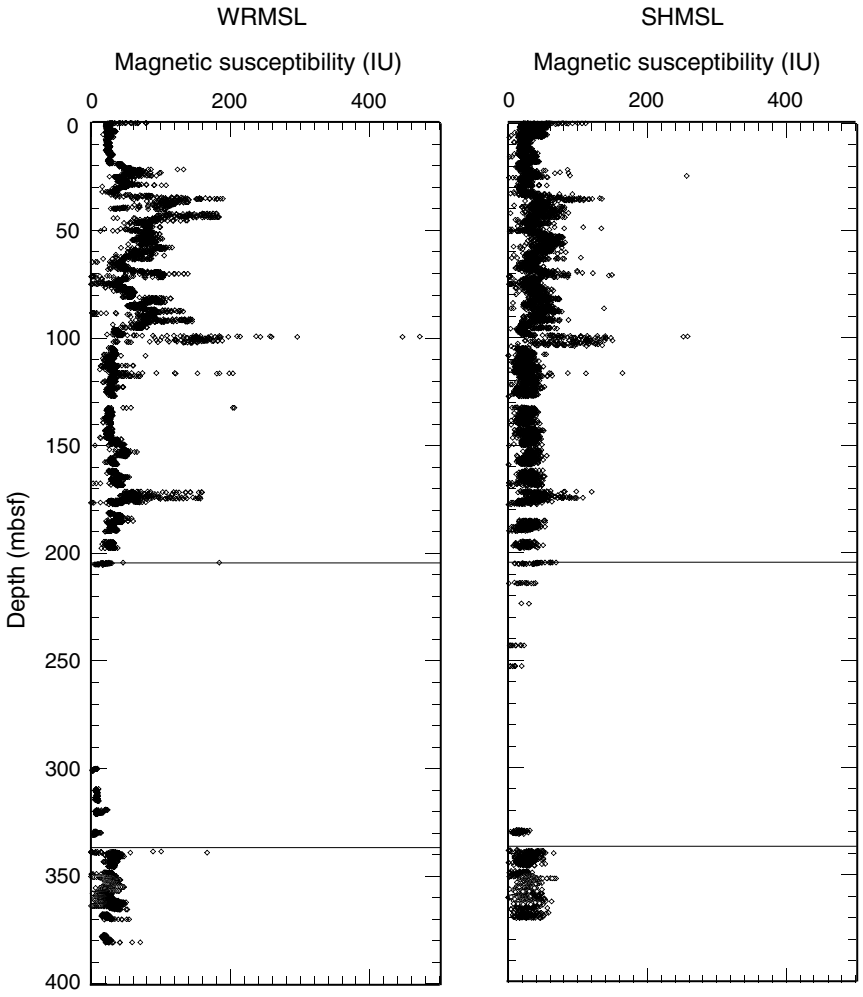

Figure F26. Downhole profile for natural gamma radiation (NGR), Site U1412. Horizontal lines = lithostratigraphic unit boundaries.

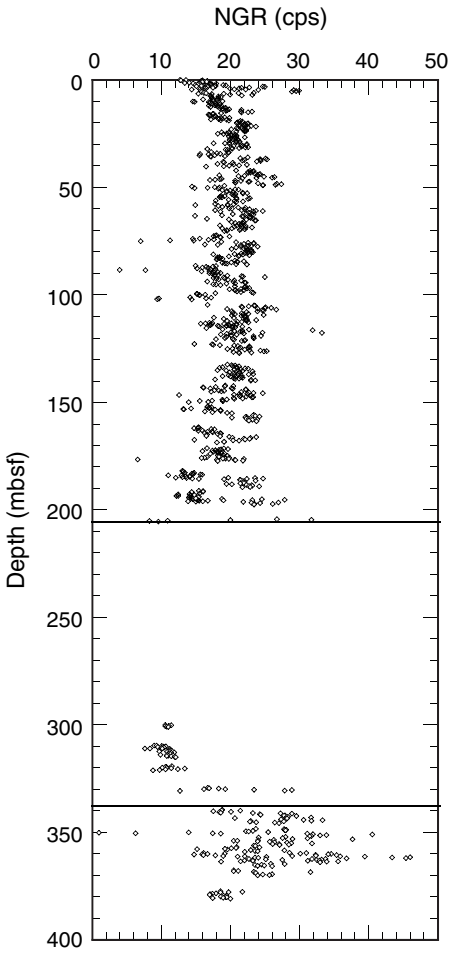

Figure F27. *P*-wave velocity measured on split cores, Site U1412. Horizontal lines = lithostratigraphic unit boundaries.

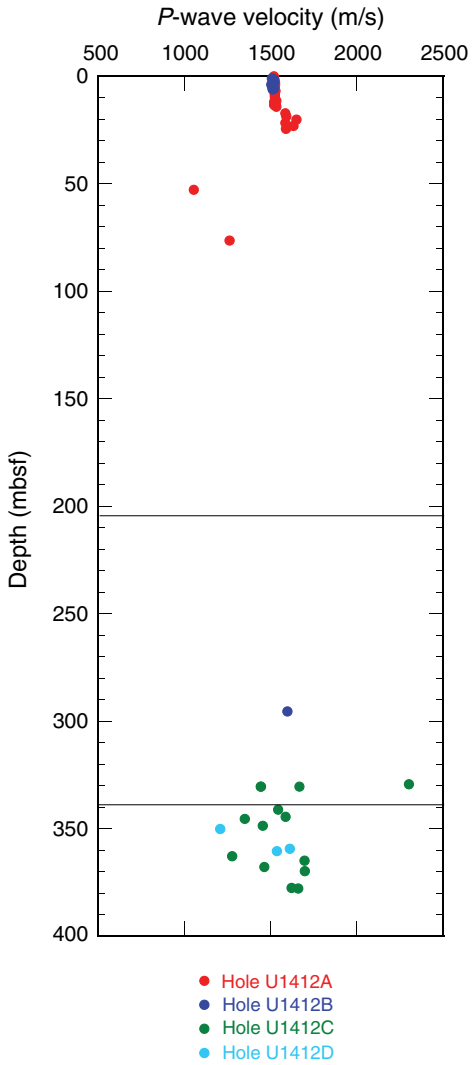

Figure F28. Thermal data, Site U1412. **A.** Thermal conductivity values. **B.** Equilibrium temperatures from Hole U1412A. Dashed line/equation = best linear fit to the temperature data. Horizontal lines = lithostratigraphic unit boundaries.

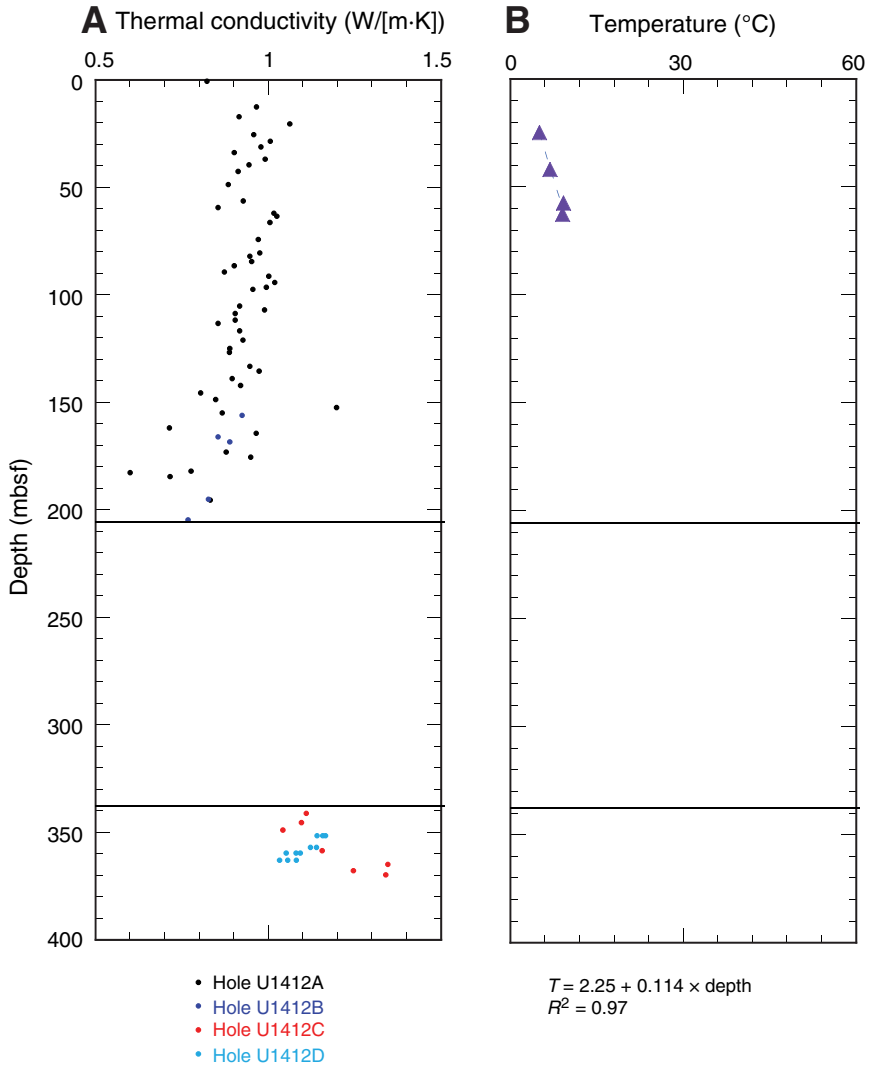

Figure F29. Strength data, Site U1412. **A.** Compressive strength measured using pocket (solid symbols) and needle (open symbols) penetrometers. **B.** Shear strength measured using an automated vane shear. Horizontal lines = lithostratigraphic unit boundaries.

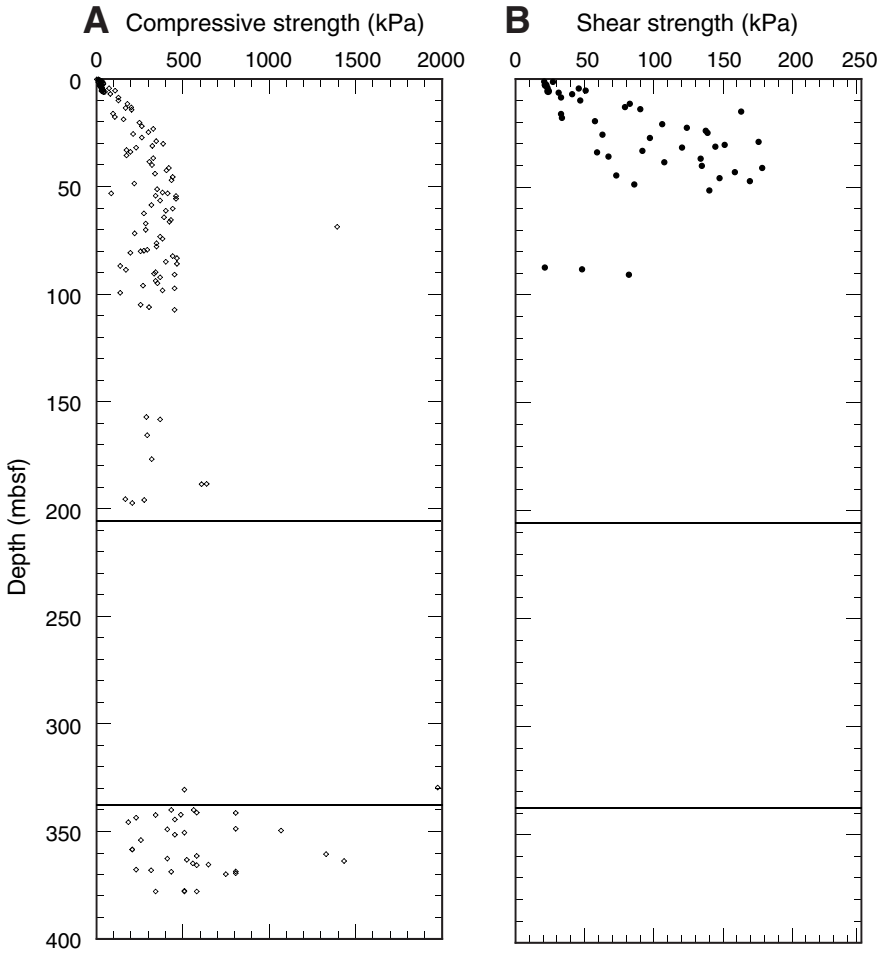

Figure F30. Formation factor calculated from electrical conductivity measurements, Site U1412.

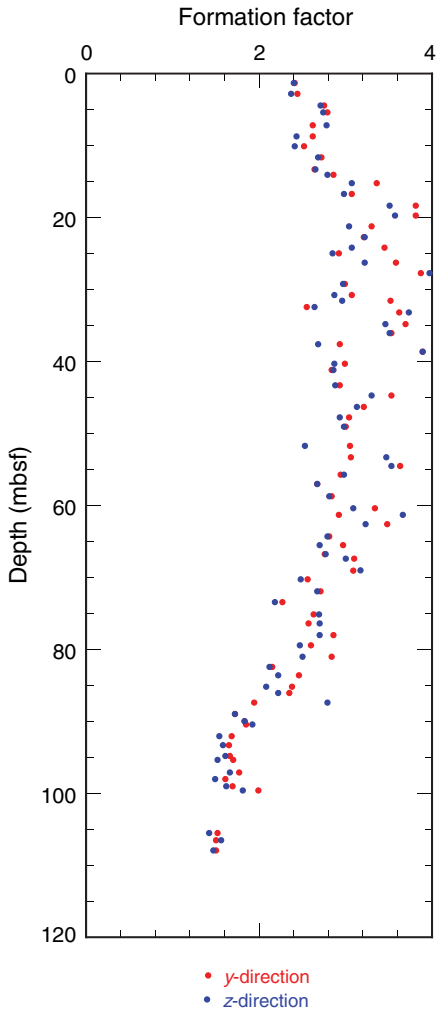

Figure F31. Reflectance L*, a*, and b* profiles, Site U1412. Horizontal lines = lithostratigraphic unit boundaries.

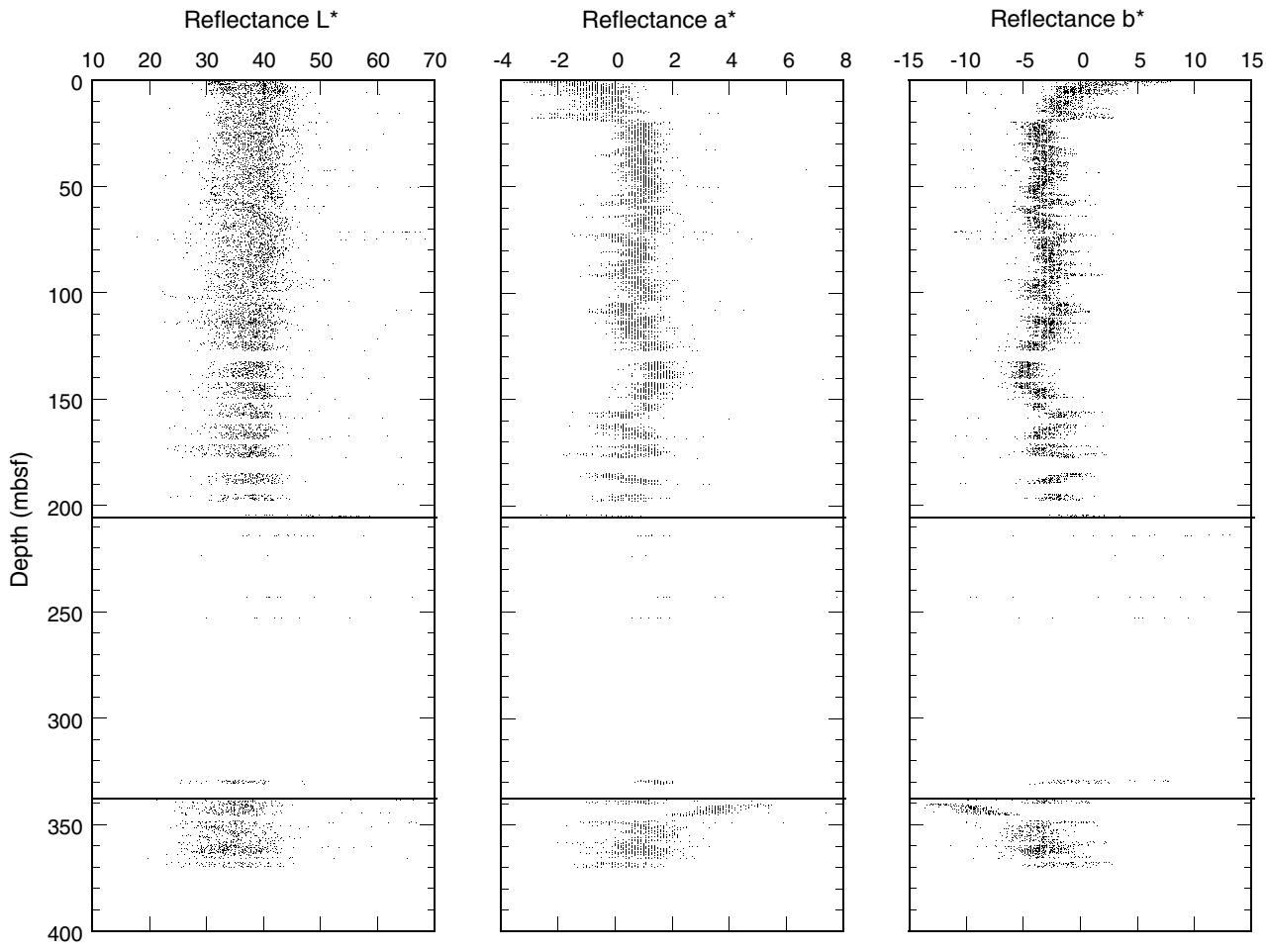

Figure F32. Paleomagnetic measurements on sediment archive-half core sections (circles) and discrete samples (crosses), Hole U1412A. **A, B.** NRM intensity and inclination after 0 and 40 mT AF demagnetization. **C.** Characteristic remanent magnetization (ChRM) for discrete samples determined from principal component analysis.

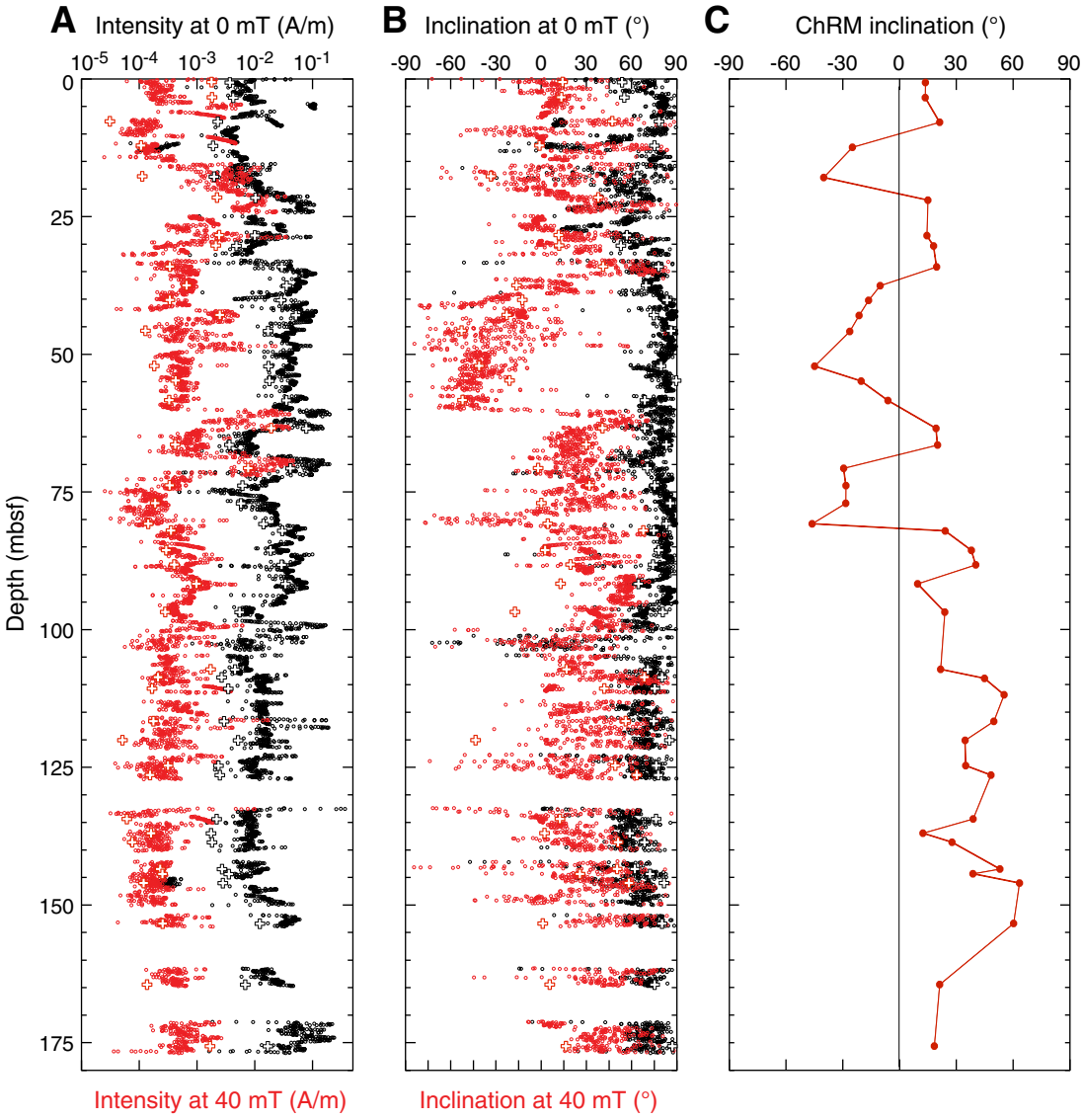

Figure F33. Paleomagnetic measurements on archive sections (open circles) and discrete samples (solid circles), Hole U1412B. **A, B.** NRM intensity and inclination after 0 and 40 mT AF demagnetization. **C.** Characteristic remanent magnetization (ChRM) for discrete samples determined from principal component analysis.

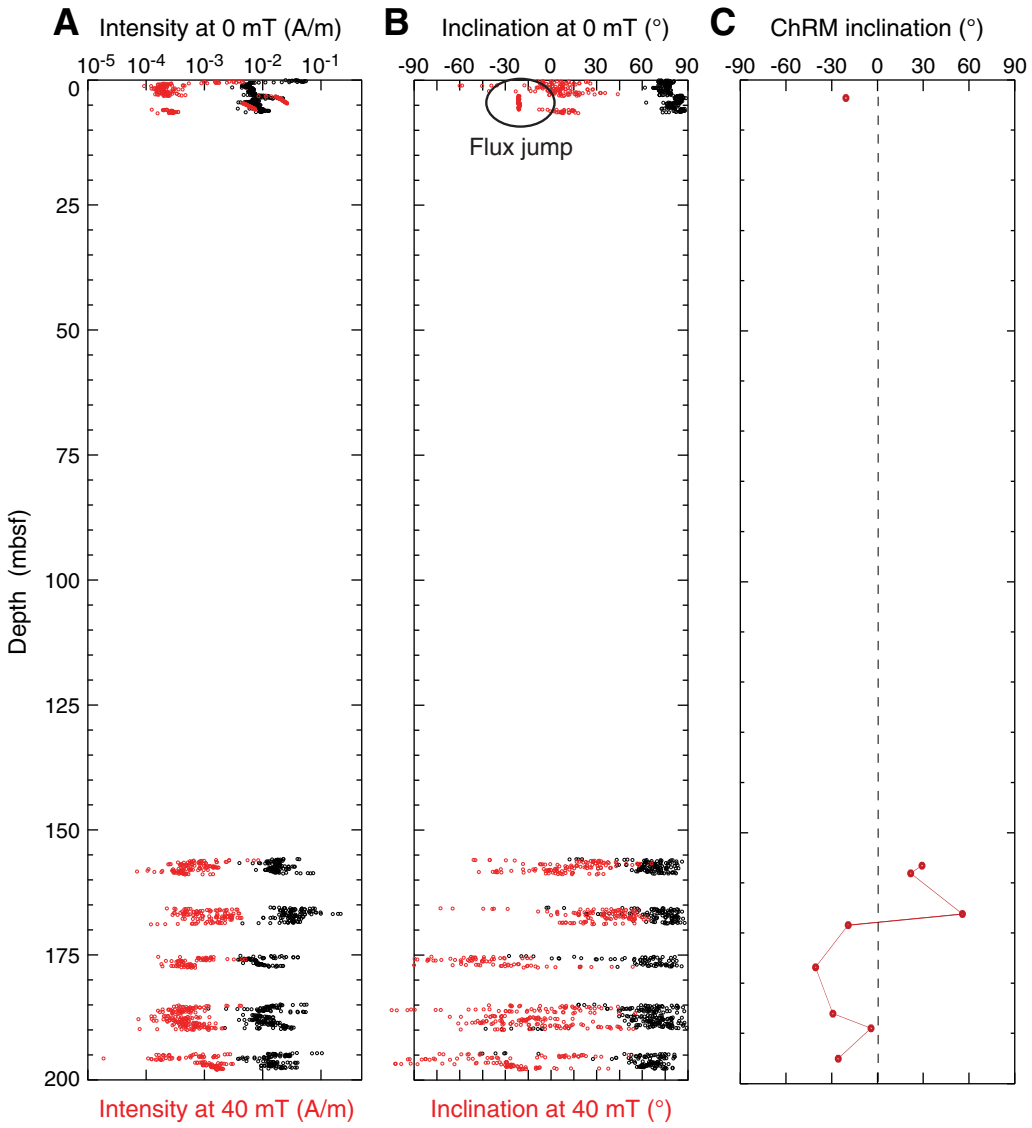

Figure F34. Paleomagnetic measurements on archive sections (open circles) and discrete samples (solid circles), Hole U1412C. **A, B.** NRM intensity and inclination after 0 and 40 mT AF demagnetization. **C.** Characteristic remanent magnetization (ChRM) for discrete samples determined from principal component analysis.

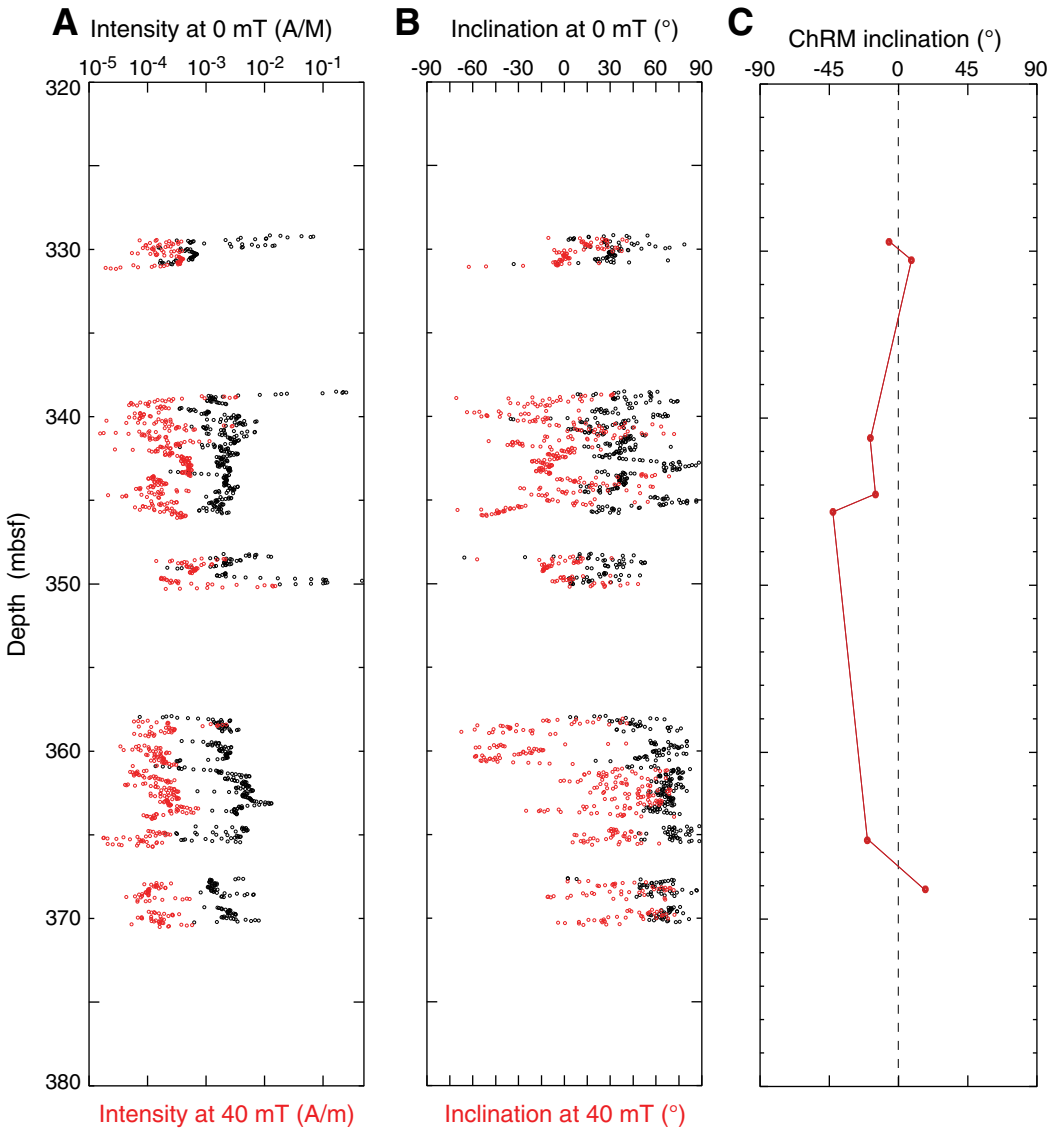

Figure F35. Paleomagnetic measurements on archive sections (open circles) and discrete samples (solid circles), Hole U1412D. **A, B.** NRM intensity and inclination after 0 and 40 mT AF demagnetization. **C.** Characteristic remanent magnetization (ChRM) for discrete samples determined from principal component analysis.

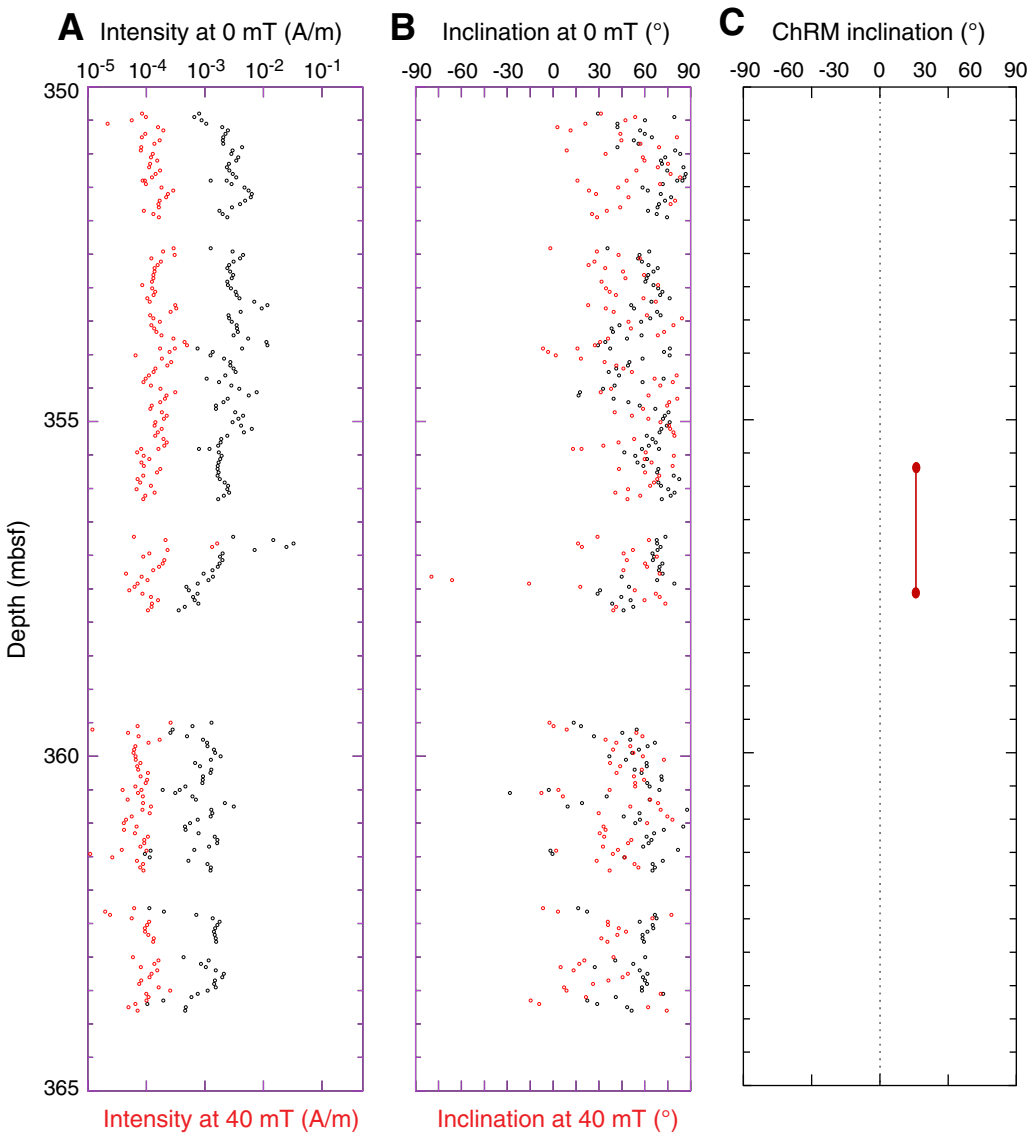

Figure F36. Representative vector end-point diagrams (Zijderveld, 1967) for sediment samples through stepwise AF demagnetization. All samples display a normal vertical component of magnetization caused by drilling that is removed after 5 mT demagnetization. **A.** Pass-through section measurement (Sample 344-U1412A-10H-2A, 17.5 cm). **B.** Corresponding discrete sample (Sample 344-U1412A-10H-2W, 17.5-19.5 cm). **C.** Normal polarity sample (Sample 344-U1412A-12H-2W, 55-57 cm). **D.** Reversed polarity sample (Sample 344-U1412A-6H-1W, 92-94 cm). Open and solid squares = projection of the magnetization vector end-points onto the vertical and horizontal planes, respectively. NRM = natural remanent magnetization.

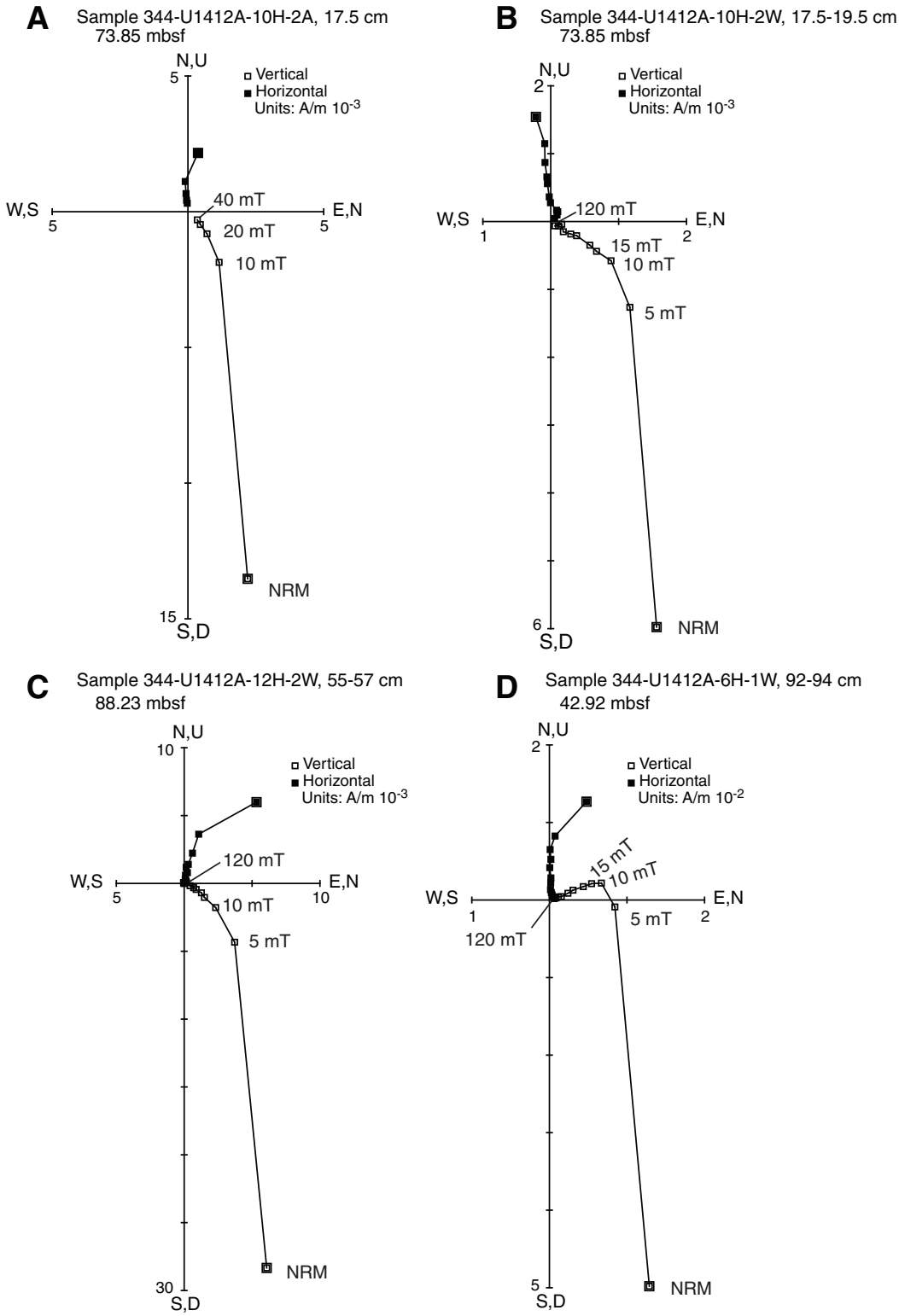

Figure F37. Correlation of Hole U1412A discrete sample magnetostratigraphy with the geomagnetic polarity timescale of Gradstein et al. (2012). Discrete sample results of characteristic remanence (ChRM) were determined by principal component analysis (Kirschvink, 1980). Black = normal polarity, white = reversed polarity.

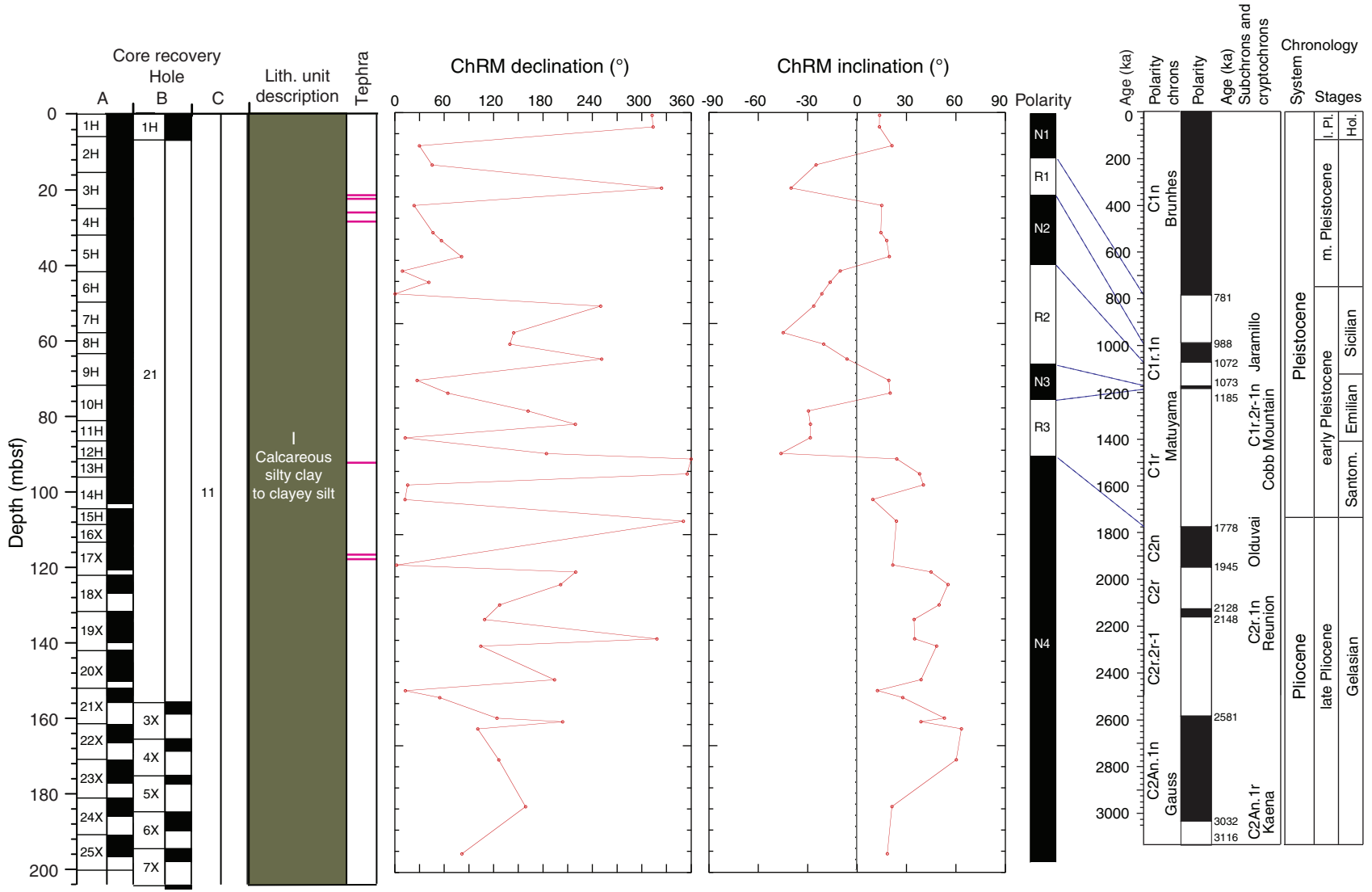

Table T1. Site U1412 coring summary. (Continued on next page.)

Hole U1412A
Latitude: 8°29.3294′N
Longitude: 84°7.6686′W
Time on hole (h): 60.2 (2.51 days)
Seafloor (drill pipe measurement from rig floor, m DRF): 1931.6
Distance between rig floor and sea level (m): 10.9
Water depth (drill pipe measurement from sea level, m): 1920.7
Total penetration (drilling depth below seafloor, m DSF): 200.3
Total length of cored section (m): 200.3
Total core recovered (m): 170.03
Core recovery (%): 85
Total number of cores: 25

Hole U1412B
Latitude: 8°29.1599′N
Longitude: 84°7.7512′W
Time on hole (h): 104.4 (4.35 days)
Seafloor (drill pipe measurement from rig floor, m DRF): 1975.9
Distance between rig floor and sea level (m): 11.0
Water depth (drill pipe measurement from sea level, m): 1964.9
Total penetration (drilling depth below seafloor, m DSF): 304.3
Total length of cored section (m): 155.2
Total core recovered (m): 28.3
Core recovery (%): 18
Total number of cores: 19

Hole U1412C
Latitude: 8°29.1700′N
Longitude: 84°7.7467′W
Time on hole (h): 71.3 (2.97 days)
Seafloor (drill pipe measurement from rig floor, m DRF): 1975.9
Distance between rig floor and sea level (m): 10.95
Water depth (drill pipe measurement from sea level, m): 1965.0
Total penetration (drilling depth below seafloor, m DSF): 387.0
Total length of cored section (m): 87.0
Total core recovered (m): 36.6
Core recovery (%): 42
Total number of cores: 9

Hole U1412D
Latitude: 8°29.1402′N
Longitude: 84°7.7793′W
Time on hole (h): 71.3 (2.97 days)
Seafloor (drill pipe measurement from rig floor, m DRF): 1984.0
Distance between rig floor and sea level (m): 11.5
Water depth (drill pipe measurement from sea level, m): 1973.0
Total penetration (drilling depth below seafloor, m DSF): 369.2
Total length of cored section (m): 18.8
Total core recovered (m): 12.3
Core recovery (%): 65
Total number of cores: 2

Core	Date (2012)	Time UTC (h)	Depth DSF (m) Top of cored interval	Depth DSF (m) Bottom of cored interval	Interval advanced (m)	Depth CSF (m) Top of cored interval	Depth CSF (m) Bottom of cored interval	Length of core recovered (m)	Recovery (%)	Comments
344-U1412A-										
1H	14 Nov	2135	0.00	5.90	5.9	0.00	5.90	5.90	100	FlexIt
2H	14 Nov	2235	5.90	15.40	9.5	5.90	15.76	9.86	104	FlexIt
3H	14 Nov	2355	15.40	24.90	9.5	15.40	25.54	10.14	107	FlexIt, APCT-3
4H	15 Nov	0110	24.90	32.90	8.0	24.90	32.91	8.01	100	FlexIt
5H	15 Nov	0220	32.90	42.00	9.1	32.90	42.04	9.14	100	FlexIt, APCT-3
6H	15 Nov	0330	42.00	49.50	7.5	42.00	49.56	7.56	101	FlexIt
7H	15 Nov	0450	49.50	57.50	8.0	49.50	57.58	8.08	101	FlexIt, APCT-3
8H	15 Nov	0620	57.50	62.90	5.4	57.50	62.85	5.35	99	FlexIt, APCT-3
9H	15 Nov	0730	62.90	72.20	9.3	62.90	72.20	9.34	100	FlexIt
10H	15 Nov	0840	72.20	81.10	8.9	72.20	81.10	8.90	100	FlexIt
11H	15 Nov	0945	81.10	86.30	5.2	81.10	86.32	5.22	100	FlexIt
12H	15 Nov	1100	86.30	90.80	4.5	86.30	90.84	4.54	101	FlexIt
13H	15 Nov	1230	90.80	95.90	5.1	90.80	95.88	5.08	100	FlexIt
14H	15 Nov	1330	95.90	104.60	8.7	95.90	103.90	8.00	92	FlexIt
15H	15 Nov	1445	104.60	108.20	3.6	104.60	108.23	3.63	101	FlexIt

Table T1 (continued).

Core	Date (2012)	Time UTC (h)	Depth DSF (m) Top of cored interval	Depth DSF (m) Bottom of cored interval	Interval advanced (m)	Depth CSF (m) Top of cored interval	Depth CSF (m) Bottom of cored interval	Length of core recovered (m)	Recovery (%)	Comments
16X	15 Nov	1630	108.20	113.00	4.8	108.20	115.16	6.96	145	
17X	15 Nov	1740	113.00	122.70	9.7	113.00	121.81	8.81	91	
18X	15 Nov	1910	122.70	132.40	9.7	122.70	127.34	4.64	48	
19X	15 Nov	2010	132.40	142.10	9.7	132.40	140.47	8.07	83	
20X	15 Nov	2125	142.10	151.80	9.7	142.10	150.20	8.10	84	
21X	15 Nov	2305	151.80	161.50	9.7	151.80	155.46	3.66	38	
22X	16 Nov	0145	161.50	171.20	9.7	161.50	165.38	3.88	40	
23X	16 Nov	0445	171.20	180.90	9.7	171.20	177.11	5.91	61	
24X	16 Nov	0840	180.90	190.60	9.7	180.90	185.86	4.96	51	
25X	16 Nov	1425	190.60	200.30	9.7	190.60	196.89	6.29	65	
			Hole U1412A totals:		200.3			170.03	85	
344-U1412B-										
1H	17 Nov	0915	0.00	6.70	6.7	0.00	6.74	6.74	101	
21					*****Drilled from 6.7 to 155.8 m DSF*****					
3X	18 Nov	0250	155.80	165.50	9.7	155.80	159.03	3.23	33	
4X	18 Nov	0615	165.50	175.20	9.7	165.50	168.89	3.39	35	
5X	18 Nov	0935	175.20	184.90	9.7	175.20	177.61	2.41	25	
6X	18 Nov	1200	184.90	194.60	9.7	184.90	189.95	5.05	52	
7X	18 Nov	1400	194.60	204.30	9.7	194.60	198.05	3.45	36	
8X	18 Nov	1650	204.30	214.00	9.7	204.30	205.40	1.10	11	
9X	18 Nov	1910	214.00	223.70	9.7	214.00	214.38	0.38	4	
10X	18 Nov	2110	223.70	228.50	4.8	223.70	223.83	0.13	3	
11X	18 Nov	2225	228.50	233.40	4.9	228.50	229.21	0.71	14	
12X	19 Nov	0235	233.40	243.10	9.7	233.40	233.83	0.43	4	
13X	19 Nov	0700	243.10	252.80	9.7	243.10	243.36	0.26	3	
14X	19 Nov	0930	252.80	262.50	9.7	252.80	252.99	0.19	2	
15X	19 Nov	1105	262.50	272.20	9.7	262.50	262.53	0.03	0	
16X	19 Nov	1435	272.20	281.90	9.7	272.20	272.30	0.10	1	
17X	19 Nov	1635	281.90	291.60	9.7	281.90	282.02	0.12	1	
18X	19 Nov	1930	291.60	295.60	4.0	291.60	291.89	0.29	7	
19X	19 Nov	2145	295.60	301.30	5.7	295.60	295.81	0.21	4	
20X	19 Nov	2345	301.30	304.30	3.0	301.30	301.34	0.04	1	
			Hole U1412B totals:		304.3			28.26	18	
344-U1412C-										
11					*****Drilled from 0.0 to 300.0 m DSF*****					
2R	22 Nov	1430	300.00	309.50	9.5	300.00	301.22	1.22	13	
3R	22 Nov	1735	309.50	319.10	9.6	309.50	315.28	5.78	60	
4R	22 Nov	2050	319.10	328.80	9.7	319.10	321.50	2.40	25	
5R	23 Nov	2355	328.80	338.50	9.7	328.80	331.14	2.34	24	
6R	23 Nov	0220	338.50	348.20	9.7	338.50	345.90	7.40	76	
7R	23 Nov	0425	348.20	357.90	9.7	348.20	350.92	2.72	28	
8R	23 Nov	0715	357.90	367.60	9.7	357.90	366.07	8.17	84	
9R	23 Nov	1010	367.60	377.30	9.7	367.60	370.31	2.71	28	
10R	23 Nov	1350	377.30	387.00	9.7	377.30	381.13	3.83	39	
			Hole U1412C totals:		387.0			36.57	42	
344-U1412D-										
11					*****Drilled from 0.0 to 350.4 m DSF*****					
2R	2 Dec	1350	350.40	359.50	9.1	350.40	358.17	7.77	85	
3R	2 Dec	1530	359.50	369.20	9.7	359.50	363.98	4.48	46	
			Hole U1412D totals:		369.2			12.25	65	
			Site U1412 totals:		1260.80			247.10		

DSF = drilling depth below seafloor, CSF = core depth below seafloor. H = advanced piston corer core, X = extended core barrel core, R = rotary core barrel core, numeric core type = drilled interval. APCT-3 = advanced piston corer temperature tool.

Table T2. Summary of Site U1412 lithologic units.

Unit	Top depth (mbsf)	Hole, core, section, interval (cm)	Bottom depth (mbsf)	Hole, core, section, interval (cm)	Unit thickness (m)	Major lithology
		344-		344-		
I	0	U1412A-2H-1, 0	204.74	U1412B-8X-1, 44	204.74	Calcareous silty clay to clayey silt
II	204.74	U1412B-8X-1, 44	331.01	U1412C-5R-CC, 10	126.27	Calcareous ooze with nannofossils and biogenic silica
III	331.01	U1412C-5R-CC, 10	387.00	U1412C-10R-CC, 19	55.99	Clayey siltstone to claystone
	350.40	U1412D-2R-1, 0	363.98	U1412D-3R-CC, 15	13.58	

Table T3. Calcareous nannofossil faunal distribution, Holes U1412A–U1412C. (Continued on next page.)

Core, section, interval (cm)	Depth (mbsf) Top	Depth (mbsf) Bottom	Preservation	Group abundance	*Calcidiscus leptoporus*	*Ceratolithus cristatus*	*Ceratolithus cristatus (rugosus)*	*Ceratolithus cristatus* var. *telesmus*	*Coccolithus miopelagicus*	*Coccolithus pelagicus*	*Coronocyclus nitescens* (elliptical)	*Cyclicargolithus floridanus*	*Discoaster brouweri*	*Discoaster deflandrei*	*Discoaster* sp.	*Discoaster* spp.	*Emiliania huxleyi*	*Gephyrocapsa* (<4 µm)	*Gephyrocapsa* (>4 µm)	*Gephyrocapsa caribbeanica*	*Gephyrocapsa ericsonii*	*Gephyrocapsa oceanica*	*Helicosphaera carteri*	*Helicosphaera neogranulata*	*Helicosphaera sellii*	*Helicosphaera* sp.	*Helicosphaera* spp.	*Pontosphaera discopora*	*Pontosphaera multipora*	*Pseudoemiliania lacunosa*	*Reticulofenestra pseudoumbilicus*	*Rhabdosphaera clavigera*	*Scyphosphaera cylindrica*	*Sphenolithus abies*	*Sphenolithus heteromorphus*	*Sphenolithus moriformis*	*Sphenolithus* spp.	*Syracosphaera histrica*	*Syracosphaera pulchra*	*Umbilicosphaera sibogae*
344-U1412A-																																								
1H-CC, 0–5	5.85	5.90	G	A	C												R	A	A		C	A	C			C												R	
2H-CC, 0–5	15.70	15.75	G	A	C												R	C	C			C	C			C							R						
3H-CC, 0–5	25.48	25.53	M	C	Freq					R								C	C			C				C											*		
4H-CC, 0–5	32.86	32.91	G	C	Freq													C				C				C		R								*		
5H-CC, 0–5	41.99	42.04	M	C	Freq											*		C				C		C		C												
6H-CC, 0–5	49.51	49.56	M	F	R											*		C		C		C		Freq		C										*	R	
7H-CC, 0–5	57.53	57.58	G	C	Freq										*					C		C	R	Freq		C												
8H-CC, 0–5	62.80	62.85	P	R	R															Freq		Freq				R												
9H-CC, 0–5	72.14	72.19	M	C	R													C		C		C		Freq		C												R
10H-CC, 0–3	81.07	81.10	M	C	R	*	*			R	*				*			A		A		A				C				R					*		R	R
11H-CC, 0–5	86.26	86.31	M	C	Freq																	C	Freq			C											R	
12H-CC, 0–5	90.78	90.83	M	C	Freq													C				C				C										*		
13H-CC, 0–5	95.82	95.87	M	C	R					R								C	Freq	Freq			C	Freq			C							R			*	R	
14H-CC, 0–5	103.84	103.89	G	C	Freq					Freq						*		C	Freq	C			C				C										*	R	
15H-CC, 0–5	108.18	108.23	M	C	R					R					*			C		Freq			C				C												
16X-CC, 0–5	115.11	115.16	M	C	Freq					R								C	C								C												
17X-CC, 0–5	121.76	121.81	M	C	Freq					R								C	Freq	C				Freq			C	R											
18X-CC, 0–5	127.29	127.34	P	F	R				R	R								C	C	C			C				C	R											
19X-CC, 0–5	140.42	140.47	M	C	Freq					R								C	Freq	C				C			C												
20X-CC, 0–5	150.15	150.20	M	C	Freq										*			C	R	C			C	R			Freq			R								
21X-CC, 0–5	155.41	155.46	M	C	Freq					R								C	Freq	C			C	Freq			C												
22X-CC, 0–5	165.33	165.38	M	C	Freq					R								C	C	C			Freq	Freq		R	C										R		
23X-CC, 0–5	177.05	177.10	M	C	Freq					R								C	C	C			C	Freq			C			Freq									
24X-CC, 0–5	185.81	185.86	M	C	R					Freq								C					Freq	Freq															
25X-CC, 0–5	196.81	196.86	P	F	Freq					Freq						*		C					Freq			Freq	C												
344-U1412B-																																								
1H-CC, 0–5	6.67	6.72	G	C	R				R	R							Freq	C	C			C		Freq			C			*									
3X-CC, 0–5	158.98	159.03	M	F	R					Freq								C		Freq		C	R				C												R
4X-CC, 0–5	168.83	168.88	M	R	R					R								Freq		R		Freq	R				Freq												R
5X-CC, 0–5	177.55	177.60	G	C	Freq					R								C		C		C	Freq	R			C			R							*		
6X-CC, 0–5	189.88	189.93	M	R	R					R							R	Freq		R		R								R									
7X-CC, 0–5	197.98	198.03	M	F	Freq												Freq	C				C		R			Freq												Freq
8X-CC, 0–1	205.39	205.40	M	C						Freq						Freq															Freq				R				
9X-CC, 0–5	214.33	214.38	P	F						C						Freq															C				C		C		
10X-CC, 0–4	223.79	223.83	M	C						C						C													R		C					R	C		
11X-CC, 0–5	229.16	229.21	M	C						C	R					Freq											Freq				Freq				C	C	C		
12X-CC, 0–5	233.78	233.83	M	C						C						Freq															C				C	Freq	C		
13X-CC, 0–5	243.26	243.31	P	C						C						R																			C	C	C		
14X-CC, 0–5	252.80	252.85	M	C						C						Freq											Freq				Freq				C	C	C		
16X-CC, 0–5	272.20	272.25	P	C						C		Freq				Freq															Freq				C	C	A		

Table T3 (continued).

Core, section, interval (cm)	Depth (mbsf) Top	Depth (mbsf) Bottom	Preservation	Group abundance	*Calcidiscus leptoporus*	*Ceratolithus cristatus*	*Ceratolithus cristatus (rugosus)*	*Ceratolithus cristatus* var. *telesmus*	*Coccolithus miopelagicus*	*Coccolithus pelagicus*	*Coronocyclus nitescens* (elliptical)	*Cyclicargolithus floridanus*	*Discoaster brouweri*	*Discoaster deflandrei*	*Discoaster* sp.	*Discoaster* spp.	*Emiliania huxleyi*	*Gephyrocapsa* (<4 µm)	*Gephyrocapsa* (>4 µm)	*Gephyrocapsa caribbeanica*	*Gephyrocapsa ericsonii*	*Gephyrocapsa oceanica*	*Helicosphaera carteri*	*Helicosphaera neogranulata*	*Helicosphaera sellii*	*Helicosphaera* sp.	*Helicosphaera* spp.	*Pontosphaera discopora*	*Pontosphaera multipora*	*Pseudoemiliania lacunosa*	*Reticulofenestra pseudoumbilicus*	*Rhabdosphaera clavigera*	*Scyphosphaera cylindrica*	*Sphenolithus abies*	*Sphenolithus heteromorphus*	*Sphenolithus moriformis*	*Sphenolithus* spp.	*Syracosphaera histrica*	*Syracosphaera pulchra*	*Umbilicosphaera sibogae*
17X-CC, 0–5	281.90	281.95	P	C	R				Freq	C																					Freq				C	C	C			
18X-CC, 0–5	291.75	291.80	M	C					Freq	C		C				C															C				C	C	C			
19X-CC, 0–5	295.76	295.81	M	C						C		Freq				C											R				C				C	C	C			
20X-CC, 0–4	301.30	301.34		B																																				
344-U1412C-																																								
2R-CC, 0–5	301.14	301.19	M	C	Freq					C		C				Freq										R					C				C	C				
3R-CC, 0–5	315.23	315.28	P	C						C		Freq			C																C				C	C				
4R-CC, 0–5	321.40	321.45	P	F	Freq										*			C				C				R														
5R-CC, 0–5	331.03	331.08	P	C					Freq	C		C		R		C															C				C	C				
6R-CC, 0–4	345.86	345.90	M	F	Freq															Freq		Freq				Freq														
7R-CC, 0–5	350.87	350.92	P	R	C										*			C		C		C				Freq														
8R-CC, 0–5	365.98	366.03	G	F	C					R			R										R			C				A	C		R				R			R
9R-CC, 0–5	370.22	370.27	M	F	C								R		R			Freq				Freq		Freq		C		R		R	Freq									

* = reworked. Preservation: G = good, M = moderate, P = poor. Abundance: A = abundant, C = common, Freq = frequent, F = few, R = rare. See the "Methods" chapter (Harris et al., 2013) for group species and abundance definitions.

Table T4. Radiolarian faunal distribution, Holes U1412A–U1412C. (This table is available in an **oversized format.**)

Table T5. Benthic foraminiferal faunal counts, Holes U1412A–U1412C. (This table is available in an **oversized format.**)

Table T6. Uncorrected pore fluid major element concentrations, Site U1412.

Core, section, interval (cm)	Depth (mbsf)	Volume (mL)	Salinity	pH	Alkalinity (mM)	SO_4 IC (mM)	SO_4 ICP (mM)	Cl IC (mM)	Cl titr. (mM)	Br (mM)	Na (mM)	K (mM)	Ca (mM)	Mg (mM)	NH_4 (mM)
344-U1412A-															
1H-1, 138–150	1.44	52.0	35	8.07	4.31	27.45	26.94	559	553	0.86	461	12.0	9.13	47.8	0.31
1H-2, 138–150	2.94	52.0	35	7.67	5.78	24.46	24.38	551	554	0.86	454	11.6	8.41	46.8	0.54
1H-4, 98–110	5.54	53.0	34.5	7.82	10.03	19.08	18.73	559	557	0.88	465	11.7	7.27	46.3	1.05
2H-2, 138–150	8.84	46.0	34.5	7.97	16.15	11.35	16.56	559	559	0.90	456	11.7	5.34	43.0	1.56
2H-6, 72–84	14.20	46.0	34	7.96	26.09	0.20	1.01	562	560	0.93	453	11.3	3.19	40.2	2.44
2H-7, 106–118	15.38	56.0	34	7.97	25.13	0.05	0.38	559	562	0.92	456	11.4	3.28	40.4	—
3H-1, 138–150	16.84	45.0	34	8.04	26.72	0.46	2.03	564	563	0.94	446	11.0	3.88	40.7	3.05
3H-3, 138–150	19.84	25.0	33.5	7.96	28.99	0.20	0.57	561	560	0.95	460	11.2	3.80	41.5	3.28
3H-5, 138–150	22.84	50.0	33.5	7.78	28.09	0.10	0.37	565	562	0.97	461	11.9	3.89	40.4	4.14
4H-2, 138–150	27.84	23.0	33.5	7.9	31.99	0.10	0.32	563	561	1.01	459	11.8	4.23	40.8	5.74
4H-4, 138–150	30.87	41.0	33.5	7.76	34.73	0.05	0.01	561	560	1.04	467	11.9	4.41	42.2	5.48
5H-3, 118–135	36.19	46.0	34.5	7.75	38.61	0.41	0.45	563	561	1.08	473	12.2	4.90	43.2	6.58
5H-7, 133–150	40.50	51.0	34.5	7.68	40.25	0.05	0.35	564	565	1.12	459	12.2	4.83	42.2	7.15
6H-2, 132–149	44.87	45.0	34	7.85	42.6	0.10	0.24	563	561	1.13	465	12.5	5.01	43.4	7.66
6H-4, 134–151	47.91	47.0	34.5	7.88	40.46	0.05	0.38	566	562	1.16	468	13.1	4.64	42.1	8.14
7H-2, 128–145	51.89	50.0	34.5	7.72	43.48	0.41	0.45	564	562	1.17	470	12.4	5.16	44.3	8.09
7H-5, 103–120	55.89	52.0	34.5	7	43.99	0.05	0.16	565	562	1.19	472	12.4	5.08	44.8	8.19
8H-1, 129–151	58.90	53.0	34.5	7.8	41.83	0.87	1.09	562	562	1.18	471	12.3	5.01	44.1	8.37
8H-3, 100–122	61.62	44.0	34	7.66	43.37	0.00	0.31	556	554	1.20	462	12.4	4.91	43.5	8.35
9H-2, 128–150	65.76	34.0	34.5	7.77	43.65	0.05	0.27	566	562	1.24	459	12.1	4.83	43.6	8.62
9H-6, 135–157	70.54	52.0	33.5	7.94	40.98	0.05	0.35	548	544	1.22	456	12.4	4.44	41.7	8.57
10H-1, 128–150	73.59	56.0	34.5	7.81	41.62	0.26	0.36	565	565	1.27	470	12.2	4.60	43.9	8.73
10H-5, 134–156	79.59	51.0	34.5	7.86	40.52	0.00	0.31	566	564	1.28	479	12.7	4.90	44.1	9.19
11H-2, 130–152	83.93	43.0	33	7.86	40.59	0.10	0.26	546	540	1.26	458	11.8	5.11	41.9	8.88
12H-1, 115–137	87.56	40.0	34.5	7.79	41.14	0.56	0.79	563	562	1.30	465	11.1	5.45	43.8	8.87
12H-3, 94–116	90.13	57.0	34.5	7.84	40.04	0.31	0.51	567	565	1.31	462	11.7	5.15	42.7	9.16
13H-2, 124–146	93.62	51.0	34	7.7	35.8	0.20	0.45	566	568	1.32	472	11.6	4.59	42.5	8.83
14H-2, 80–102	98.22	52.0	34.5	7.78	34.34	0.15	0.16	567	567	1.33	455	11.2	4.83	40.3	9.12
15H-2, 93–115	106.75	51.0	33.5	7.76	32.31	0.10	0.33	571	563	1.36	482	12.5	5.25	40.6	9.30
16X-2, 126–148	110.98	12.0	33.5	—	—	0.20	0.41	563	561	1.35	468	11.6	5.51	40.2	9.26
20X-4, 131–151	148.01	0.8	—	—	—	0.05	—	559	555	1.38	362	7.65	5.25	31.6	—
22X-1, 131–151	162.91	2.3	—	—	—	2.40	—	563	564	1.32	376	9.04	5.62	32.4	—
22X-3, 68–88	165.01	1.8	—	—	—	0.82	—	569	563	1.39	442	10.8	6.08	35.0	—
23X-3, 100–120	175.30	2.0	—	—	—	1.48	—	563	561	1.36	577	13.2	8.93	45.0	—
344-U1412B-															
4X-2, 100–120	167.97	5.2	32.0	—	—	—	—	548	553	1.08	328	7.02	6.31	31.1	—
5X-1, 120–140	176.40	32.0	33.0	7.77	18.9	0.46	—	554	560	1.10	442	9.52	8.35	38.9	6.24
6X-2, 99–125	186.74	30.0	33.0	7.79	18.19	0.61	—	554	556	1.12	414	8.07	8.01	33.9	5.75
7X-2, 51–73	196.02	50.0	32.5	7.76	16.09	0.61	—	555	561	1.15	378	10.2	9.14	35.4	6.03
344-U1412C-															
4R-CC		3.5	31.5	—	—	2.96	—	555	—	1.29	480	9.07	9.48	31.2	—
5R-1, 0–36	328.80	11.0	31.0	—	—	0.31	—	560	560	1.53	468	8.44	10.3	26.8	3.38
6R-1, 9–20	338.59	7.0	30.5	—	—	0.15	—	550	553	1.90	498	8.22	12.4	28.2	3.49
7R-2, 96–112	350.31	20.0	32.0	7.84	6.42	0.51	—	558	560	2.20	475	9.12	12.4	24.0	3.91
8R-1, 121–148	359.11	8.0	30.5	—	—	0.51	—	541	546	2.23	440	7.79	11.2	23.6	4.04
8R-5, 59–95	364.13	35.0	31.0	7.93	3.86	0.36	—	552	559	2.42	492	9.58	10.8	22.2	5.31
9R-2, 58–88	369.02	35.0	31.0	7.74	4.41	0.26	—	544	553	2.47	486	9.98	11.2	22.4	6.10
344-U1412D-															
2R-2, 78–101	352.18	28.0	32	7.63	7.31	0.20	—	561	552	2.56	484	9.85	9.67	21.8	5.35
2R-5, 106–131	356.47	29.0	31.5	7.85	6.53	0.15	—	562	552	2.60	490	10.4	9.06	19.9	6.57
3R-3, 61–86	362.02	33.0	31.5	7.62	8.02	0.51	—	555	599	2.52	488	10.6	8.74	18.8	7.55
Drilling fluid						25.64		496	492	0.76	404	8.65	8.97	46.1	0.00

IC = ion chromatograph, ICP = inductively coupled plasma–atomic emission spectroscopy, titr. = titration, — = not measured.

Table T7. Uncorrected pore fluid minor element concentrations, Site U1412.

Core, section, interval (cm)	Depth (mbsf)	B (μM)	Li (μM)	Sr (μM)	Ba (μM)	Mn (μM)	Si (μM)	PO_4 (μM)
344-U1412A-								
1H-1, 138–150	1.44	576	25.8	82.9	0.344	1.3	501	9.3
1H-2, 138–150	2.94	497	22.1	79.8	0.250	0.0	514	19.6
1H-4, 98–110	5.54	536	22.7	79.3	0.241	0.0	581	28.6
2H-2, 138–150	8.84	474	20.0	68.2	0.664	0.0	627	47.1
2H-6, 72–84	14.20	508	12.7	71.2	10.8	0.0	655	88.9
2H-7, 106–118	15.38	571	10.7	75.6	12.5	0.0	622	102
3H-1, 138–150	16.84	537	9.14	75.2	12.9	0.0	625	102
3H-3, 138–150	19.84	502	5.96	80.1	15.7	0.36	530	117
3H-5, 138–150	22.84	531	5.91	79.9	16.9	0.37	537	121
4H-2, 138–150	27.84	453	9.31	79.0	21.1	0.46	504	99.4
4H-4, 138–150	30.87	383	10.9	81.7	25.8	1.2	545	102
5H-3, 118–135	36.19	389	12.3	85.6	33.0	2.2	544	85.6
5H-7, 133–150	40.50	377	13.1	84.8	36.6	1.8	534	86.6
6H-2, 132–149	44.87	370	12.3	87.1	37.5	1.6	512	72.6
6H-4, 134–151	47.91	292	12.7	82.8	36.9	0.97	446	57.4
7H-2, 128–145	51.89	392	13.8	88.4	35.6	1.8	594	91.3
7H-5, 103–120	55.89	359	14.4	88.3	34.5	1.5	580	82.6
8H-1, 129–151	58.90	356	13.7	88.6	30.0	1.4	579	79.2
8H-3, 100–122	61.62	398	12.4	88.1	30.0	0.48	535	92.3
9H-2, 128–150	65.76	390	13.1	92.7	29.0	0.54	530	97.4
9H-6, 135–157	70.54	333	15.1	84.4	28.6	0.44	451	57.5
10H-1, 128–150	73.59	329	17.6	87.3	31.7	0.58	580	62.7
10H-5, 134–156	79.59	304	17.4	88.1	35.9	1.6	535	52.2
11H-2, 130–152	83.93	312	16.0	83.7	38.8	1.7	553	58.8
12H-1, 115–137	87.56	302	15.3	83.6	34.2	2.4	596	58.9
12H-3, 94–116	90.13	288	16.8	86.6	37.5	2.1	586	51.0
13H-2, 124–146	93.62	271	17.7	79.6	30.5	0.58	541	39.8
14H-2, 80–102	98.22	285	17.9	83.6	26.0	0.55	399	29.9
15H-2, 93–115	106.75	239	23.0	85.1	36.8	0.50	612	33.6
16X-2, 126–148	110.98	219	24.9	85.1	42.5	1.2	585	22.2
20X-4, 131–151	148.01	—	—	—	—	—	—	—
22X-1, 131–151	162.91	134	37.4	91.6	44.0	1.6	609	—
22X-3, 68–88	165.01	70.0	35.2	92.4	47.3	1.2	483	—
23X-3, 100–120	175.30	113	40.8	92.4	37.7	0.92	373	—
344-U1412B-								
4X-2, 100–120	167.97	109	53.1	92.6	58.1	2.3	589	—
5X-1, 120–140	176.40	112	58.3	107	68.5	1.5	518	—
6X-2, 99–125	186.74	132	61.4	121	79.4	3.0	625	—
7X-2, 51–73	196.02	128	60.8	139	113	3.0	639	—
344-U1412C-								
4R-CC	321.50	376	27.6	226	59.1	1.6	986	—
5R-1, 0–36	328.80	334	—	311	591	1.6	769	—
6R-1, 9–20	338.59	141	21.8	307	515	3.5	159	—
7R-2, 96–112	350.31	144	82.8	266	215	6.8	467	—
8R-1, 121–148	359.11	152	109	247	194	3.8	173	—
8R-5, 59–95	364.13	159	108	248	298	2.1	206	—
9R-2, 58–88	369.02	279	97.9	260	390	5.1	356	—
344-U1412D-								
2R-2, 78–101	352.18	215	91.9	227	264	2.2	313	—
2R-5, 106–131	356.47	261	71.9	235	366	1.8	392	—
3R-3, 61–86	362.02	492	69.0	239	317	2.8	745	—
Drilling fluid		322	18.0	76	0	0.0	66	0

— = not measured.

Table T8. Sulfate-corrected pore fluid major element concentrations, Site U1412.

Core, section, interval (cm)	Depth (mbsf)	Salinity	pH	Alkalinity (mM)	Cl IC (mM)	Cl titr. (mM)	Br (mM)	Na (mM)	K (mM)	Ca (mM)	Mg (mM)	NH_4 (mM)
344-U1412A-												
1H-1, 138–150	1.44	35.0	8.07	4.31	559	553	0.86	461	12.0	9.13	47.8	0.31
1H-2, 138–150	2.94	35.0	7.67	5.78	551	554	0.86	454	11.6	8.41	46.8	0.54
1H-4, 98–110	5.54	34.5	7.82	10.03	559	557	0.88	465	11.7	7.27	46.3	1.05
2H-2, 138–150	8.84	34.5	7.97	16.15	559	559	0.90	456	11.7	5.34	43.0	1.56
2H-6, 72–84	14.20	34.0	7.96	26.09	562	560	0.93	453	11.3	3.19	40.2	2.44
2H-7, 106–118	15.38	34.0	7.97	25.18	559	562	0.92	456	11.4	3.27	40.4	—
3H-1, 138–150	16.84	34.1	8.04	27.17	565	564	0.94	446	11.1	3.78	40.6	3.10
3H-3, 138–150	19.84	33.5	7.96	29.21	562	560	0.95	461	11.3	3.76	41.4	3.31
3H-5, 138–150	22.84	33.5	7.78	28.19	565	562	0.97	462	12.0	3.87	40.4	4.16
4H-2, 138–150	27.84	33.5	7.90	32.11	563	561	1.02	459	11.9	4.22	40.7	5.76
4H-4, 138–150	30.87	33.5	7.76	34.80	561	560	1.04	467	11.9	4.40	42.2	5.49
5H-3, 118–135	36.19	34.6	7.74	39.20	564	562	1.08	474	12.2	4.84	43.2	6.68
5H-7, 133–150	40.50	34.5	7.68	40.33	565	566	1.12	459	12.2	4.83	42.2	7.17
6H-2, 132–149	44.87	34.0	7.85	42.76	563	561	1.14	466	12.5	5.00	43.3	7.69
6H-4, 134–151	47.91	34.5	7.88	40.54	566	562	1.16	468	13.1	4.63	42.1	8.16
7H-2, 128–145	51.89	34.6	7.71	44.15	566	563	1.18	471	12.4	5.10	44.3	8.22
7H-5, 103–120	55.89	34.5	7.00	44.07	565	562	1.19	472	12.4	5.07	44.8	8.21
8H-1, 129–151	58.90	34.6	7.79	43.22	565	564	1.20	474	12.4	4.87	44.0	8.66
8H-3, 100–122	61.62	34.0	7.66	43.37	556	554	1.20	462	12.4	4.91	43.5	8.35
9H-2, 128–150	65.76	34.5	7.77	43.73	566	562	1.24	459	12.1	4.83	43.6	8.64
9H-6, 135–157	70.54	33.5	7.94	41.06	548	544	1.22	456	12.4	4.43	41.7	8.59
10H-1, 128–150	73.59	34.5	7.81	42.02	565	566	1.28	471	12.3	4.56	43.9	8.82
10H-5, 134–156	79.59	34.5	7.86	40.52	566	564	1.28	479	12.7	4.90	44.1	9.19
11H-2, 130–152	83.93	33.0	7.86	40.74	546	540	1.26	458	11.8	5.10	41.9	8.92
12H-1, 115–137	87.56	34.6	7.78	42.01	564	563	1.31	466	11.2	5.37	43.8	9.07
12H-3, 94–116	90.13	34.5	7.84	40.50	568	566	1.31	463	11.7	5.11	42.7	9.27
13H-2, 124–146	93.62	34.0	7.70	36.07	567	568	1.32	473	11.6	4.56	42.4	8.90
14H-2, 80–102	98.22	34.5	7.78	34.53	568	568	1.34	455	11.2	4.81	40.3	9.17
15H-2, 93–115	106.75	33.5	7.76	32.43	571	564	1.37	483	12.5	5.23	40.5	9.34
16X-2, 126–148	110.98	33.5	—	—	564	561	1.35	469	11.7	5.48	40.1	9.34
20X-4, 131–151	148.01	—	—	—	559	555	1.38	362	7.65	5.24	31.6	—
22X-1, 131–151	162.91	—	—	—	570	572	1.38	373	9.08	5.27	30.9	—
22X-3, 68–88	165.01	—	—	—	572	566	1.41	444	10.8	5.98	34.7	—
23X-3, 100–120	175.30	—	—	—	567	565	1.40	587	13.4	8.93	44.9	—
344-U1412B-												
4X-2, 100–120	167.97	32.0	—	—	549	554	1.09	—	6.99	6.27	30.8	—
5X-1, 120–140	176.40	33.1	7.76	19.31	556	562	1.11	442	9.54	8.33	38.7	6.39
6X-2, 99–125	186.74	33.1	7.78	18.58	555	557	1.13	415	8.05	7.98	33.6	5.89
7X-2, 51–73	196.02	32.5	7.75	16.38	556	563	1.15	378	10.3	9.14	35.1	6.15
344-U1412C-												
4R-CC	321.47	31.6	—	—	562	—	1.36	311	9.13	9.54	29.3	—
5R-1, 0–36	328.80	31.0	—	—	561	561	1.54	328	8.43	10.3	26.5	3.42
6R-1, 9–20	338.59	30.5	—	—	551	553	1.91	338	8.22	12.4	28.1	3.51
7R-2, 96–112	350.31	32.0	7.83	6.51	560	561	2.23	349	9.13	12.4	23.6	3.99
8R-1, 121–148	359.11	30.5	—	—	542	547	2.26	358	7.78	11.3	23.1	4.13
8R-5, 59–95	364.13	31.0	7.93	3.89	553	560	2.44	364	9.60	10.8	21.8	5.38
9R-2, 58–88	369.02	31.0	7.74	4.43	545	554	2.49	369	10.0	11.2	22.2	6.17
344-U1412D-												
2R-2, 78–101	352.18	—	—	—	—	—	—	485	9.86	9.67	21.6	—
2R-5, 106–131	356.47	—	—	—	—	—	—	490	10.4	9.06	19.8	—
3R-3, 61–86	362.02	—	—	—	—	—	—	489	10.6	8.73	18.2	—
Drilling fluid												

IC = ion chromatograph, titr. = titration, — = not measured.

Table T9. Minor element concentrations corrected for drill fluid contamination, Site U1412.

Core, section, interval (cm)	Depth (mbsf)	B (μM)	Li (μM)	Sr (μM)	Ba (μM)	Mn (μM)	Si (μM)
344-U1412A-							
1H-1, 138–150	1.4	576	25.8	82.9	0.34	1.3	501
1H-2, 138–150	2.9	497	22.1	79.8	0.25	0.0	514
1H-4, 98–110	5.5	536	22.7	79.3	0.24	0.0	581
2H-2, 138–150	8.8	474	20.0	68.2	0.66	0.0	627
2H-6, 72–84	14.2	508	12.7	71.2	10.8	0.0	655
2H-7, 106–118	15.4	572	10.7	75.6	12.6	0.0	623
3H-1, 138–150	16.8	541	9.0	75.2	13.1	0.0	635
3H-3, 138–150	19.8	503	5.9	80.2	15.9	0.36	533
3H-5, 138–150	22.8	532	5.9	79.9	17.0	0.37	538
4H-2, 138–150	27.8	454	9.3	79.0	21.2	0.46	506
4H-4, 138–150	30.9	383	10.8	81.7	25.9	1.2	546
5H-3, 118–135	36.2	390	12.2	85.7	33.5	2.3	552
5H-7, 133–150	40.5	377	13.1	84.8	36.7	1.8	535
6H-2, 132–149	44.9						
6H-4, 134–151	47.9	292	12.7	82.8	37.0	0.97	446
7H-2, 128–145	51.9	393	13.7	88.6	36.2	1.8	603
7H-5, 103–120	55.9	359	14.4	88.3	34.6	1.5	581
8H-1, 129–151	58.9	358	13.6	89.1	31.1	1.5	597
8H-3, 100–122	61.6	398	12.4	88.1	30.0	0.48	535
9H-2, 128–150	65.8	390	13.1	92.7	29.1	0.54	531
9H-6, 135–157	70.5	333	15.1	84.4	28.6	0.44	452
10H-1, 128–150	73.6	329	17.6	87.4	32.1	0.58	585
10H-5, 134–156	79.6	304	17.4	88.1	35.9	1.6	535
11H-2, 130–152	83.9	312	16.0	83.7	39.0	1.7	555
12H-1, 115–137	87.6	301	15.2	83.8	35.0	2.4	608
12H-3, 94–116	90.1	288	16.7	86.7	37.9	2.1	593
13H-2, 124–146	93.6	271	17.7	79.7	30.7	0.58	544
14H-2, 80–102	98.2	285	17.9	83.7	26.2	0.55	401
15H-2, 93–115	106.8	239	23.1	85.1	37.0	0.50	614
16X-2, 126–148	111.0	218	24.9	85.1	42.8	1.2	589
20X-4, 131–151	148.0						
22X-1, 131–151	162.9	114	39.4	93.3	48.5	1.8	665
22X-3, 68–88	165.0	62	35.8	92.9	48.9	1.3	497
23X-3, 100–120	175.3	100	42.2	93.5	40.0	0.98	392
344-U1412B-							
4X-2, 100–120	168.0						
5X-1, 120–140	176.4	108	59.1	108	69.7	1.6	526
6X-2, 99–125	186.7	127	62.4	122	81.3	3.1	639
7X-2, 51–73	196.0	123	61.9	140	115	3.1	653
344-U1412C-							
4R-CC	321.5	383	28.8	246	66.8	1.9	1100
5R-1, 0–36	328.8	334		314	598	1.6	778
6R-1, 9–20	338.59	140	21.8	309	518	3.5	160
7R-2, 96–112	350.31	140	84.1	270	219	6.9	475
8R-1, 121–148	359.11	148	111.2	250	198	3.9	175
8R-5, 59–95	364.13	157	109.3	251	302	2.1	208
9R-2, 58–88	369.02	279	98.7	262	394	5.2	359
344-U1412D-							
2R-2, 78–101	352.18	213	93.4	231	270	2.2	318
2R-5, 106–131	356.47	260	72.6	238	372	1.8	396
3R-3, 61–86	362.02	494	69.5	241	320	2.9	752

Table T10. Concentrations of hydrocarbon gases in headspace gas samples, Site U1412.

Core, section, interval (cm)	Depth (mbsf)	Methane (ppmv)	Ethane (ppmv)	Propane (ppmv)	C_1/C_{2+}
344-U1412A-					
1H-2, 0–5	1.50	4.25	ND	ND	—
1H-3, 0–5	3.00	6.15	ND	ND	—
1H-4, 93–98	5.43	16.3	ND	ND	—
2H-3, 0–5	8.90	59.4	0.420	ND	141
2H-6, 67–72	14.09	8,500	1.44	ND	5,920
2H-7, 101–106	15.27	8,410	0.855	ND	9,830
3H-2, 0–5	16.90	3,880	0.602	ND	6,450
3H-3, 0–5	18.40	14,300	0.850	ND	9,550
3H-6, 145–150	24.35	7,290	0.404	ND	18,000
4H-3, 0–5	27.90	7,690	0.612	ND	7,220
4H-5, 0–5	30.93	7,090	0.492	ND	6,380
5H-4, 0–5	36.27	10,900	0.645	ND	16,900
5H-7, 128–133	40.36	3,960	ND	ND	—
6H-3, 0–5	44.95	7,470	0.669	ND	5,220
6H-5, 0–5	47.99	268	ND	ND	—
7H-3, 0–5	51.97	1,300	ND	ND	—
7H-6, 0–5	55.97	406	ND	ND	813
8H-2, 0–5	59.01	3,760	ND	ND	—
8H-4, 0–5	61.73	734	ND	ND	—
9H-3, 0–5	65.87	893	ND	ND	—
9H-7, 0–5	70.61	5,780	0.692	ND	8,360
10H-2, 0–5	73.70	2,860	ND	ND	—
10H-6, 0–5	79.70	10,500	0.979	ND	7,540
11H-3, 0–5	84.04	5,490	ND	ND	—
12H-2, 0–5	87.67	2,820	0.825	ND	3,420
12H-4, 0–5	90.24	3,590	0.806	ND	4,460
13H-3, 0–5	93.70	755	ND	ND	—
14H-3, 0–5	98.33	4,850	0.828	ND	5,860
15H-3, 0–5	106.86	6,090	1.89	ND	3,220
16X-3, 0–5	111.09	4,210	1.20	ND	3,500
17X-3, 0–5	115.94	6,520	0.995	ND	6,550
17X-6, 0–5	119.72	6,220	1.57	0.396	3,160
18X-1, 0–5	122.70	4,900	0.750	ND	6,530
18X-3, 0–5	125.41	4,580	1.27	ND	3,600
19X-2, 0–5	133.90	3,180	ND	ND	—
19X-4, 0–5	136.57	7,670	1.78	ND	4,300
20X-2, 0–5	143.60	5,070	1.28	ND	3,960
20X-5, 0–5	148.11	4,410	1.89	ND	2,330
21X-1, 0–5	151.80	31,400	3.58	ND	8,780
21X-3, 0–5	154.58	5,960	2.72	ND	2,190
22X-1, 0–5	162.76	7,070	1.83	ND	3,870
22X-2, 0–5	163.01	2,030	0.516	ND	3,930
23X-2, 0–5	172.70	2,650	1.52	ND	1,740
23X-4, 0–5	175.40	1,980	1.47	ND	1,350
24X-3, 0–5	182.59	26,800	3.06	ND	8,760
25X-3, 0–5	191.94	16,300	2.66	ND	6,130
344-U1412B-					
1H-2, 0–5	1.50	218	1.67	ND	83.4
1H-4, 0–5	4.50	10.3	ND	ND	—
3X-2, 0–5	156.62	6,050	6.28	0.625	641
4X-3, 0–5	168.17	10,600	2.47	ND	3,590
5X-2, 0–5	176.60	4,400	1.57	ND	2,080
6X-3, 0–5	187.00	5,440	0.88	ND	6,150
7X-3, 0–5	196.24	15,500	1.44	0.438	8,240
8X-1, 0–5	204.30	9,040	1.22	ND	7,430
11X-1, 40–45	228.90	15,000	8.64	2.52	1,340
12X-1, 23–28	233.63	17,100	11.9	ND	1,430
344-U1412C-					
2R-1, 109–114	301.09	1,570	1.20	ND	1,310
5R-1, 31–36	329.11	5,550	7.17	ND	775
6R-1, 9–14	338.59	1,900	3.03	ND	628
6R-6, 0–5	344.77	1,720	4.10	ND	420
7R-2, 96–101	350.31	4,920	4.22	ND	1,170
8R-2, 0–5	359.38	3,380	3.34	3.08	527
8R-6, 0–5	364.49	9,560	3.10	ND	3,090
9R-3, 0–5	369.32	4,760	3.72	0.509	1,130

— = incalculable. ND = not detected.

Table T11. Concentrations of hydrocarbon and CO_2 gases in the void gas, Hole U1412A and U1412B.

Core, section, interval (cm)	Depth (mbsf)	Methane (ppmv)	Ethane (ppmv)	Propane (ppmv)	CO_2 (ppmv)	C_1/C_{2+}
344-U1412A-						
4H-4, 50–51	29.93	820,000	16.4	1.6	5,190	45,700
4H-6, 50–51	32.13	813,000	16.0	1.6	4,980	46,200
5H-2, 50–51	33.93	781,000	14.9	1.4	3,020	48,000
5H-4, 50–51	36.77	823,000	16.4	1.6	4,610	45,700
5H-7, 50–51	39.58	837,000	16.5	1.6	4,000	46,200
6H-1, 50–51	42.50	773,000	14.2	1.0	1,700	50,800
7H-1, 50–51	50.00	841,000	16.8	1.2	3,390	46,600
9H-2, 50–51	64.87	835,000	29.6	1.0	4,440	27,300
9H-7, 50–51	71.11	849,000	56.1	ND	1,910	15,200
10H-2, 50–51	74.20	848,000	24.6	1.2	4,610	32,800
11H-4, 50–51	85.75	849,000	28.0	2.7	2,570	27,600
12H-2, 50–51	88.17	842,000	54.5	2.2	3,500	14,900
13H-4, 50–51	95.41	850,000	44.6	3.1	2,730	17,800
14H-3, 50–51	98.83	838,000	53.4	4.3	5,070	14,500
18X-3, 50–51	125.91	788,000	62.9	10.9	11,100	10,700
19X-2, 50–51	134.40	838,000	58.6	7.0	6,420	12,800
19X-4, 50–51	137.07	822,000	63.4	8.9	10,500	11,400
23X-4, 50–51	175.90	844,000	85.3	7.2	6,830	9,120
344-U1412B-						
6X-3, 50–51	187.50	846,000	28.4	0.6	5,360	29,200
7X-3, 50–51	196.74	850,000	46.7	2.9	8,710	17,100

ND = not detected.

Table T12. Total carbon (TC), inorganic carbon (IC), total organic carbon (TOC), calcium carbonate, total nitrogen (TN), and C/N ratios, Hole U1412A.

Core, section, interval (cm)	Depth (mbsf)	TC (wt%)	IC (wt%)	TOC (wt%)	$CaCO_3$ (wt%)	TN (wt%)	C/N ratio
344-U1412A-							
1H-2W, 133–134	2.83	2.37	0.544	1.83	4.54	0.160	11.4
1H-4W, 2–3	4.52	1.70	0.301	1.40	2.51	0.145	9.68
1H-4W, 93–94	5.43	2.97	1.15	1.81	9.62	0.136	13.4
2H-2W, 136–138	8.76	2.06	0.459	1.60	3.83	0.152	10.5
2H-7W, 27–28	14.53	2.33	0.651	1.68	5.43	0.145	11.6
2H-7W, 106–107	15.32	2.11	0.547	1.56	4.56	0.124	12.6
3H-3W, 137–138	19.77	2.12	0.672	1.45	5.60	0.102	14.2
3H-5W, 137–138	22.77	2.17	0.737	1.43	6.15	0.098	14.6
3H-6W, 53–54	23.43	2.27	0.863	1.41	7.20	0.108	13.0
4H-2W, 135–136	27.75	2.03	0.652	1.38	5.43	0.089	15.6
4H-3W, 94–95	28.84	2.54	1.08	1.46	8.99	0.115	12.7
4H-4W, 138–139	30.81	2.34	0.841	1.50	7.02	0.132	11.4
5H-3W, 118–120	36.10	1.95	0.529	1.42	4.41	0.134	10.6
5H-3W, 63–64	35.55	2.11	0.685	1.43	5.72	0.093	15.3
5H-7W, 131–132	40.39	2.16	0.554	1.61	4.62	0.157	10.2
6H-2W, 130–131	44.76	2.33	0.508	1.82	4.24	0.178	10.2
6H-3W, 70–71	45.65	2.37	0.571	1.80	4.76	0.176	10.2
6H-4W, 131–132	47.79	2.17	0.469	1.70	3.91	0.172	9.93
7H-2W, 62–63	51.14	2.04	0.297	1.74	2.48	0.176	9.90
7H-2W, 27–28	50.79	2.20	0.589	1.61	4.91	0.158	10.2
7H-5W, 101–102	55.78	2.13	0.521	1.61	4.35	0.150	10.7
8H-1W, 27–28	57.77	1.98	0.364	1.61	3.04	0.173	9.33
8H-2W, 87–88	59.88	2.22	0.666	1.55	5.56	0.161	9.63
8H-3W, 98–99	61.49	2.47	0.839	1.63	7.00	0.144	11.3
9H-6W, 131–133	70.35	2.06	0.928	1.13	7.74	0.103	10.9
10H-1W, 126–127	73.46	2.14	0.845	1.30	7.04	0.140	9.25
10H-4W, 133–134	77.98	2.25	0.860	1.39	7.17	0.143	9.71
10H-5W, 33–34	78.47	2.15	0.742	1.41	6.19	0.146	9.67
11H-1W, 139–140	82.49	1.80	0.437	1.36	3.64	0.137	9.91
11H-2W, 128–129	83.80	1.97	0.268	1.70	2.24	0.168	10.1
12H-1W, 112–113	87.42	1.72	0.107	1.61	0.892	0.171	9.41
12H-2W, 137–138	89.04	1.62	0.106	1.52	0.885	0.163	9.29
12H-3W, 92–93	90.00	1.87	0.477	1.39	3.98	0.155	8.99
13H-2W, 120–121	93.44	2.15	0.900	1.25	7.51	0.128	9.72
14H-2W, 77–78	98.08	2.37	0.813	1.56	6.78	0.132	11.8
15H-2W, 91–92	106.62	2.67	1.07	1.60	8.91	0.161	9.94
15H-3W, 61–62	107.47	2.26	0.882	1.37	7.36	0.142	9.63
16X-2W, 120–121	110.81	2.58	1.08	1.51	8.97	0.147	10.2
16X-4W, 129–130	113.79	1.79	0.169	1.62	1.41	0.175	9.22
17X-2W, 122–123	115.64	1.68	0.470	1.21	3.92	0.146	8.28
17X-4W, 17–18	117.61	1.20	0.379	0.824	3.16	0.112	7.35
17X-5W, 69–70	119.45	2.39	0.901	1.49	7.51	0.161	9.25
18X-3W, 118–119	126.59	2.09	0.654	1.44	5.46	0.157	9.18
19X-3W, 68–69	135.74	2.05	0.810	1.24	6.75	0.153	8.12
19X-3W, 129–130	136.35	2.48	1.06	1.42	8.85	0.161	8.80
20X-4W, 28–29	146.88	2.75	1.07	1.68	8.95	0.163	10.3
20X-5W, 111–112	149.22	1.99	0.765	1.22	6.38	0.146	8.37
21X-1W, 116–118	152.96	1.63	0.437	1.19	3.65	0.156	7.65
21X-1W, 117–119	152.97	1.66	0.473	1.19	3.94	0.151	7.83
21X-2W, 89–91	154.19	1.79	0.512	1.28	4.27	0.157	8.16
22X-1W, 128–129	162.78	2.16	0.926	1.24	7.72	0.151	8.19
22X-3W, 29–30	164.52	1.55	0.405	1.15	3.38	0.150	7.64
22X-3W, 67–68	164.90	1.70	0.901	0.798	7.52	0.152	5.24
23X-3W, 99–100	175.19	1.77	0.547	1.22	4.56	0.156	7.86
23X-4W, 141–142	176.81	1.89	0.817	1.07	6.82	0.147	7.31
24X-2W, 65–66	182.43	1.93	0.581	1.35	4.85	0.124	10.9
24X-3W, 57–58	183.16	2.05	0.845	1.21	7.05	0.145	8.30
25X-5W, 140–142	194.86	1.60	0.593	1.01	4.95	0.108	9.35